1 Introduction to Finite Element Methods for Electromagnetic fields and coupled problems

1.1 Background: interacting physical phenomena

In engineering analysis and design, many phenomena have to be considered in order to predict a technical device's behaviour realistically. The physical processes involved are of electromagnetic, mechanical, thermal, mass transport, chemical, nuclear or other type. Moreover, non-energetic control techniques operate the device's behaviour following a set of mathematical and logical rules. The mathematical description of the complicated model is a coupled problem, almost always of a non-linear nature. An additional difficulty is the combination of the different time scales of the phenomena.

Numerical simulations are commonly used to analyse and design devices, though often only one field phenomenon is studied in detail. Software allowing these calculations is usually developed for a limited set of problems.
However, in order to tackle the physical interactions, the study of the coupled problems becomes a necessary, but complicated matter.
With larger and cheaper computing power coming available, this situation starts to change. Some commercial packages market 'multi-physics' options [ANSY], [MEMC]. However, the available approach is merely a simple iterative combination of individual field calculations with limited possibilities (e.g. same discretisation for the different subproblems, no special non-linear solution techniques, ...).

There is a clear need to study the coupled problems more thoroughly from the engineering point of view. Coupled problems are mathematically complicated and not always solvable by combining the existing well-studied, subproblem specific solver algorithms. An in-depth, global approach is required.

1.2 Electrical energy transfer: coupled physical interactions and time scales

Electrical energy research and development deals with the use of electrical, magnetic and electromagnetic phenomena to produce, transfer and transform this type of energy. It is governed by the Maxwell equations for electromagnetic phenomena. However, many other physical fields and control rules not governed by the physical application influence the system. The applicable devices can have any size: micro-electronic interconnect lines, on-chip integrated coils, MEMS (micro-electromechanical systems) [FUJI], miscellaneous actuators, sensors and passive

devices, electrical drives to huge power transformers and generators, electroheat applications [DORF].

Figure 1.1 illustrates the interaction at different levels, found in a general electromagnetic energy converter structure. Different fields, described by non-linear differential equations interact through losses, forces, cooling, thermal dependencies of material characteristics, etc. The overall system is governed by a control system. The power electronic system translates its commands into energetic signals supplied to the device.

The control levels are considered different from the physical energy exchanges in the scheme. The physical problems are governed by energy exchange, containment or minimisation principles. They are therefore referred to as ‘conservative’. The control equations, often in state variable form, are basically not energy-related and therefore ‘non-conservative’.

All fields have their own specific time scale. In the interaction, it may even seem that one field does not change at all, though the other behaves in an extremely dynamic way, for instance the electromagnetic-thermal interaction. Figure 1.2 compares the time scales, associated with the general electrical power processing problem template of Figure 1.1 [MOHA]. The typical ratio of the largest to the smallest time constant may be as large as 10^{10}, obviously having major consequences for the computational algorithms.

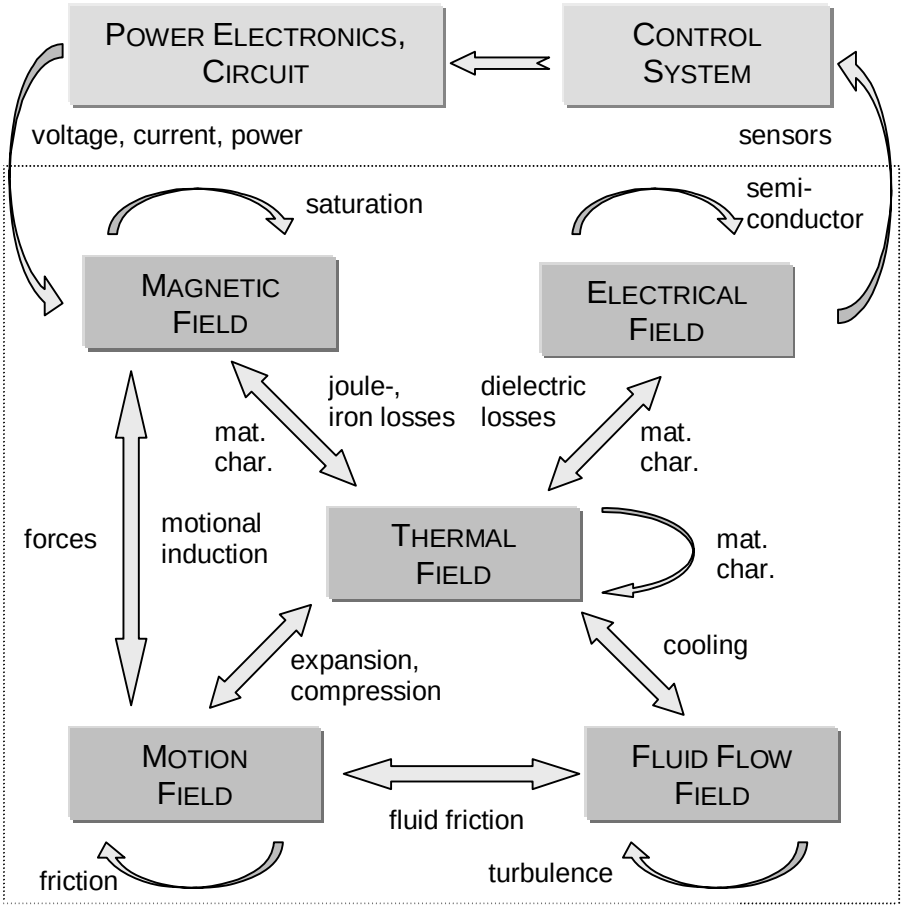

Figure 1.1 Field interaction in a general electromagnetic problem

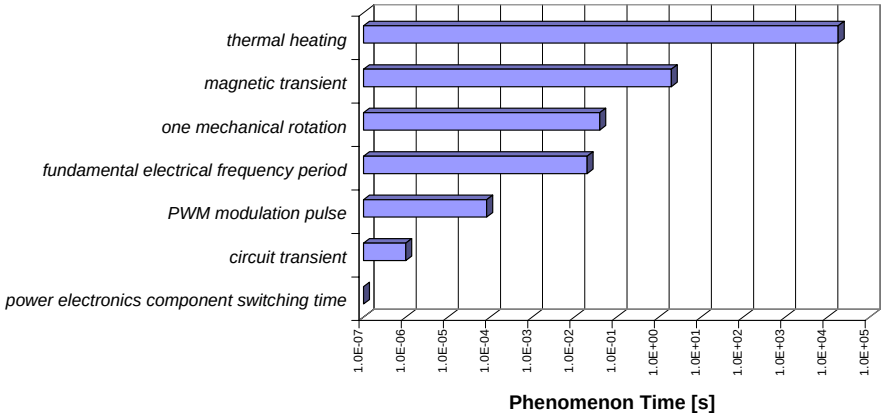

Figure 1.2 Comparison of typical time scales in a general, coupled electromagnetic problem

1.3 Coupled problems classification

The mathematical definition of a coupled problem is clearly presented in [ZIE2]: "*a coupled problem is a coupled system or formulation, defined on multiple domains, possibly coinciding, involving dependent variables that cannot be eliminated on the equation level*".
This term 'coupled problem' is often used in literature, but not always in the same context. Therefore, a classification of the coupled problem terminology is required.

A first remark concerns the often used expressions 'strong' and 'weak' coupling. Strictly speaking, when referring to the physical phenomena, these notions 'strong' and 'weak' indicate the strength of the interaction between the subproblems involved. The knowledge of the degree of mutual influence is one of the key goals of the coupled problem analysis, and therefore, not known at the instant of problem formulation. Moreover, it is a subjective notion, since there does not exist a clear quantifiable boundary between both classes. Note that a problem can even evolve in time from 'weak' to 'strong' or the other way around, because of the non-linear coupling mechanisms. This happens, for instance, when materials undergo a phase transformation and then exhibit a different behaviour. To make the confusion even larger, the strong/weak notion is used for other distinctions too, such as the non-linear numerical solution algorithm.

The coupled problem can be classified according to [HAM1], [HAM2]:

- *Extent*: The interacting fields are defined on partially or entirely overlapping problem domains (e.g. thermal-magnetic), or they can interact through an interface (e.g. a massive body and its cooling flow modelled separately). These groups of problems are sometimes called 'class I' and 'class II' coupled problems [ZIE2].
- *Discretisation method*: Continuous subproblems have to be discretised to obtain a mathematical model with a finite number of degrees of freedom. When this transformation is performed by the same discretisation method for all subproblems involved, e.g. the Finite Element Method (FEM), the problems are homogeneous. Otherwise, the notion 'hybrid' is applicable (e.g. a FEM/circuit combination).
- *Global non-linear numerical solution algorithm*: When the algebraic equations describing the field solution are combined and solved simultaneously in one large matrix system, a fully coupled algorithm is applied. However, when the equations or subsets of these equations are solved in a block-iterative algorithm, an internal cascade algorithm is used.

2 Modelling of coupled physical fields

2.1 Common aspects in the representation of individual physical fields

2.1.1 General representation

Many physical phenomena are described by very similar partial differential equations, on a domain Ω with boundary Γ, and may be fitted into the following prototype:

$$\alpha \frac{\mathrm{d}x}{\mathrm{d}t} - \nabla \cdot (\lambda \nabla x) + \beta x = f \,, \tag{2.1}$$

with x a generic scalar variable and t the time variable. The coefficients will be discussed further on.
The time derivative of x can be split into a position change dependence (motion at velocity $\vec{v}$) and the pure local time dependence:

$$\frac{\mathrm{d}x}{\mathrm{d}t} = \frac{\partial x}{\partial t} + \sum_i \left(\frac{\partial x}{\partial x_i} \frac{\partial x_i}{\partial t} \right) = \frac{\partial x}{\partial t} + \vec{v} \cdot \nabla x \,. \tag{2.2}$$

Substituting (2.2) into (2.1), yields:

$$\alpha \frac{\partial x}{\partial t} - \nabla \cdot (\lambda \nabla x) + \alpha \vec{v} \cdot \nabla x + \beta x = f \,. \tag{2.3}$$

The different terms involving the dependent variable x and the related coefficients and the source term are classified as shown in Table 2.1:

Term	*Term name*	*Coefficient name*
$\alpha \frac{\partial x}{\partial t}$	parabolic term (transient term)	(no general name; usually normalised to one)
$\nabla \cdot (\lambda \nabla x)$	diffusion term	diffusion coefficient
$\gamma \vec{v} \cdot \nabla x$	convection term (advection term)	convection coefficient
βx	absorption term	absorption coefficient
f	source term	-

Table 2.1 Terms and coefficients in the general differential equation

The boundary conditions on Γ can be distinguished into five types [JOHN]:

1. *Dirichlet boundary condition*, setting a fixed value C_D for the solution on the boundary Γ_N:

$$x = C_D \text{ on } \Gamma_D. \tag{2.4}$$

   This is a typical boundary condition to close the calculation domain, e.g. by setting a fixed voltage potential or temperature.
2. *Neumann boundary condition*, setting a value C_N of the derivative in the normal direction n on the boundary Γ_N:

$$-\frac{\partial x}{\partial n} = C_N \text{ on } \Gamma_N. \tag{2.5}$$

   This is a typical boundary condition to employ field symmetries or to apply a fixed flux.
3. *Robin boundary condition (mixed boundary condition)*, are a special type of Neumann boundary condition, in which the constant is replaced by a linear function of the local solution, containing parameters C_R and x_∞, on the boundary Γ_R:

$$-\frac{\partial x}{\partial n} = C_R\left(x - x_\infty\right) \text{ on } \Gamma_R. \tag{2.6}$$

   This is a typical boundary condition in thermal problems where convection is to be considered.
4. *Periodic boundary conditions*, linking the solution on geometrically different boundaries. These boundary conditions are used to impose symmetries, equivalent to an infinite spatial periodicity. When only two boundaries are involved, this boundary condition type is often referred to as *binary boundary condition*:

$$x_{P1} + C_{P1}x_{P2} = C_{P2} \text{ on } \Gamma_P \tag{2.7}$$

$$\text{or: } \frac{\partial x_{P1}}{\partial n} + C_{P3}\frac{\partial x_{P2}}{\partial n} = C_{P4} \text{ on } \Gamma_P. \tag{2.8}$$

   This is a typical boundary condition to employ field and geometrical symmetries simultaneously.
5. *Floating boundary*, indicating that the solution on this boundary is equal to a single value that is yet to be determined. This condition is similar to a floating Dirichlet condition inside the considered domain.

The general equation (2.3) is applicable to various physical fields [ZIE1], [HUEB], such as:

- *Electrostatic fields*, due to distributed charges and fixed voltages on boundaries.
- *Magnetic fields*, modelled by an appropriate potential and driven by imposed source currents and/or permanent magnet materials; all types of boundary conditions are applicable.
- *Electrical current* in a plane ('in-plane problem' [HAM1]).

- *Thermal fields* with distributed heat sources or sinks; the most common boundary conditions are fixed temperature (Dirichlet) and convection/radiation (modelled as Robin boundary conditions, possibly non-linear).
- Uncompressible, turbulence-free *fluid flow*, described by flow potentials.
- *Diffusion problems* with locally varying concentrations.

2.1.2 Time and Frequency domain

The treatment of the independent time variable in (2.3) is crucial for the further solution of the partial differential equation. When the evolution of the solution with respect to the time is to be found, the coefficients in this equation and the boundary conditions (2.4)-(2.8) are to be considered as time-dependent as well. This will eventually lead to an ODE (ordinary differential equation) problem, (see section 2.3.7 below).

Often only the steady state is of concern. The time dependency however, does not have to vanish in these cases. If a (periodic) time dependent source or boundary condition is present, the solution will be constant in the frequency domain. In this case, the frequency domain description is more appropriate, especially when dealing with linear systems. Two transformation techniques can be used to obtain a complex frequency domain PDE (partial differential equation):

1. Fourier Transformation

The Fourier transform $\mathscr{F}$ is defined as [KREY]:

$$\mathscr{F}\left(x(t)\right) = \underline{X}(\omega) = \int_{-\infty}^{\infty} x(t)\, e^{-j\omega t}\,\mathrm{d}t\,. \tag{2.9}$$

Applying this to (2.3), a PDE involving convolution products is obtained. Many of these convolution products simplify when the terms are linear and hence the coefficients become constants.

$$\begin{aligned} &-\nabla\cdot\left(\mathscr{F}(\lambda) * \nabla\underline{X}\right) + \vec{v}\cdot\mathscr{F}(\alpha) * \nabla\underline{X} + \left(\mathscr{F}(\beta) + j\omega\mathscr{F}(\alpha)\right) * \underline{X} \\ &= \mathscr{F}(f) \end{aligned} \tag{2.10}$$

The symbol " * " indicates the convolution operation.

2. Separation of the variables

In this approach, the dependent variable is replaced by a product of a harmonic function with a phasor:

$$x(t) = \underline{X}(\omega)\, e^{j\omega t}\,, \tag{2.11}$$

in which the pulsation ω becomes merely a parameter. Substituting (2.11) into (2.3) with assumed constant coefficients and a periodic source term, followed by a multiplication by $e^{-j\omega t}$, this yields:

$$-\nabla\cdot\left(\lambda\nabla\underline{X}\right) + \alpha\vec{v}\cdot\nabla\underline{X} + \left(\beta + j\omega\alpha\right)\underline{X} = \underline{F}\,. \tag{2.12}$$

It is possible to extend (2.10) to a sum of harmonic components. To account for non-linearities, the coefficients have to be written in this form, when possible. This operation yields convolution-type products as well.

Often, neither the pure time domain, nor the frequency domain approach is suited for the problem. For instance, this is the case when the problem contains fast and slow dynamic phenomena at the same time, as it is found in coupled problems. There, the effects can be found on different time scales, associated with the respective time constants. Then, a mixed approach may be more appropriate.
When the slow dynamic phenomenon, in conjunction with a very fast one in quasi steady state, is of interest, (2.11) can be altered to

$$x(t) = \underline{X}(t,\omega)\, e^{j\omega t}\,, \tag{2.13}$$

making $\underline{X}$, the 'envelope-function' (Figure 2.1), again a function of time (slow time scale) with parameter ω (fast time scale, dealt with in the frequency domain).

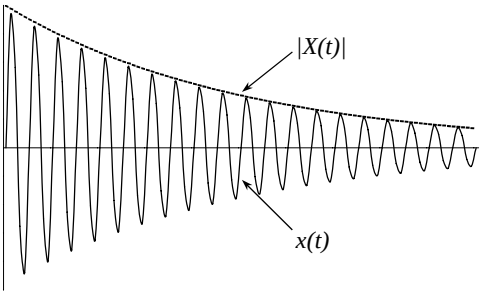

Figure 2.1 Function *x* and its 'envelope' *X*

This yields an extra time derivative when compared to (2.12):

$$-\nabla\cdot\left(\lambda\nabla\underline{X}\right)+\alpha\vec{v}\cdot\nabla\underline{X}+\left(\beta+j\omega\alpha\right)\underline{X}+\alpha\frac{\partial\underline{X}}{\partial t}=\underline{F}\,. \tag{2.14}$$

In this respect, a more general alternative for the Fourier transform could be a Wavelet transformation, using basis functions localised in space and time [DR01].

2.1.3 Non-linearities

In general, three basic types of non-linearities can be found within the considered coupled PDEs/ODEs and their boundary conditions:

- For individual field problems, a coefficient is a function of the unknown field solution, e.g. magnetic saturation.
- For a coupled problem, the coefficient of a composing physical field equation, the 'subproblem', may vary with the other field solution (e.g. temperature dependent electromagnetic material properties).
- A term, e.g. the eddy current loss term, is a non-linear expression of one or more of the variables.

Combinations of these basic types exist. Each of these types requires a different approach, for instance when determining partial derivatives, depending on the chosen non-linear solution algorithm.

2.1.4 Notation of coupled field equations

A set of *n* coupled equations can generally be written as:

$$\sum_{j=1}^{n}\left(\alpha_{ij}\frac{\partial x_j}{\partial t}-\nabla\cdot\left(\lambda_{ij}\nabla x_j\right)+\alpha_{ij}\vec{v}\cdot\nabla x_j+\beta_{ij}x_j\right)=f_i,\ i=1(1)n\,. \tag{2.15}$$

To be a true coupled problem, it may not be possible to eliminate these variables x_j. An alternative notation style is obtained by rearranging (2.15) to a matrix equation:

$$\left[\alpha_{ij}\right]\frac{\partial\left[x_j\right]}{\partial t}-\nabla\cdot\left(\left[\lambda_{ij}\right]\nabla\left[x_j\right]\right)+\left[\alpha_{ij}\right]\vec{v}\cdot\nabla\left[x_j\right]+\left[\beta_{ij}\right]\left[x_j\right]=\left[f_i\right]. \tag{2.16}$$

For the further discussion in which the continuous equations will be converted into discrete problems, the notation (2.15) is preferable. It expresses that a coupled problem consists of different physical problems, each calculated on their own subdomain Ω_i. These domains do not need to be identical and may be partially overlapping.

It must be noted that some individual equations with more than one degree of freedom, such as vector or complex variables, could be written in the form of (2.16), but are not to be considered as coupled problems.

2.2 Individual physical field calculation methodologies

2.2.1 Method types

2.2.1.1 Lumped methods

For solution purposes, many physical fields, or parts of them can be reduced in their mathematical dimensionality. By an appropriate choice of potentials, either scalar or vector, the PDEs can be simplified. If the fields and their gradients follow certain geometrical patterns, the continuous character can be exchanged for lumped parameter representations. This leads to expressions in terms of 'across'-variables and 'through'-variables. Typical examples are:

- electrical current between two voltage nodes through an electrical impedance;
- magnetic circuits describing main flux paths;
- heat flux between two temperature nodes through a thermal impedance;
- fluid flow between points of (generalised) pressure through tubes;
- mechanical systems expressed in terms of speeds and forces acting on a mass.

The equations can then be written in terms of concentrated parameters in generalised lumped resistances, capacitances and inductances. It must be noted that not every physical field has an equivalent representation for these lumped parameters. For instance, a thermal inductance does not exist due to fundamental thermodynamic laws.

If these physical systems are described in a consistent way, the related energy is conserved. Therefore, these systems are often called ‘conservative’.

To decide whether these lumped methods, which are considerably simpler than the field methods, are valid, decision criteria are developed, such as a limiting value on the dimensionless Biot number [LIEN] in thermal problems.

2.2.1.2 Field methods

If the continuity of the field cannot be ignored, a coupled field solution of the entire domain is essential. Potential formulations can still be used to reduce the complexity. Since an analytical field solution is often hard to find for realistic geometries and with non-linear materials, numerical methods are required. A mix of such field methods over different subdomains may be interesting.

2.2.1.3 Hybrid methods

Often it is advantageous to combine the previous types to a hybrid method, e.g. when some regions can be solved in a lumped manner, but other parts of the solution domain require a field representation, solved by a purely numerical method. An example of such a combination is a magnetic or thermal 2D field problem extended with a (generalised) circuit equation modelling effects in the third dimension. This could be considered as a special kind of coupled problem.

2.2.2 Numerical solution methods

To approximate the solution of non-linear sets of PDEs of the form (2.15), many numerical methods are proposed, used and published. Table 2.2 gives an overview and discusses the advantages and drawbacks.

Considering the arguments in this table, FEM appears to be best suited to compute non-linear, coupled physical fields in engineering. The devices to be simulated often contain complicated shapes, for which FDM is less suited. Since the ability to tackle non-linearities in the domain is crucial, BEM shows an essential drawback. How the FEM can be extended to solve coupled problems is shown further on in section 2.3.

Although it may seem advantageously to use a combination of methods, best matching the subproblems (e.g. BEM for infinite-domain linear subproblems, coupled with FEM in the finite, non-linear subproblems), problems may occur when the different sets of unknowns need to be combined, e.g. to evaluate non-linear coefficients. Then, the related subproblem solution needs to be translated to the chosen method. For instance, this would mean the interpolation or projection of a BEM solution onto a FEM discretisation, often leading to various time-consuming calculations.

Method	*Principal idea*	*Main advantages*	*Main drawbacks*
Finite Difference Method (FDM)	Approximates the differential operators by difference operators.	Easy to build equation system Non-linearities can be treated Sparse matrix equation to solve	Difficult to model curved boundaries Adaptation of the discretisation can be complicated Infinite domains need to be transformed Large number of unknowns
Finite Element Method (FEM)	Approximates the solution by a weighted sum of basis functions with a limited span (the mesh elements)	Complicated shapes are no problem (approximated by chords or more complicated isoparametric elements) Local refinement of the mesh and basis functions allow to enhance the approximation where required Non-linearities can be treated Sparse matrix equation to solve	A high quality mesh is required to obtain accurate results Infinite domains need to be transformed Large number of unknowns Treatment of first order field derivatives is difficult
Boundary Element Method (BEM)	Builds a solution as a sum of known semi-analytical solutions (e.g. Hänkel functions) written in terms of boundary points [KOST]	Easy discretisation of boundaries Significant reduction of the number of unknowns (only boundary points, no interior points) Infinite domain is allowed	Non-linearities require spectral methods [KOST] Dense system matrix, often non-symmetric, non-positive definite Complex integral evaluations

Table 2.2 Overview of numerical field solution methods

2.3 The finite element method for general problems

The FEM can be derived using general mathematical degrees of freedom (MDOFs) on a discretisation, the mesh. It contains arbitrary elements represented by a set of geometrical degrees of freedom (GDOFs) jointly covering the calculation domain Ω. Eventually, the template FEM building blocks will be filled in with physically meaningful coefficients and variables.

Although extensive literature exists on FEM [RAO], [BINN], [ZIE1], the main issues are highlighted here from the point of view of coupled problem modelling.

2.3.1 Discretisation

The idea behind the FEM is to approximate the solution x_i by a weighted sum $\bar{x}_i$ of m_i rather simple functions N_k, called basis or shape functions (elements), each having a local span $\Omega_e \subset \Omega$.

$$\bar{x}_i = \sum_{k=1}^{m_i} N_k x_{ik} \ , \quad i = 1(1)n \ . \tag{2.17}$$

In $\Omega \setminus \Omega_e$, the function is identical to zero. The union of the functions' spans approximates the solution domain as closely as possible. The functions constitute a basis of the vector space in which the solution is approximated. The geometric boundaries of their span are described by geometrical nodes. More than one function may have the same span, as long as they are linearly independent, as for instance in so-called hierarchic elements. The weights x_{ik} are the mathematical degrees of freedom. For some types of elements (nodal elements) they can be associated with a geometrical node. In that case they are commonly called the mathematical nodes. A mathematical node is not always a geometric node, e.g. the nodes in the middle of edges in higher order elements.

Equation (2.17) implicitly assumes that the functions N_k and thus the mesh are identical for all subproblems *i*. This is not necessarily the case, but for simplicity it is assumed that when different meshes and different N_k^i are used, the approximate solution of one subproblem is available in terms of all the other subproblems' basis functions. This is theoretically achieved by projections between the different vector spaces. How this is accomplished in practice, is discussed in section **Error! Reference source not found.**.

2.3.2 Element types

There exist many different types of elements. The most common types are polynomial interpolating functions of a pre-set order m_i. Hence the error, which depends on a characteristic geometrical mesh parameter *h*, has an order of m_i+1:

$$x_i = \bar{x}_i + O\left(h^{(m_i+1)}\right) \tag{2.18}$$

Two common types of interpolating elements are [ZIE1], [HUEB], [RAO]:

- *Lagrange interpolating elements*: This popular polynomial function family is based on Lagrange interpolation. The Lagrange polynomials have a value one in a distinct point and zero in the other interpolation points. The derivatives at the boundaries of the interpolation interval may be discontinuous.
- *Hermite interpolating elements*: This polynomial function family is based on the Hermite polynomials, having the possibility to enforce continuous derivatives at the functions' boundaries.

Hierarchical elements are a special class of elements. They allow to adaptively construct higher order approximations. Polynomial combinations of first order (usually Lagrange) functions are used to construct higher order shape functions, with the same span as the original elements [ZIE1]. The constructed functions group's MDOFs, along with the original functions' MDOFs form a higher order approximation. These newly created MDOFs are not always associated with nodal GDOFs, but with edges (e.g. product of two first order nodal functions) or surfaces (product of three first order nodal functions) etc. These elements play a key role in *p*-adaptation schemes.

Isoparametric elements arise when coordinate transformations are applied on standard polynomial elements. This transformation may map elements with straight geometric boundaries on elements with curved boundaries due to non-straight shapes in the computational domain. This is an alternative to chord approximations for round shapes, yielding fewer elements but requiring more complicated mathematics (i.e. 'Jacobian transformations').

2.3.3 Variational equation and weak form

The starting point of all the procedures to obtain the FEM equation system, more in particular fixing the weights x_{ik}, is the derivation of an equivalent integral equation for (2.17). The most common ways to accomplish this are:

- *Minimise the field energy*: due to thermodynamic laws, the solution of most individual physical fields minimises the energy associated with the field in the computation domain. Hence the minimum of the energy integral expression leads to the desired solution. This method is less useful for coupled problems since there is usually no overall energy function available when more than one physical phenomenon is involved. The combination, e.g. by summation of individual energies, may not yield a unique solution.

- *Minimise the associated functional*: for a lot of PDEs and their boundary conditions, involving some terms of (2.3), an equivalent variational integral exists of which the extremum is a solution of the PDE. It has been proven that this is possible if the operator associated with the PDE fulfils a condition called self-adjointness [JOHN]:

$$\int_{\Omega}\int_{0}^{t}\left(x_i\, L_{ij}\left(x_j\right)\right)\mathrm{d}t\,\mathrm{d}\Omega = \int_{\Omega}\int_{0}^{t}\left(L_{ij}\left(x_i\right)x_j\right)\mathrm{d}t\,\mathrm{d}\Omega\,, \tag{2.19}$$

with L_{ij} the operator in the field equation i, acting on the variable of field j. Unfortunately, the conditions this operator has to fulfil are too strict for many coupled problems and an equivalent functional is not found. In the case a field energy integral exists, the functional is equivalent.

- *Method of the weighted residuals*: this is the most general method, that works for any PDE or algebraic equation and coupled problems of any kind. It is motivated by the fact that a residual R_i, defined in (2.20), is zero for the exact solution x_i. For an approximate solution $\bar{x}_i$ it should be forced to zero by determining the unknown coefficients x_{ik}, defined in (2.17).

$$\sum_{j=1}^{n}\left(\alpha_{ij}\frac{\partial \bar{x}_j}{\partial t}-\nabla\cdot\left(\lambda_{ij}\nabla\bar{x}_j\right)+\alpha_{ij}\vec{v}\cdot\nabla\bar{x}_j+\beta_{ij}\bar{x}_j\right)-f_i=R_i\,,\qquad i=1(1)n \tag{2.20}$$

To transform (2.3) into a functional, each equation is multiplied (weighted) with a set of test functions w_l. The product is integrated over the computation domain. Hence, the approximate solution is found as the solution of:

$$\int_{\Omega} w_l\left(\sum_{j=1}^{n}\left(\alpha_{ij}\frac{\partial \bar{x}_j}{\partial t}-\nabla\cdot\left(\lambda_{ij}\nabla\bar{x}_j\right)+\alpha_{ij}\vec{v}\cdot\nabla\bar{x}_j+\beta_{ij}\bar{x}_j\right)-f_i\right)\mathrm{d}\Omega=0\qquad i=1(1)n\,. \tag{2.21}$$

Continuity problems arise when integrating the second order derivatives in (2.21) with low–order finite elements. In that case, Green's formula has to be applied to obtain first order derivatives only in the 'weak form' of the PDE.
The boundary conditions have to be included in the integral equation (2.21). The following boundary integrals need to be added to the left-hand side of (2.21) for the Neumann and mixed boundary conditions (2.4)-(2.8):

$$\int_{\Gamma_{\mathrm{N},i}} w_{(\mathrm{N})l}\left(-\frac{\partial x}{\partial n}-C_{\mathrm{N},i}\right)\mathrm{d}\Gamma+\int_{\Gamma_{\mathrm{R},i}} w_{(\mathrm{R})l}\left(-\frac{\partial x}{\partial n}-C_{\mathrm{R},i}\left(x_i-x_{\infty,i}\right)\right)\mathrm{d}\Gamma \tag{2.22}$$

The Dirichlet boundary condition is imposed by a proper substitution of the constraint MDOFs (essential boundary condition).

The choice of the test functions determines the obtained approximation and influences the numerical properties of the system of equations. A possibility is to enforce an exact solution at a number of points (collocation method); this is equivalent to a weighting with Dirac functions at these points. A different common choice is to use the same basis functions as used to write the FEM solution: the Galerkin approach.

$$w_l = N_l \tag{2.23}$$

In this way it is assured that for every coefficient of (2.21) and (2.22), an expression is derived. This Galerkin approach eventually leads to the same equations as the two previous variational methods. When the weighting

function equals the shape function, on which the operator is applied, a least-square solution is obtained.

Since this weighted residual approach is the best suited and often the only one generally possible for coupled problems of the type (2.15), the further considerations and discussions will be based on (2.21) and (2.22).

2.3.4 Building blocks for standard equation terms

To obtain expressions for the basic building blocks to construct the FEM equation for the Galerkin method, the approximating sum (2.17) is substituted in (2.21) and in the boundary equations. Next, the integral and summation operators are interchanged. The integral equation (2.21) then becomes (2.24).
To be able to put the PDE coefficients, the different α_{ij}, λ_{ij}, β_{ij}, f_i or C_i in front of the integral, it is assumed that they are constant over the entire integration domain Ω_e. This is a key assumption and is discussed later in section **Error! Reference source not found.** for non-linear and dependent coefficients.

$$\begin{aligned}
&\sum_{j=1}^{n}\Bigg[\sum_{k=1}^{m_i}\Bigg[\left(\overline{\alpha}_{ij}\int_{\Omega_e}\left(N_l\,N_k\right)\mathrm{d}\Omega\right)\frac{\partial x_{jk}}{\partial t}+\Bigg(-\overline{\lambda}_{ij}\int_{\Omega_e}\left(N_l\,\nabla^2 N_k\right)\mathrm{d}\Omega\\
&+\overline{\alpha}_{ij}\vec{v}\cdot\int_{\Omega_e}\left(N_l\,\nabla N_k\right)\mathrm{d}\Omega+\overline{\beta}_{ij}\int_{\Omega_e}\left(N_l\,N_k\right)\mathrm{d}\Omega\Bigg)x_{jk}\Bigg]\Bigg]-\overline{f}_i\int_{\Omega_e}N_l\,\mathrm{d}\Omega\\
&+\Bigg(-\int_{\Gamma_{\mathrm{N},i}}\left(N_l\frac{\partial N_k}{\partial n}\right)\mathrm{d}\Gamma-\int_{\Gamma_{\mathrm{R},i}}\left(N_l\frac{\partial N_k}{\partial n}\right)\mathrm{d}\Gamma\\
&-\overline{C}_{\mathrm{R},i}\int_{\Gamma_{\mathrm{R},i}}\left(N_l\,N_k\right)\mathrm{d}\Gamma\Bigg)x_i-\overline{C}_{\mathrm{N},i}\int_{\Gamma_{\mathrm{N},i}}N_l\,\mathrm{d}\Gamma-\overline{C}_{\mathrm{R},i}x_{\infty,i}\int_{\Gamma_{\mathrm{R},i}}N_l\,\mathrm{d}\Gamma=0,\\
&\qquad\text{for } i=1(1)n\,.
\end{aligned}\tag{2.24}$$

The boundary integrals are only required if the element's edge is constrained with that particular condition.

The second order derivatives in the integral containing the diffusion term of (2.24) cause continuity problems at the element boundaries when integrating low order shape functions. Therefore, this term has to be simplified, by applying Green's first theorem (2.25) [KREY]. Then, the order of the partial derivatives drops by one and the so-called 'weak form' of the PDE is obtained.

$$\int_{\Omega_e}\left(N_l\,\nabla^2 N_k\right)\mathrm{d}\Omega=-\int_{\Omega_e}\left(\nabla N_l\,\nabla N_k\right)\mathrm{d}\Omega+\int_{\Gamma_{\Omega_e}}\left(N_l\frac{\partial N_k}{\partial n}\right)\mathrm{d}\Gamma\tag{2.25}$$

When the test functions N_l in the boundary integrals containing the normal derivatives in (2.24) and (2.25) are multiplied by ± 1 (constrained boundary) or omitted (free boundary), depending whether the considered edge is constrained or not, these integrals cancel each other. Hence, the homogeneous Neumann boundary

condition (C_N=0), is fulfilled implicitly (natural boundary condition). Eq. (2.24) then reduces to:

$$\begin{aligned}
&\sum_{j=1}^{n}\Bigg[\sum_{k=1}^{m_i}\Bigg[\left(\overline{\alpha}_{ij}\int_{\Omega_e}\left(N_l\,N_k\right)\mathrm{d}\Omega\right)\frac{\partial x_{jk}}{\partial t}+\Bigg(\overline{\lambda}_{ij}\int_{\Omega_e}\left(\nabla N_l\,\nabla N_k\right)\mathrm{d}\Omega\\
&+\overline{\alpha}_{ij}\vec{v}\cdot\int_{\Omega_e}\left(N_l\,\nabla N_k\right)\mathrm{d}\Omega+\overline{\beta}_{ij}\int_{\Omega_e}\left(N_l\,N_k\right)\mathrm{d}\Omega\Bigg)x_{jk}\Bigg]\Bigg]\\
&+\left(-\overline{C}_{R,i}\int_{\Gamma_{R,i}}\left(N_l\,N_k\right)\mathrm{d}\Gamma\right)x_i\\
&=\bar{f}_i\int_{\Omega_e}N_l\mathrm{d}\Omega+\overline{C}_{N,i}\int_{\Gamma_{N,i}}N_l\mathrm{d}\Gamma+\overline{C}_{\mathrm{R},i}x_{\infty,i}\int_{\Gamma_{R,i}}N_l\mathrm{d}\Gamma,\\
&\qquad\text{for } i=1(1)n
\end{aligned}\tag{2.26}$$

In general, only four domain integrals and two boundary integrals remain in (2.26). These can be integrated using analytical or numerical methods, depending on the degree of difficulty of the expressions. By writing the result in matrix form and combining the different terms, the contribution to the FEM matrix and right-hand side is obtained.

$$\begin{aligned}
&\sum_{j=1}^{n}\left[\left(\overline{\alpha}_{ij}\boldsymbol{H}_i\right)\frac{\partial\boldsymbol{x}_j}{\partial t}+\left(\overline{\lambda}_{ij}\boldsymbol{K}_i+\overline{\alpha}_{ij}\vec{v}\cdot\boldsymbol{M}_i+\overline{\beta}_{ij}\boldsymbol{H}_i\right)\boldsymbol{x}_j\right]-\overline{C}_{\mathrm{R},i}\boldsymbol{C}_i\boldsymbol{x}_i\\
&=\bar{f}_i\boldsymbol{F}_i+\overline{C}_{\mathrm{N},i}\boldsymbol{T}_{i,\mathrm{N}}+\overline{C}_{\mathrm{R},i}x_{\infty,i}\boldsymbol{T}_{i,\mathrm{R}}\\
&\qquad i=1(1)n\,.
\end{aligned}\tag{2.27}$$

The matrices and vectors $\boldsymbol{K}_i$, $\boldsymbol{H}_i$, $\boldsymbol{M}_i$, $\boldsymbol{C}_i$, $\boldsymbol{F}_i$, $\boldsymbol{T}_i$ are calculated in more detail in appendix A.1.

2.3.5 Overall matrix system assembling

In general, the overall system matrix is built in nested loops and on different matrix levels: first, the element matrices are constructed, then these are put in the large system matrix. (See [HAM3] for detailed schemes.)
At first, the different element matrix contributions are calculated. These matrices are added after multiplication with the appropriate coefficient. The contributions of the boundary conditions (e.g. mixed conditions) are added as well.

Secondly, the composite element matrix entries are added into the global matrix system. At this point, the local MDOF numbers have to be translated into global MDOF numbers, indicating the position where the new entry is to be added. At this level, several checks regarding the boundary conditions need to be performed. If the MDOF is constrained by an essential (Dirichlet) boundary condition, it is not added, but substituted. In practice, an identity equation is used for this MDOF, due to its higher priority. Periodic boundary conditions need a particular treatment as well. One of the involved MDOFs is left free; the equation of the other involved MDOF is replaced by the algebraic boundary condition expression. This may even be done by

using a dummy equation and substituting the correct solution for this MDOF afterwards.

2.3.6 Adaptation strategies

When the accuracy of a subproblem solution is not sufficient in a zone, the mesh can be refined there locally and the problem is solved again. Two basic finite element refinement strategies and their combination can be distinguished for individual FEM problems:

1. *h-refinement* [ZIE1]: The element's span is refined by introducing new GDOFs leading to a new set of elements. For instance, new GDOFs are put in the middle of the edges of the original element and connected, yielding four new elements. Consequently, operations to enhance the mesh quality are performed [MER1], [BANK].
2. *p-refinement* [ZIE1]: The order of the element's shape function is increased by introducing new MDOFs. When hierarchical elements are used, the new elements can be constructed easily without replacing the existing set of MDOFs. It is also possible to maintain solution continuity between adjacent elements with different orders of the shape function.
3. *hp-refinement*: Combines both previous strategies. Research is still going on regarding the optimal combination strategy [GIAN], [VANT]. For instance, '*h*' is used until the elements are becoming relatively small, after which '*p*' continues.

These strategies are applied on candidate elements with a normalised error exceeding a pre-set limit. First, error values are calculated using problem-specific error estimators and then normalised. Next, these elements are ordered by rising error value. The 'worst' elements in this series are refined.

2.3.7 Time discretisation

2.3.7.1 Time marching schemes

When the time domain PDE, after the FEM discretisation, is transformed into (2.27), an algebraic ODE problem remains. The last variable to discretise, is time. This is a general problem, not only existing in PDE problems, for which many methods have been developed. Generally, the solution is obtained by a time-marching scheme in which the new solution at a certain point in time is derived, using a subset of the previous solutions.

The general template for the ODE-set to be solved is:

$$\frac{\partial \boldsymbol{x}}{\partial t} = \boldsymbol{f}(\boldsymbol{x}, t) = \boldsymbol{f}(..., x_{i-1}, x_i, x_{i+1}, ..., t), \tag{2.28}$$

The vector $\boldsymbol{x}$ is solved for a set of time samples t_l. Two important classes of methods exist to discretise the time derivative in (2.28) [PRES].

- *Linear Multistep methods (LM)*:
  These methods can be written in the form of the following linear expression:

$$\sum_{j=0}^{p} \alpha_j \boldsymbol{x}[t_{l+j}] = \Delta t_l \sum_{j=0}^{p} \beta_j \boldsymbol{f}[t_{l+j}], \tag{2.29}$$

with α_j and β_j method dependent parameters; $\boldsymbol{f}$ is the short notation of the function evaluation in the right-hand side of (2.28). Explicit (β_p=0) and implicit ($\beta_p \neq 0$) versions of (2.29) do exist. The coefficient α_p is usually scaled to 1.

- *Runge-Kutta methods (RK)*:
  These methods consist of explicit non-linear expressions:

$$\boldsymbol{x}[t_{l+1}] = \Delta t_l \, \boldsymbol{\psi}(\boldsymbol{x}[t_l], \Delta t_l, \boldsymbol{f}[t_l]), \tag{2.30}$$

  with $\boldsymbol{\psi}$ a weighted average of consecutive derivative approximations at intermediate time-steps. Implicit methods are applicable as well [CAME].

These methods can be interpreted as further developments of finite-difference time discretisations. The general FEM expression (2.17) needs to be extended:

$$\bar{x}_i = \sum_{k=1}^{m_k} N_k \, x_{ik}[t_l], \quad i = 1(1)n, \tag{2.31}$$

since the complete spatial field solution is computed at all time steps t_l.

An alternative could be considering the time variable as a 'fourth spatial dimension' modelled by FEM and discretise the time dimension as well. The FEM mesh is then filled with so-called 'space-time elements': $N_k(x,y,z,t)$ [RAO]. This full-FEM approach is theoretically more flexible, since time steps can now be adapted in every element, e.g. this is common in computational fluid dynamics (CFD) calculations [DELA]. However, this is less practical in coupled problems: to interface between problems of various kinds, a large subset of the solution is required at the considered time step. Thus, in practice almost the whole solution has to be determined, i.e. calculated or interpolated. Even more, keeping track of all the required intermediate solutions at different time steps is a complicated organisational and memory-consuming problem. Using an equidistant time-mesh, the same formulation as the finite difference time discretisation is obtained.

Traditionally, the single step methods are popular to solve large-scale ODEs originating from PDEs solved by means of FEM [MER1]. Since the FEM approach already introduces a discretisation error, a high-order time discretisation is not absolutely necessary. An additional advantage is the moderate use of memory to store previous and intermediate solutions. The lower order of this method is not troublesome if the time step is chosen sufficiently small. The template for the single step methods with parameter θ is:

$$\boldsymbol{x}[t_{l+1}] = \boldsymbol{x}[t_l] + \Delta t_l \left(\theta \, \boldsymbol{f}[t_{l+1}] + (1-\theta)\boldsymbol{f}[t_l]\right). \tag{2.32}$$

The method is stable if $\theta \geq 0.5$. Theoretically it is optimal for linear problems if θ=0.5 (Crank-Nicholson), but numerical and other problems prevent the use of this value [MER1]. θ=1.0 (backward difference) yields the full-implicit method, which

damps numerical oscillations quickly. θ=2/3 is the so-called Galerkin choice, which is obtained if (2.32) is derived using a Galerkin weighted residual approach instead of finite differences [ZIE2]. This θ parameter can be optimised to approximate a certain time constant exactly, but when the time constants are more or less distributed over an entire spectrum, as it is the case with many stiff problems, the optimal θ parameter equals the value 0.878 (Liniger choice).

The solution of the non-linear equation (2.32) using predictor-corrector schemes or Newton-Raphson methods is discussed extensively in chapter 5.1.

2.3.7.2 Time step choice

The choice of the time step Δt_l is important for the stability of the numerically approximated ODE solution, stiff or non-stiff. For first order LM-methods applied on FEM systems, the following upper bound, containing the PDE coefficients α and λ (see Table 2.1) can be derived:

$$\Delta t_l < \zeta \frac{\alpha}{\lambda} h^2, \tag{2.33}$$

with h a characteristic size parameter of the used domain discretisation and ζ a numerical parameter, depending on the type of elements and θ [ZIE2].
To be able to solve the implicit equation (2.29) by means of Picard iteration (see section 5.1.2.1), an additional limit can be derived:

$$\Delta t_l < \frac{1}{|\beta_p| L}, \tag{2.34}$$

with L the Lipschitz continuity constant, obtained using the same Jacobian as needed to determine the stiffness ratio.

$$L = \sup\left\{ \left\| eig\left[\frac{\partial \boldsymbol{f}}{\partial x} \right] \right\| \right\} \tag{2.35}$$

The time step is also bounded by the Nyquist limit to prevent aliasing. It should be smaller than half the period of the highest frequency phenomenon to model. In general (2.33) is stronger than this Nyquist limit.

3 Modelling of electromagnetic and thermal fields in FEM

3.1 Electromagnetic field modelling

3.1.1 Maxwell equations and material characteristics

The fundamental physical equations for electromagnetic field calculations are the Maxwell equations (in differential form) [SILV]:

$$\nabla \cdot \boldsymbol{D} = \rho_{\mathrm{ch}} \quad \text{(Gauss law)} \tag{3.1}$$

$$\nabla \cdot \boldsymbol{B} = 0 \tag{3.2}$$

$$\nabla \times \boldsymbol{E} = -\frac{\partial \boldsymbol{B}}{\partial t} \quad \text{(Faraday-Lenz law)} \tag{3.3}$$

$$\nabla \times \boldsymbol{H} = \boldsymbol{J} + \frac{\partial \boldsymbol{D}}{\partial t} \quad \text{(extended Ampère's law)} \tag{3.4}$$

with			
	$\boldsymbol{E}$	[V/m]	electric field strength vector
	$\boldsymbol{D}$	[C/m²] or [As/m²]	electric flux density vector
	$\boldsymbol{B}$	[T] or [Vs/m²]	magnetic flux density vector
	$\boldsymbol{H}$	[A/m]	magnetic field strength vector
	$\boldsymbol{J}$	[A/m²]	current density vector
	ρ_{ch}	[C/m³] or [As/m³]	charge density

To define the relationship between the different field vectors, constitutive relationships, the material equations, are added to form the complete system:

$$\boldsymbol{D} = \varepsilon \boldsymbol{E} = \varepsilon_0 \varepsilon_{\mathrm{r}} \boldsymbol{E} \tag{3.5}$$

$$\boldsymbol{B} = \mu \boldsymbol{H} = \mu_0 \mu_{\mathrm{r}} \boldsymbol{H} = \frac{1}{\upsilon} \boldsymbol{H} = \frac{1}{\upsilon_0 \upsilon_{\mathrm{r}}} \boldsymbol{H} \tag{3.6}$$

$$\boldsymbol{J} = \sigma \boldsymbol{E} = \frac{1}{\rho_{\mathrm{E}}} \boldsymbol{E} \quad \text{(Ohm's law)} \tag{3.7}$$

with			
	ε	[F/m] or [As/m]	electric permittivity
	ε_0	[F/m] or [As/m]	electric permittivity of vacuum (=8.85·10^{-12} F/m)
	ε_{r}	-	relative electric permittivity

μ	[H/m] or [Vs/A]	permeability
μ_0	[H/m] or [Vs/A]	permeability of vacuum ($=4\pi\cdot10^{-7}$ H/m)
μ_r	-	relative permeability
υ	[m/H] or [A/Vs]	reluctivity tensor
υ_0	[m/H] or [A/Vs]	reluctivity of vacuum ($=1/\mu_0$)
υ_r	-	relative reluctivity
σ	[S/m] or [A/Vm]	electrical conductivity
ρ_E	[Ωm] or [Vm/A]	electrical resistivity

Often the material parameters have a non-linear field and frequency dependency. The relative permeability (and reluctivity) of ferromagnetic materials is saturable and converges to unity for high magnetic fields. Electric properties of semiconductors are dependent on the electric field. The temperature dependence of all parameters can be significant and is discussed in section 4.1.

Some magnetic materials called hard magnetic materials or permanent magnets, can establish important m.m.f. sources. For these materials, (3.6) is extended to:

$$\boldsymbol{B} = \mu\boldsymbol{H} + \boldsymbol{M} \tag{3.8}$$

with $\boldsymbol{M}$ the magnetisation. In general the *B*-*H* characteristic of ferromagnetic materials exhibits hysteresis, being significant for the hard magnetic materials. The field remaining when no external field is applied, is the remanent field B_r. The intersections of the *M*- and the *B*-curve with the horizontal axis are called coercitive fields. It is not advisable to bring the operating point *WP* to this value, since the irreversible demagnetisation starts already at lower field strengths, close to the bending point of the magnetisation curve.

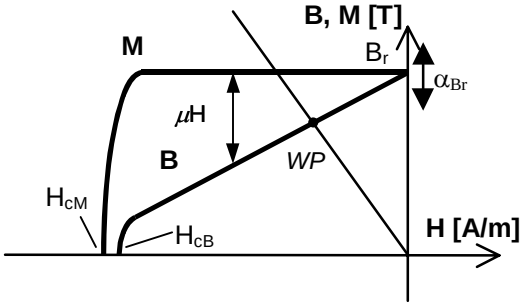

Figure 3.1 Hard magnetic material definitions

An equivalence for the internal source field phenomenon in dielectric materials is the possibility to polarise their dipoles semi-permanently; in this case a polarisation term $\boldsymbol{P}$ is added to (3.5).

3.1.2 Potential formulations

Usually, the Maxwell equations are not solved in terms of the field quantities $\boldsymbol{E}$, $\boldsymbol{D}$, $\boldsymbol{B}$ or $\boldsymbol{H}$. They are transformed into more interesting PDEs or ODEs using well-chosen potential formulations. Many potentials and related gauges exist, all with specific advantages and drawbacks [SILV], [DUL1], [BOSS]. In this work, the magnetic calculation is assumed to be performed mainly in two dimensions, often

coupled with circuit equations. In this respect, the so-called *A*-*V* potential combination is the most interesting formulation [BINN]. These potentials for the electric and magnetic field are called the magnetic vector potential $\boldsymbol{A}$ and the electrical voltage *V*, defined by:

$$\boldsymbol{B} = \nabla \times \boldsymbol{A}\,, \tag{3.9}$$

$$\boldsymbol{E} = -\nabla V\,. \tag{3.10}$$

Using (3.9), the magnetic field continuity law (3.2) is automatically satisfied. The Ampère law becomes (the subscript *s* indicates the external source quantities):

$$\nabla \times \left(\upsilon_{\mathrm{r}} \nabla \times \boldsymbol{A}\right) = \mu_0 \boldsymbol{J}_{\mathrm{s}} - \mu_0 \varepsilon_0 \varepsilon_{\mathrm{r}} \nabla\left(\frac{\partial V}{\partial t}\right). \tag{3.11}$$

The last term is the displacement current density. At low frequencies, it can often be neglected when compared to the current density source field to obtain a quasi-static field formulation. However, displacement current plays a key role in processes such as radio frequency (RF) dielectric heating.
A vector calculus identity can be used to simplify (3.11):

$$\nabla \times \left(\nabla \times \boldsymbol{A}\right) = \nabla\left(\nabla \cdot \boldsymbol{A}\right) - \nabla^2 \boldsymbol{A}\,. \tag{3.12}$$

At this point, a gauge must be introduced. This additional condition applied to the potential, is required to obtain a unique solution field. This gauge is chosen in such a way that the further equations will be simplified as well.
For quasi-static magnetic fields, the best choice is the Coulomb gauge:

$$\nabla \cdot \boldsymbol{A} = 0 \tag{3.13}$$

This simplifies (3.12) and a Poisson equation is found for the static magnetic field:

$$\nabla \cdot \left(\upsilon_{\mathrm{r}} \nabla \boldsymbol{A}\right) = -\mu_0 \boldsymbol{J}_{\mathrm{s}} = -\mu_0 \sigma V_{\mathrm{s}}\,. \tag{3.14}$$

When permanent magnets are involved, (3.14) is extended to (3.15), using (3.8). The magnetisation $\boldsymbol{M}$, present in the reluctivity υ_{r}, is moved to the right-hand side:

$$\nabla \cdot \left(\upsilon_{\mathrm{r}} \nabla \boldsymbol{A}\right) = -\mu_0 \boldsymbol{J}_{\mathrm{s}} - \mu_0 \nabla \times \boldsymbol{M}\,. \tag{3.15}$$

The Faraday-Lenz electric field law is transformed into:

$$\nabla \times \boldsymbol{E} = -\nabla \times \left(\frac{\partial \boldsymbol{A}}{\partial t}\right), \tag{3.16}$$

which is satisfied when the electric field potential for the non-static fields is extended with an induced voltage:

$$\boldsymbol{E} = -\nabla V - \frac{\partial \boldsymbol{A}}{\partial t}\,. \tag{3.17}$$

Using (3.17) and (3.7), the dynamic version of (3.14) is obtained:

$$\nabla \cdot \left(\upsilon_r \nabla \boldsymbol{A}\right) - \mu_0 \sigma \frac{\partial \boldsymbol{A}}{\partial t} = -\mu_0 \boldsymbol{J}_s = -\mu_0 \sigma V_s \tag{3.18}$$

The total current density, important for the Joule loss calculation in the conductive parts (see section 4.2.1), consists of a source and an induced (eddy) current contribution:

$$\boldsymbol{J}_{tot} = \boldsymbol{J}_s + \sigma \frac{\mathrm{d}\boldsymbol{A}}{\mathrm{d}t} = \sigma\left(V_s + \frac{\partial \boldsymbol{A}}{\partial t}\right). \tag{3.19}$$

In case of 2D fields, only the *z*-component of the magnetic vector potential, current densities and related vectors differs from zero. Then, the magnetic field equations become scalar PDEs. Therefore, in the remainder of the discussion, *A* and *J* indicate these *z*-components, unless stated otherwise.

$$\begin{aligned} \boldsymbol{A} &= (0,0,A) \\ \boldsymbol{J} &= (0,0,J) \end{aligned} \tag{3.20}$$

Gauss's law (3.1) is extended after (3.17) is substituted, in (3.5):

$$\nabla \cdot \left(\varepsilon_r \nabla V\right) = -\frac{\rho_{ch}}{\varepsilon_0} - \frac{1}{\varepsilon_0} \frac{\partial\left(\nabla \cdot A\right)}{\partial t}. \tag{3.21}$$

For the electrodynamic fields, the Lorentz gauge with the dielectric current neglected, is advantageous to decouple *A* and *V*:

$$\nabla \cdot A = -\mu \sigma V \tag{3.22}$$

This leads to a dynamic electric field equation:

$$\nabla \cdot \left(\varepsilon_r \nabla V\right) - \frac{\mu \sigma}{\varepsilon_0} \frac{\partial V}{\partial t} = -\frac{\rho_{ch}}{\varepsilon_0}. \tag{3.23}$$

This equation can further be developed into a wave equation, using the full Lorentz gauge [SILV]. A wave equation exists for *A* as well. In practice, the static electric field equation is used for many applications (see section 3.3):

$$\nabla \cdot \left(\varepsilon_r \nabla V\right) = -\frac{\rho_{ch}}{\varepsilon_0} \tag{3.24}$$

3.2 Magnetic field calculation using FEM

3.2.1 Basic equations

The complete two-dimensional dynamic magnetic field equation, using the magnetic vector potential, reduced to its *z*-component and the divergence-free gauge, containing all the discussed source terms and the often ignored displacement currents, is:

$$\nabla \cdot \left(\upsilon_{\mathrm{r}}(A,T)\nabla A\right) - \mu_0 \sigma(T)\frac{\partial A}{\partial t} = \\ -\mu_0 \sigma(T) V_{\mathrm{s}} - \mu_0 \nabla \times M(T) - \mu_0 \varepsilon_0 \varepsilon_{\mathrm{r}} \left[\frac{\partial V_{\mathrm{s}}}{\partial t} + \frac{\partial^2 A}{\partial t^2}\right] \tag{3.25}$$

The material characteristics having a significant thermal dependency are indicated by the presence of the temperature variable *T*.
The vector potential solution is a function of time. This makes the problem-own non-linearities an indirect time-function as well. The treatment of the time variable is crucial, as will be discussed extensively in sections 3.2.5 to **Error! Reference source not found.**.

3.2.2 Boundary conditions

3.2.2.1 Unary boundary conditions

As derived in section 2.3.4, the Neumann boundary condition is the natural boundary condition when FEM is used. Considering (3.9), this means that the magnetic field lines are perpendicular to the unconstrained boundaries.

The essential boundary condition, the Dirichlet condition, is mainly applied in its homogeneous form. Field lines are parallel to these boundaries.

$$A\big|_{\Gamma_D} = A_0 \,. \tag{3.26}$$

The non-homogeneous Dirichlet boundary can be used to force a prescribed flux between two non-touching boundaries. The flux ψ is determined by the following equation, after applying vector calculus and assuming no flux variation in the *z*-direction (2D field):

$$\psi = \int_S B\mathrm{d}S = \oint_L A\mathrm{d}l = L\left(A_2 - A_1\right), \tag{3.27}$$

where *L* is the distance between the two boundaries in the *z*-direction. The same equation is applicable to determine any flux linkage.

Mixed boundary conditions are well known as surface impedance conditions in the frequency domain [BINN]. They replace a semi-infinite conductive material in which eddy currents are generated due to the external alternating magnetic field. They have the complex form:

$$\frac{\partial A}{\partial n} = -\frac{1+j}{\mu_{\mathrm{r}}\delta} A \,, \tag{3.28}$$

in which the conductor's skin depth δ, within which the majority of the current is penetrating, plays a key role.

$$\delta = \sqrt{\frac{2}{\omega\sigma\mu_0\mu_r}} \,. \tag{3.29}$$

3.2.2.2 Periodic boundary conditions

In many electromagnetic field problems, a field symmetry is found, for instance pole configurations and infinite spatial repetitions. The general form of this type of boundary condition in magnetic fields is:

$$A_1 + c_1 A_2 = c_2 \tag{3.30}$$

The coefficient c_2 is in most of the practical problem definitions equal to zero. The coefficient c_1 usually equals ±1, depending on the type of (anti-)symmetry. Since the number of involved boundaries is usually two, rather than one, this condition is often referred to as 'binary boundary condition'.

3.2.3 Source term modelling: circuit coupling

3.2.3.1 Solid or stranded conductors

Due to the non-zero resistivity of conductive materials, magnetic fields exist inside the conductors. When the field is not constant with respect to time, eddy currents arise: due to the field change, a compensating current density is induced. To fulfil the requirement of a minimum of the field energy, the current density increases at the boundary of the conductor. To quantify the layer in which the major part of the current (and therefore the Joule losses) is found, the skin depth (3.29) is used. For conductors having all dimensions significantly smaller than this parameter, the current redistribution effect may be neglected. Such a conductor is often made of multiple insulated strands connected in parallel, closely together, called 'stranded' or 'filament' conductors. It can be assumed that the current is penetrating the entire cross-section area of the conductor in an equally distributed way.

The conductors in which the development of the eddy currents is allowed in the model are known as 'solid' or 'massive conductors. The consequences of this distinction are summarised in Table 3.1. Note that large errors in the Joule loss computation may be made when 'stranded conductors' experience significant external non-constant fields such as leakage fields or in situations with important proximity effects.

	Stranded Conductor	*Solid Conductor*
Equation	Eddy current term omitted, thereby locally ignoring all dynamic effects with internal or external causes.	Eddy current term included.
Electrical conductivity σ	Allowed to vary locally due to thermal effects; influencing the total current.	Allowed to vary locally due to thermal effects; this influences the local current density and as a result the total current.
Mesh requirements	Standard mesh quality requirements.	Additional mesh quality requirement: elements may not have larger dimensions than the skin depth, being frequency dependent.
Loss computation	Losses due to source currents are included. Eddy current losses due to internal currents are assumed to be negligible; eddy current losses due to external fields (leakage fields, proximity effects) are omitted and have to be calculated separately.	Joule loss caused by source currents as well as eddy currents with internal and external causes included.
Thermal model	Equivalent characteristics or different models to account for the insulation/conductor composite.	Conductor's unaltered thermal characteristics.
Circuit model (3.2.3.2)	$J_s = const.$ (3.31)	$\Delta V_s = const.$ (3.32)

Table 3.1 Overview of consequences of the stranded or solid conductor paradigm

3.2.3.2 Circuit coupling

The source term describes the externally enforced current density in the conductive materials. Therefore, it is closely related to the stranded or solid conductor approximation chosen for the conductor.

- *Stranded conductor*: If it is assumed that eddy currents are not present, the current density is therefore constant within the stranded conductor region S_{str}. The total current I_s characterises the source term within the element and is related to this current density by the number of turns N_{str} (series connected) and a filling factor f_{str}.

$$J = J_s = \frac{I_s}{f_{str}\frac{S_{str}}{N_{str}}}. \tag{3.33}$$

  The voltage across the different strands is allowed to be unequally distributed. This is possible since magnetically induced electrical fields perpendicular to the calculation plane are not compensated. The total voltage drop across a strand is composed of a resistive voltage drop due to the source term and the induced voltage. The conductor's global voltage drop is calculated using an average of the induced voltage across the stranded conductor's length:

$$\Delta V = N_{\mathrm{str}}\left[\left(\frac{l_{\mathrm{str}}}{\frac{f_{\mathrm{str}}}{N_{\mathrm{str}}}\sum_{e\subset\mathrm{str}}\left(\int_{\Omega_e}\sigma\,\mathrm{d}\Omega\right)}\right)I_{\mathrm{s}} + l_{\mathrm{str}}\sum_{e\subset\mathrm{str}}\left(\frac{1}{\Omega_e}\int_{\Omega_e}\frac{\partial A}{\partial t}\mathrm{d}\Omega\right)\right]. \tag{3.34}$$

The calculation of the first integral (calculation of an averaged conductivity) is reduced to a simple summation when a zero-order representation of the electrical conductivity within the elements is assumed. The further treatment of the second integral depends on the time discretisation.

- *Solid conductor*: In 2D models, the local current density is assumed not to change in the *z*-dimension. The voltage does not change within the cross-section of the conductor. Hence, the voltage across the conductor is:

$$\Delta V = V_{\mathrm{s}}. \tag{3.35}$$

The total current is obtained by integrating of the local current densities (3.19):

$$I = \left(\frac{1}{l_{\mathrm{sol}}}\sum_{e\subset\mathrm{sol}}\int_{\Omega_e}\sigma\,\mathrm{d}\Omega\right)V_s + \sum_{e\subset\mathrm{sol}}\int_{\Omega_e}\left(\sigma\frac{\partial A}{\partial t}\right)d\Omega. \tag{3.36}$$

These integrals are calculated numerically, taking into account the order of the shape function, the time variable representation and the characteristic of the material representation.

When the magnetic field equation is coupled to circuit equations, a condensed form of electromagnetic field equation, the external source term in (3.25) is written in terms of the voltage drop across a solid conductor or the current density through the stranded conductor. Often, these variables are unknown and determined by circuit equations.
It is common to include these circuit equations in the FEM magnetic field equation system, with the field variable integrals in (3.34) and (3.36) written as a function of the vector potentials. A separate set of algebraic non-FEM equations is added. They relate the currents and voltages by means of circuit analysis methods such as (modified) nodal analysis or signal flow graph [DEG1].

3.2.4 Static magnetic field

For the static situation, (3.25) reduces to:

$$\nabla\cdot\left(\upsilon_{\mathrm{r}}(A)\nabla A\right) = -\mu_0\sigma(T)V_{\mathrm{s}} - \mu_0\nabla\times M(T). \tag{3.37}$$

This equation matches the template (2.3). The magnetic reluctivity can be anisotropic, e.g. oriented ferromagnetic steel and permanent magnets. After applying the FEM, the following non-linear algebraic equation arises, following the methodology of section 2.3.4:

$$\boldsymbol{K}_A(\boldsymbol{A})\boldsymbol{A} = \boldsymbol{F}_A(T) + \boldsymbol{M}_A(T). \tag{3.38}$$

The matrix $\boldsymbol{M}_A$ is constructed using the magnetisation vector with components M_x and M_y in the computation plane. For an individual element, the following residual expression, altered using vector calculus, is applicable:

$$\begin{aligned} &\int_{\Omega_e} N_A \left(\frac{\partial M_x}{\partial y} - \frac{\partial M_y}{\partial x} \right) \mathrm{d}\Omega \\ &= \int_{\Omega_e} \left(M_x \frac{\partial N_A}{\partial y} - M_y \frac{\partial N_A}{\partial x} \right) \mathrm{d}\Omega - \int_{\Gamma_e} (N_A M_t) \mathrm{d}\Gamma \end{aligned} . \tag{3.39}$$

Due to the continuity of the tangential magnetic field component M_t, the last integral in (3.39), vanishes for the composition of the entire matrix $\boldsymbol{M}_A$.

3.2.5 Pure transient method

For a pure transient solution, the entire equation (3.25) must be used. Usually, the displacement current can be neglected:

$$\nabla \cdot (\upsilon_r(A) \nabla A) - \mu_0 \sigma(T) \frac{\partial A}{\partial t} = -\mu_0 \sigma(T) V_s - \mu_0 \nabla \times M(T). \tag{3.40}$$

Following the FEM methodology and applying the single step time marching scheme (2.32) with parameter θ, the non-linear algebraic system to solve for each time step becomes:

$$\begin{aligned} &\theta \left(\boldsymbol{K}_A[t_l] + \frac{\boldsymbol{H}_A[t_l]}{\Delta t} \right) \boldsymbol{A}[t_l] = \\ &-(1-\theta) \left(\boldsymbol{K}_A[t_{l-1}] - \frac{\boldsymbol{H}_A[t_{l-1}]}{\Delta t} \right) \boldsymbol{A}[t_{l-1}] \\ &+ \theta (\boldsymbol{F}_A[t_l] + \boldsymbol{M}_A[t_l]) + (1-\theta)(\boldsymbol{F}_A[t_{l-1}] + \boldsymbol{M}_A[t_{l-1}]) \end{aligned} \tag{3.41}$$

Several non-linearities, problem-own (e.g. saturation) or coupled (temperature dependence of magnet characteristics and electrical conductivities), are present in (3.41). Hence, the matrices $\boldsymbol{K}_A$, $\boldsymbol{H}_A$ and the vectors $\boldsymbol{F}_A$, $\boldsymbol{M}_A$ have to be calculated at the actual and previous time step.

The time step Δt is limited by the stability condition (2.33), which is usually stronger than the natural Nyquist limit.

When more extended LM schemes are used (e.g. higher order BDF-method for stiff problems; section **Error! Reference source not found.**), additional terms and weighting parameters are introduced. The composition of the different time terms can be computationally organised in an economical way, when the contributions are stored as long as required and re-used with other weights. Equation (3.41) can be extended with circuit equations [DEG1]. The solution of the non-linear system (3.41) is discussed in chapter 5.

3.2.6 Pure frequency domain methods

In section 2.1.2, a general discussion was given regarding the derivation of frequency domain methods. Two approaches are possible: Fourier transformation (2.9) or separation of variables (2.11). To derive the pure frequency domain methods and their approximations, the first approach is used, whereas for the transient frequency domain methods, the separation technique is more appropriate.

When applying the Fourier transformation to (3.25), including displacement current, the general steady-state frequency domain equation is obtained:

$$\begin{aligned}&\nabla\cdot\left(\mathcal{F}\left(\upsilon_{\mathrm{r}}\left(\mathcal{F}\left(A\right)\right)\right)*\nabla\mathcal{F}\left(A\right)\right)-\mu_0\sigma\left(T\right)j\omega\mathcal{F}\left(A\right)=\\&-\mu_0\sigma\left(T\right)\mathcal{F}\left(V_{\mathrm{s}}\right)-\mu_0\varepsilon_0\varepsilon_{\mathrm{r}}\left(j\omega\nabla\mathcal{F}\left(V_{\mathrm{s}}\right)+\left(j\omega\right)^2\mathcal{F}\left(A\right)\right)\end{aligned}\tag{3.42}$$

Strictly speaking, the electrical conductivity has to be Fourier transformed as well. Due to the relatively slow change of the thermal field, its spectrum can be approximated by a real-valued constant, thus avoiding a convolution in the eddy current term.

Note that permanent magnet materials are not discussed at this place, since they only posses a '*DC* source field'. In general, this equation reduces to (3.37), when ω is zero.

The displacement currents are not considered for low frequency problems, but are important in high frequency problems. When they are considered, (3.42) is simplified using a complex conductivity,

$$\underline{\sigma}=\sigma+j\omega\varepsilon\tag{3.43}$$

$$\begin{aligned}&\nabla\cdot\left(\mathcal{F}\left(\upsilon_{\mathrm{r}}\left(\mathcal{F}\left(A\right)\right)\right)*\nabla\mathcal{F}\left(\left(A\right)\right)\right)-\mu_0\underline{\sigma}\left(T\right)j\omega\mathcal{F}\left(A\right)\\&=-\mu_0\underline{\sigma}\left(T\right)\mathcal{F}\left(V_{\mathrm{s}}\right)\end{aligned}\tag{3.44}$$

Without the displacement currents, the pure electrical conductivity σ is present at the same location.

3.2.6.1 Time-harmonic method

Many electrical problems in steady state are governed by a dominant frequency ω_1: the power system's fundamental frequency or the signal carrier frequency. For these problems, only the dominant component in the Fourier spectra in (3.44) is significant:

$$\mathcal{F}\left(A\right)\approx\left\{A\left(\omega_1\right)\right\}\equiv\underline{A},\tag{3.45}$$

$$\mathcal{F}\left(V_{\mathrm{s}}\right)=\left\{V_{\mathrm{s}}\left(\omega_1\right)\right\}\equiv\underline{V}_{\mathrm{s}},\tag{3.46}$$

$$\mathcal{F}\left(\upsilon_{\mathrm{r}}\right)\approx\left\{\upsilon_{\mathrm{r}}\left(\omega=0,\mathcal{F}\left(A\right)\right)\right\}\equiv\upsilon_{\mathrm{r}}\left(\underline{A}\right).\tag{3.47}$$

The source term and the solution are replaced by a complex phasor. The saturable reluctivity is replaced by a representative constant, calculated as a function of the

field solution. To determine this non-linear relation, many methods are proposed [LUOM], [VASS]. To include the effect of iron losses, this parameter can be modelled as a complex number as well, see section 4.2.4.

Equation (3.44) now reduces to the well-known time harmonic equation, in which only one term of the convolution product remains:

$$\nabla \cdot \left(\underline{\upsilon}_{\mathrm{r}}\left(\underline{A}\right)\nabla \underline{A}\right) - \mu_0 j\omega \underline{\sigma}\left(T\right)\underline{A} = -\mu_0 \underline{\sigma}\left(T\right)\underline{V}_{\mathrm{s}} \,. \tag{3.48}$$

Following the FEM method discussion for template equations with an absorption term, the following complex non-linear algebraic equation is derived:

$$\left[\boldsymbol{K}_A\left(\boldsymbol{A}\right) + j\omega \boldsymbol{H}_A\left(\boldsymbol{T}\right)\right]\underline{\boldsymbol{A}} = \underline{\boldsymbol{F}}_A\left(\boldsymbol{T}\right). \tag{3.49}$$

Sometimes it is necessary to translate (3.49) into a real-valued system of double size (e.g. to use Newton-Raphson methods, since the complex system matrix is not directly differentiable, see section 5.1.4.2). This can be accomplished as:

$$\begin{bmatrix} \mathrm{Re}\left(\boldsymbol{K}_A + j\omega \boldsymbol{H}_A\right) & \mathrm{Im}\left(\boldsymbol{K}_A + j\omega \boldsymbol{H}_A\right) \\ -\mathrm{Im}\left(\boldsymbol{K}_A + j\omega \boldsymbol{H}_A\right) & \mathrm{Re}\left(\boldsymbol{K}_A + j\omega \boldsymbol{H}_A\right) \end{bmatrix} \cdot \begin{bmatrix} \mathrm{Re}\left(\underline{\boldsymbol{A}}\right) \\ \mathrm{Im}\left(\underline{\boldsymbol{A}}\right) \end{bmatrix} = \begin{bmatrix} \mathrm{Re}\left(\underline{\boldsymbol{F}}_A\right) \\ \mathrm{Im}\left(\underline{\boldsymbol{F}}_A\right) \end{bmatrix} \tag{3.50}$$

Equation (3.49) can be extended with circuit equations. When only solid conductors and voltage sources are present, or when only current sources and stranded conductors exist, no circuit equations are required due to the assumptions (3.31) and (3.32).

3.2.7 Domain transformations

It is difficult to restrict the magnetic field to a particular domain. Effective shielding is difficult. Ferromagnetic materials ('leading the fluxes around') and by using conductive materials for the higher frequencies ('absorbing the flux in eddy currents') can be employed for shielding applications. The ferromagnetic shields must be considered in the computation domain. The conductive shields can be replaced by the appropriate boundary condition (3.28), but then the losses in the shield cannot be computed accurately.

However, in most of the quasi-static cases, no significant shielding is present and the field should be modelled to spatial infinity. One approach is the 'closing of the field' by a boundary condition at a well-chosen distance. The correct inclusion of the infinite computation domain is required for many problems in which the leakage flux is crucial, e.g. tank-less transformers and high-current conductors.

The infinite air domain can be included in the model by transforming the field equation using a Kelvin transformation at a certain distance from the model [FRE1], [FRE2], [LOW1], [LOW2]. Air is assumed, in the external part, being a non-magnetic, non-conductive, source-free material. The magnetic equation (3.25) then reduces to the Laplace equation:

$$\nabla^2 A = 0 \,, \tag{3.51}$$

or, in polar coordinates:

$$\frac{\partial^2 A}{\partial r^2} + \frac{1}{r^2}\frac{\partial^2 A}{\partial \theta^2} + \frac{1}{r}\frac{\partial A}{\partial r} = 0\,. \tag{3.52}$$

Applying a Kelvin coordinate transformation for $r>R>0$, this homogeneous equation remains unaltered.

$$r = \frac{1}{r'} \tag{3.53}$$

The magnetic equation can therefore still be used without changes in the transformed domain. Both parts, the *R*-circle and the transformed domain are connected through binary boundary conditions (3.30).

The homogeneous Dirichlet boundary condition at infinity is replaced by the enforcement of a fixed potential inside the 'infinite' computation domain.
Similar transformations exist for half- or quarter-plane, applicable when symmetry can be used to reduce the model. Figure 3.2 shows an example of such a set of meshes.

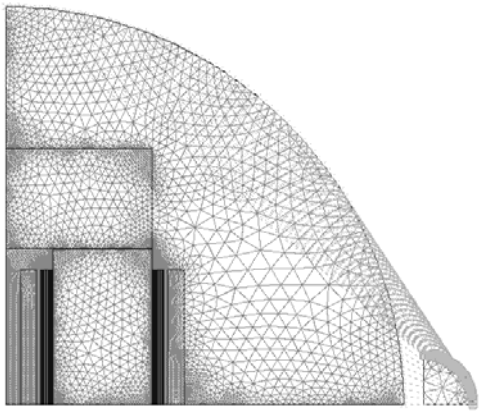

Figure 3.2 Example of the two involved meshes, connected by 'binary boundary conditions', modelling an infinite air region by the Kelvin transformation

3.2.8 Error estimators for loss computations

Error estimators have to be chosen with the simulation aim in mind. When the magnetic problem is a subproblem in a magnetic-thermal coupled problem, accurate loss computations and the material representations are important. Therefore, in every region with losses, a dedicated error estimator related to the specific losses is to be chosen. Table 3.2 summarises possible error estimators, specific for loss computations. Other types of error estimators, for instance to enforce field continuities at material boundaries, exist as well [HAM3].

Region	*Suggested error estimator*	*Discussion*
ferromagnetic region	$\lvert\Delta B\rvert$, $\Delta\lvert B\rvert^2$, possibly weighted with energy	Focus on regions with flux density changes and therefore, with changes in iron loss; the vector difference may point at rotational losses, the quadratic dependency stresses iron losses in general (smoothes the *B*-field).
solid conductor	$\lvert\Delta J\rvert$, $\lvert\Delta J\rvert^2$ or $\frac{\lvert\Delta J\rvert^2}{\sigma(T)}$	The error in the current density is found near the skin effect regions. In these locations, the differences in Joule losses are situated as well.
stranded conductor	$\frac{\lvert\Delta J\rvert^2}{\sigma(T)}$, $\lvert\Delta B\rvert$	Because of the assumed constant current density in the stranded conductors, differences in the temperature dependent Joule loss density only arise due to temperature differences. The field error (eddy current cannot force it out) is important for the loss calculation due to leakage fields.
permanent magnet	$\lvert\Delta B\rvert$	The differences in the magnetic field indicate the tendency towards irreversible demagnetisation; it is also a measure for the eddy current loss in conductive magnet materials (smoothes the *B*-field).
air gap and surrounding air	$\lvert\Delta B\rvert$	In the surrounding air, the leakage flux is importance. In air gaps in actuators, the field accuracy is important for accurate force and torque calculations (smoothes the *B*-field).

Table 3.2 Summary of error estimators in magnetic problems, coupled to thermal problems

3.3 Electric field calculation using FEM

The 3D electric field is described by the potential equations (3.23) (quasi-static or electrodynamic) and (3.24) (static). For many engineering applications, the time derivative terms can be neglected. When conductors are involved, the source term representing the charge density vanishes and it is replaced by boundary conditions of the Dirichlet type, modelling a constant-voltage surface (perpendicular to the electric field). In that case, the potential equation reduces to a Laplace equation.

$$\nabla\cdot\left(\varepsilon_{\mathrm{r}}\nabla V\right)=0 \tag{3.54}$$

$$V\big|_{\Gamma_{\mathrm{D}}}=V_0 \tag{3.55}$$

The value V_0 can be positive, zero (ground plane) or negative (Dirichlet condition). The electric field vectors at free boundary surfaces will be perpendicular to this boundary.
Binary boundary conditions are also applicable when field symmetry exists. A special subclass of the binary conditions are the 'floating potentials' in which the solution approximations on a boundary are made equal to a single degree of freedom. In electric fields, this may be the surface of a free conductor [DUL2].

The order of magnitude of ε_r ranges from 10^0 to 10^2. It is a frequency and temperature dependent value, and becomes non-linear for some special classes of materials such as semiconductors. Usually, it is represented by a diagonal tensor, as the off-diagonal coupling terms are most of the time negligible:

$$\boldsymbol{\varepsilon} = \begin{bmatrix} \varepsilon_x & 0 & 0 \\ 0 & \varepsilon_y & 0 \\ 0 & 0 & \varepsilon_z \end{bmatrix}. \tag{3.56}$$

A domain transformation, such as the Kelvin transformation, used to model semi-infinite domains is possible here as well.
The energy associated with the electric field is expressed by:

$$W_{\mathrm{E}} = \int_V \frac{\boldsymbol{D} \cdot \boldsymbol{E}}{2} \mathrm{d}V = \int_V \frac{\varepsilon |\boldsymbol{E}|^2}{2} \mathrm{d}V \,, \tag{3.57}$$

and can be used is used in the post-processing phase to determine capacitances.

Figure 3.3 shows an example of such a 3D calculation: the computation goal is to estimate the capacitive coupling between a set of crossing metal lines in different layers in a microelectronics circuit, carrying digital clock signals at high frequency. Since the structure dimensions are at least a magnitude smaller than the wavelength, a quasi-static field equation is applicable.

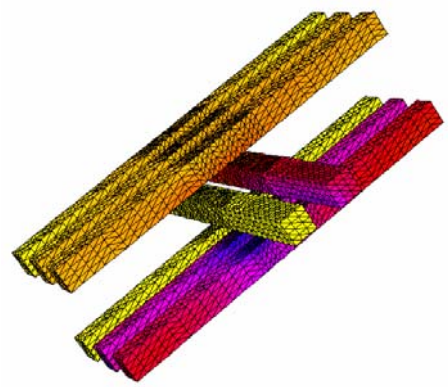

Figure 3.3 Solution of an electrostatic problem in a microelectronics circuit for determining the capacitive coupling between signal lines

Dielectric losses are associated with this field problem (section 4.2.2). The incorporation of these losses in the field model may require the use of a tensor with complex permittivities (section 4.2.4).
Local error estimators for adaptive mesh refinement can be constructed using errors in the potential distribution or its derivative (electrical field strength), possibly weighted with the local energy density. When the squared electrical field is used as error indicator, an estimation for the dielectric losses is obtained.

3.4 Thermal field calculation using FEM

3.4.1 Physical phenomena

Heat transfer occurs in three different modes [LIEN], when temperature differences are present:

- *Conduction*: transfer of kinetic energy (diffusion mechanism) between molecules or atoms in solids and fluids.
- *Convection*: energy transport caused by macroscopic movement (mass transport) in fluids in the liquid or gaseous state; the movement can be induced externally (forced convection), or caused by the buoyancy forces due to temperature differences in the fluid (free or natural convection).
- *Radiation*: energy exchange by means of electromagnetic radiation (electromagnetic waves) between surfaces in view of each other and/or through transparent structures.

To describe the heat transfer in solid structures, the conduction equations are applied. The major heat transfer mechanism at the physical boundaries of those structures is by convection or radiation.

3.4.2 Fundamental equations

A temperature gradient causes a heat energy flux $\boldsymbol{Q}$ [W/m^2], which is described by Fourier's law:

$$\boldsymbol{Q} = -\lambda \cdot \nabla T \ . \tag{3.58}$$

with λ the thermal conductivity tensor of the material, which has a positive value. Often it has a diagonal structure, with different parameters for the main axes (3.59). A typical example of such a three-dimensional anisotropic material is a laminated ferromagnetic iron core, having a different conductivity in the lamination plane, compared to the direction perpendicular to this plane.

$$\boldsymbol{\lambda} = \begin{bmatrix} \lambda_x & 0 & 0 \\ 0 & \lambda_y & 0 \\ 0 & 0 & \lambda_z \end{bmatrix} \tag{3.59}$$

The thermal energy conservation law states that a material heats up when the net outgoing heat flux is smaller than the locally produced heat density q [W/m^3]:

$$-\nabla \cdot \boldsymbol{Q} + q = \rho c \frac{\partial T}{\partial t} \tag{3.60}$$

The scalar material parameters determining the rate of change of temperature are the mass density ρ and the specific heat c. In most cases the applicable specific heat c is c_p, the specific heat at constant pressure. Substitution of (3.58) in (3.60) yields the fundamental heat conduction equation, applicable in 2D and 3D (for axisymmetric coordinates, the operators need to be adapted):

$$\nabla \cdot (\lambda \cdot \nabla T) - \rho c \frac{\partial T}{\partial t} = -q \,. \tag{3.61}$$

The heat source density q can have different physical background including electromagnetic (section 4.2), mechanical, chemical, nuclear, etc. Therefore, it is always coupled to another physical field. Often, q is a non-linear function of the temperature as well.

To obtain the steady-state temperature, the transient term is removed from (3.61) and a Poisson equation remains.

The material parameters λ and c are temperature dependent as well. Often they can be considered as constants when only a limited temperature interval is considered. However, these parameters may change significantly when a phase transition occurs. Since the conductivity mechanism is related to molecular interactions, λ changes when the transition affects the crystal structures. Figure 3.4 shows the changes which can be discontinuous close to transition temperatures, such as the Curie temperature (magnetic structure transition) and other phase changes for ST44-3 steel [CHAB], [FELI]. The transformation heat at the Curie transition is spread over an interval around this temperature, resulting in the peak-shaped curve instead of a Dirac function, in order to make this a 'softer' non-linearity for the calculation process [ZIE2].

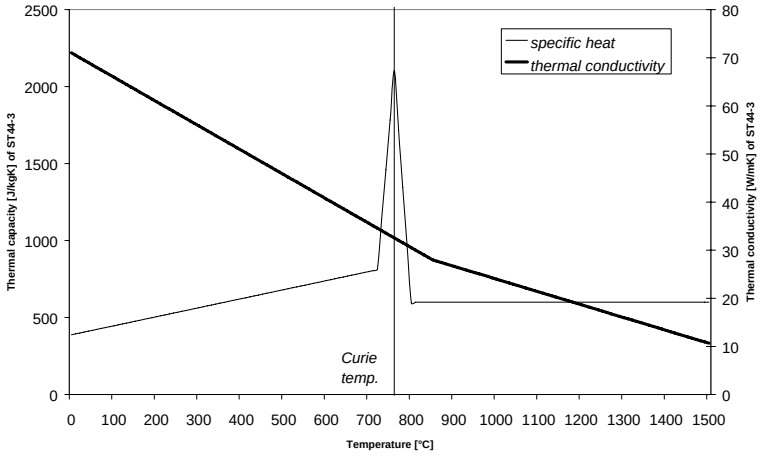

Figure 3.4 Temperature dependence of the thermal physical parameters of ST44-3 steel

Common conductor materials have a relative temperature coefficients for the thermal conductivity (α_λ) and the thermal capacitance (α_c) for the specific heat of the order of 10^{-4} K^{-1} (Table 3.3).

Material	λ *[W/mK]*	$\alpha_{\lambda,20°C}$ *[K^{-1}]*	ρ *[kg/m^3]*	*c [J/kgK]*	$\alpha_{c,20°C}$ *[K^{-1}]*
copper	394	$1.5 \cdot 10^{-4}$	8890	383	$3.35 \cdot 10^{-4}$
aluminium	208	$O(10^{-4})$	2703	897	$3.8 \cdot 10^{-4}$
(magnetic) steel	±50	$O(10^{-4})$	7780	481	$1.0 \cdot 10^{-4}$

Table 3.3 Thermal conductivity and related data for common electrotechnical materials (at reference temperature of 293 K)

When more phases are involved or when composite materials are used (e.g. insulated conductors), the following formulae can be applied to retrieve equivalent material parameters, based on the volume fractions V [STEP]:

$$\lambda^{AB} = \frac{\lambda^A V^A + \lambda^B V^B}{V^A + V^B}, \tag{3.62}$$

$$\alpha_\lambda^{AB} = \frac{\alpha^A \alpha^B \left(\frac{1}{\lambda^A V^A} + \frac{1}{\lambda^B V^B} \right) + \frac{\alpha^A}{\lambda^B V^B} + \frac{\alpha^B}{\lambda^A V^A}}{\frac{1+\alpha^A}{\lambda^A V^A} + \frac{1+\alpha^B}{\lambda^B V^B}}, \tag{3.63}$$

$$\rho^{AB} = \frac{\rho^A V^A + \rho^B V^B}{V^A + V^B}, \tag{3.64}$$

$$c^{AB} = \frac{c^A \rho^A V^A + c^B \rho^B V^B}{\rho^A V^A + \rho^B V^B}, \tag{3.65}$$

$$\alpha_c^{AB} = \frac{\alpha^A c^A \rho^A V^A + \alpha^B c^B \rho^B V^B}{\alpha^A \rho^A V^A + \alpha^B \rho^B V^B}. \tag{3.66}$$

These expressions can be used for dense stranded conductor windings, in which *A* represents the conductor and *B* the insulation, or for sheets of conductor (*A*) and insulator (*B*) materials, in the direction perpendicular to the sheets.

3.4.3 Boundary conditions

3.4.3.1 Isothermal wall

The equivalent of a Dirichlet boundary condition (2.4) associated with the PDE (3.61), is an isothermal surface. In reality this models an adjacent constant thermal reservoir with infinite thermal conductivity.

$$T\big|_{\Gamma_D} = T_D \tag{3.67}$$

This boundary condition is the essential boundary condition in the FEM method (section 2.3.4).

3.4.3.2 Prescribed heat flux and ideal insulation

Considering Fourier's law (3.58), analogous to the Neumann condition (2.5) is a constant surface heat flux:

$$-\lambda \left.\frac{\partial T}{\partial n}\right|_{\Gamma_N} = Q_N \tag{3.68}$$

The homogeneous version of (3.68) is understood to be an 'ideal insulation', an approximation for an adjacent material with an almost non-existing heat transfer capability. This homogeneous boundary condition is the natural boundary condition (section 2.3.4).

3.4.3.3 Thermal convection

The occurrence of a fluid having a different temperature next to a solid structure causes convective heat transport, either starting by itself as natural convection or externally imposed as forced convection. This mechanism is the principal heat evacuation mechanism for most energy converters. The general representation of thermal convection is:

$$-\lambda \left.\frac{\partial T}{\partial n}\right|_{\Gamma_c} = h_c\left(T - T_\infty\right), \tag{3.69}$$

with T_∞ the bulk temperature of the fluid and h_c the convection coefficient, heat transfer coefficient or film coefficient, which has a positive value. This boundary condition is a mixed condition of the type (2.6).

The major difficulty is the determination of the convection coefficient h_c. This single scalar coefficient contains the condensed information of an entire fluid flow model with mass and heat transport. In practical problems, this coefficient is calculated using dimensionless parameters ('numbers') describing the fluid conditions and containing geometrical information. For standard geometries, formulae (correlations) containing these non-dimensional parameters are published allowing the determination of h_c [LIEN], [WONG]. These correlations are obtained by extensive experimentation and analytical/numerical computations. The most important parameters are listed in Table 3.4. Many of these parameters also occur in the description of fluid mass transport, because of the close relationship of the underlying mechanism.

The correlations for the dimensionless convection coefficient are written as:

$$Nu \sim Pr^m\, Re^n\; f(\text{geometry ratio}), \tag{3.70}$$

for forced convection and

$$Nu \sim Pr^m\, Ra^n\; f(\text{geometry ratio}), \tag{3.71}$$

for natural convection; m and n are listed coefficients depending from the geometrical situation. Basically, h_c depends on the cooled or heated surface temperature (e.g. when h_c is calculated using Gr) and therefore, is a non-linear

coefficient. Throughout a simulation it can vary significantly when the flow regime changes.

Parameter ('number')	*Expression*		*Interpretation*
Nusselt	$Nu = \frac{hL}{\lambda}$	(3.72)	*Nu* is the dimensionless convection coefficient. *L* is a typical size parameter and λ is the thermal conductivity of the fluid.
Reynolds	$Re = \frac{\rho v L}{\mu_v}$	(3.73)	*Re* characterises the ratio of inertia forces and viscous forces; used to indicate the transition from laminar to turbulent flows at speed v. μ_v is the dynamic fluid viscosity.
Prandtl	$Pr = \frac{\mu_v c_p}{\lambda}$	(3.74)	*Pr* is a measure for the ratio of motion diffusion to thermal energy diffusion and is related to the size of the hydrodynamic to the thermal boundary layer.
Peclet	$Pe = Re \cdot Pr$	(3.75)	*Pe* characterises the ratio of thermal energy transport by convection and by conduction; used in forced convection.
Grashof	$Gr = \frac{g\beta_V \Delta T \rho^2 L^3}{\mu_v^2}$	(3.76)	*Gr* is interpreted as a ratio of buoyant to viscous forces; used for natural convection characterisation. *g* is the gravitational acceleration (9.81 m/s²), β_V is the volumetric thermal expansion coefficient, ΔT is the typical temperature difference.
Rayleigh	$Ra = Gr \cdot Pr$	(3.77)	*Ra* indicates the flow conditions in free convection (instead of *Re*).
Taylor	$Ta = \frac{r_a \omega_m^2 \delta^3}{\upsilon^2}$	(3.78)	*Ta* represents the ratio between centrifugal forces and viscous forces in a fluid in an annulus with radius r_a and size δ between relatively rotating cylinders at speed ω_m ('air gap' situation in rotating electrical machines).

Table 3.4 Non-dimensional parameters characterising convective heat transfer

3.4.3.4 Thermal radiation

Thermal radiation, in fact electromagnetic waves, does not require a medium for heat transfer. It becomes very important when the involved temperatures are large. The accurate modelling requires an extensive simulation including visibility, reflection and transparency at different wavelengths. The general expression for radiation is:

$$-\lambda \frac{\partial T}{\partial n}\bigg|_{\Gamma_r} = \varepsilon_e \sigma_{SB}\left(T^4 - T_\infty^4\right), \tag{3.79}$$

with ε_e the surface's emissivity (equal to unity for a black body, lower than unity for a 'grey' body) and the Stefan-Boltzmann constant σ_{SB} equal to $5.669 \cdot 10^{-8}$ W/m²K⁴. For practical purposes, (3.79) is rewritten in the same form as a convection boundary condition:

$$-\lambda \left.\frac{\partial T}{\partial n}\right|_{\Gamma_r} = h_r(T)(T - T_\infty). \tag{3.80}$$

with h_r a non-linear, temperature dependent equivalent coefficient:

$$h_r(T) = \varepsilon_e \sigma_{SB} \frac{T^4 - T_\infty^4}{T - T_\infty} \tag{3.81}$$

Using this approach, the radiation boundary condition is treated in exactly the same way as the mixed boundary condition (2.6). For boundaries subject to both convection and radiation, h_c and h_r can be added.

When different bodies radiate each other, (3.79) is written in terms of the surface temperature of both bodies and multiplied by a view factor. This parameter may be difficult to determine. This is especially true when multiple reflecting bodies are involved [LIEN], [WONG].

3.4.4 Domain transformations

To model a semi-infinite conductive domain, a Kelvin transformation with radius R can be used. However, this may be troublesome when the conductive domain is semi-infinite with a special boundary condition, as for instance, when dealing with devices, such as cables buried in the ground. When this boundary condition includes gradients (heat flux, convection or radiation), the derivative has to be transformed as well. This derivative becomes more complicated when considering the coordinate transformation (3.53):

$$\frac{\partial T}{\partial y'} = \frac{\partial T}{\partial y}\frac{\partial y}{\partial y'} = -\frac{R}{y^2}\frac{\partial T}{\partial y} \tag{3.82}$$

As a result, the boundary condition may become non-linear. This non-linearity can be approximated by a constant average in every element or a may be neglected and replaced by a global constant at a large distance.

3.4.5 Error estimators

Applicable regional error estimators for adaptive thermal mesh refinement are constructed based on differences in (average) temperature between adjacent elements. Large errors indicate significant temperature differences (possibly due to a high source term in an element) and the associated heat flow. An alternative is to estimate an error quantity using the temperature gradient, being a measure of the heat flow through the element.

4 Interaction of electromagnetic and thermal fields

4.1 Direct interaction through temperature dependent material characteristics

The thermal field affects many material properties that influence the electromagnetic fields in a direct or indirect way. These thermal dependencies occur as part of non-linear coefficients in the electromagnetic equations. It is common practice to describe this dependency in terms of a temperature difference ΔT. This difference is mainly with respect to the 'room temperature' of 20 °C or 25 °C.

$$\Delta T = T - T_{\mathrm{ref}} \tag{4.1}$$

4.1.1 Electrical characteristics: electrical conductivity

An important temperature dependent characteristic, directly affecting the electrical current distribution, is the electrical conductivity σ. Its inverse, the electrical resistivity ρ_{E}, can be approximated as a polynomial function of ΔT:

$$\rho_{\mathrm{E}} = \rho_{\mathrm{E,ref}} \left(1 + \alpha_{\rho\mathrm{E,ref}} \Delta T + \beta_{\rho\mathrm{E,ref}} \Delta T^2 + \gamma_{\rho\mathrm{E,ref}} \Delta T^3 + \ldots\right). \tag{4.2}$$

For most materials (4.2) reduces to an almost linear function. For instance, copper has a dominant first order coefficient: $\rho_{\mathrm{E,ref}}=1.7\cdot10^{-8}\ \Omega\mathrm{m}$, $\alpha_{\rho\mathrm{E,ref}}=\alpha_{\sigma,\mathrm{ref}}=2.3\cdot10^{-2}\ \mathrm{K}^{-1}$, $\beta_{\rho\mathrm{E,ref}}=-2.2\cdot10^{-6}\ \mathrm{K}^{-2}$, $\gamma_{\rho\mathrm{E,ref}}=2.9\cdot10^{-9}\ \mathrm{K}^{-3}$ [CHAB], [FELI], [BEAT]. A first order hyperbolic expression for the conductivity is obtained by:

$$\sigma = \frac{1}{\rho_{\mathrm{E}}} = \frac{\sigma_{\mathrm{ref}}}{1 + \alpha_{\sigma,\mathrm{ref}} \Delta T}\,. \tag{4.3}$$

Figure 4.1 shows the different characteristics for the polynomial and first order rational approximations for copper. Table 4.1 collects some values for common electrotechnical materials, including the electrical conductivity temperature coefficient α_{σ}.

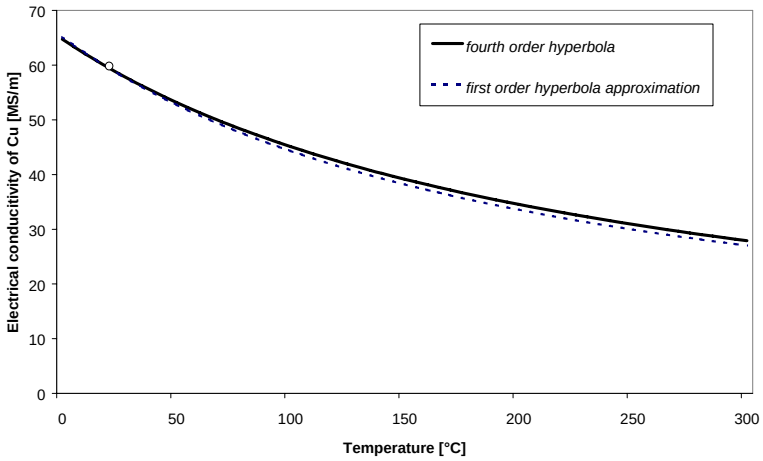

Figure 4.1 Electrical conductivity of copper

Material	σ *[Sm^{-1}]*	$\alpha_{\sigma,20°C}$ *[K^{-1}]*
copper	$5.8 \cdot 10^{7}$	$3.9 \cdot 10^{-3}$
aluminium	$3.5 \cdot 10^{7}$	$4.03 \cdot 10^{-3}$
(magnetic) steel	$3.5 \cdot 10^{6}$-$5 \cdot 10^{6}$	$4.5 \cdot 10^{-3}$

Table 4.1 Electrical conductivity and related data for common electrotechnical materials (at a temperature of 20 °C)

When a mixture of materials is used, for instance steel reinforced aluminium cables, the equivalent parameters can be found, based on the volumetric fractions of both materials *A* and *B* [STEP]:

$$\sigma^{AB} = \frac{\sigma^A V^A + \sigma^B V^B}{V^A + V^B}, \tag{4.4}$$

$$\alpha_\sigma^{AB} = \frac{\alpha^A \alpha^B \left(\frac{1}{\sigma^A V^A} + \frac{1}{\sigma^B V^B} \right) + \frac{\alpha^A}{\sigma^B V^B} + \frac{\alpha^B}{\sigma^A V^A}}{\frac{1+\alpha^A}{\sigma^A V^A} + \frac{1+\alpha^B}{\sigma^B V^B}}. \tag{4.5}$$

It can be noticed that for many materials, a relation is found between the electrical and thermal conductivity:

$$\frac{\lambda}{\sigma} \propto T. \tag{4.6}$$

The proportionality constant for metals is approximately 2.4 (slightly temperature dependent).

A special type of temperature related electrical conductivity phenomenon is superconductivity. For a special class of materials, electrical resistance vanishes at a certain low temperature. The transition to the 'regular' conductive state takes place in a very narrow temperature zone, i.e. almost discontinuously (quench) [HASH].

4.1.2 Soft magnetic characteristics: permeability

The magnetic properties of metallic materials with a small hysteresis loop (so-called 'soft magnetic' materials), such as ferromagnetic laminations, have a temperature dependent permeability. All those materials have, apart from the saturation phenomenon, a transition temperature, the Curie temperature T_C, beyond which the magnetic properties vanish. This is generally expressed by the Curie-Weiss law [MICH], relating the magnetic susceptibility and temperature [CHAB]:

$$\chi \sim \frac{1}{(T - T_C)^{\gamma_{cw}}} . \tag{4.7}$$

For many metal alloys, square root or exponential expressions can be used to evaluate the permeabilities over a wide temperature range, e.g.

$$\mu(H,T) = \mu_0 \left(1 + \sqrt{\frac{T_C - T}{T_C}} \frac{\beta_\mu}{1 + \frac{H}{\gamma_\mu}} \right) . \tag{4.8}$$

The magnetic properties evolution of magnetic steel ST44-3 is plotted in Figure 4.2. Other material properties change as well: electrical conductivity (Figure 4.2) and pure thermal properties (Figure 3.4).

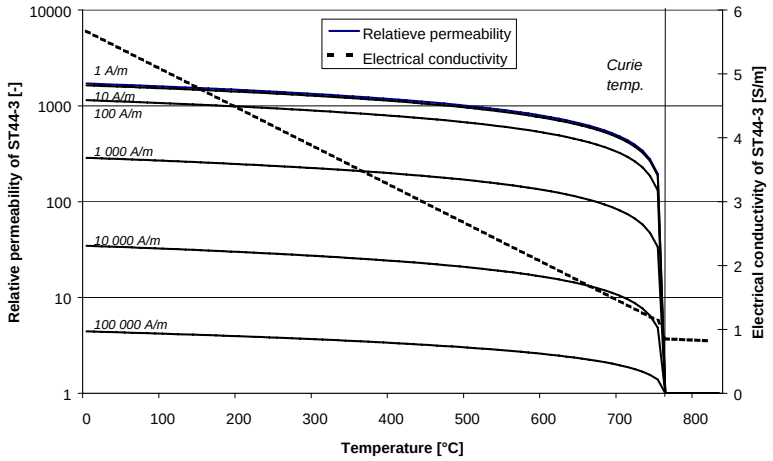

Figure 4.2 Temperature dependence of the magnetic permeability and electrical conductivity of stainless steel ST44-3

As can be noticed from Figure 4.2, the permeability (and its inverse, the reluctivity) remains almost constant over a large range in the lower temperature region.

Therefore, the magnetic properties in electric machines and energy converters are assumed to be constant in the rated operation ranges. Exceptionally, (4.8) is linearised with a temperature coefficient $\alpha_\mu \approx 0.5...1.0 \cdot 10^{-6}\,\mathrm{K}^{-1}$, valid for most ferromagnetic materials [MICH]. In electrothermal applications, such as induction heating devices, the Curie transition has to be considered (e.g. [CHAB], [DUGH], [TMAT]).

4.1.3 Hard magnetic characteristics

Permanent magnets are magnetic materials or composites with a wide hysteresis loop, resulting in an important remanent field. For these types of materials, the changing hysteresis loop in the second *B*-*H* quadrant needs to be considered [CHEN], [MICH].
In Figure 4.3, the influence of the temperature on the magnetisation characteristic of NdFeB is shown. Both the magnetisation and the magnetic induction are plotted. It is, in fact, the magnetisation which is the temperature dependent quantity. Its characteristic shifts almost parallel downwards with rising temperature. Moreover, the point at which the irreversible demagnetisation continues, shifts to applied field values with a lower absolute magnitude for rare-earth magnets or to a higher absolute magnitude for ferrite magnets. The consequence of this is that the range of safe operation is limited at higher temperatures.

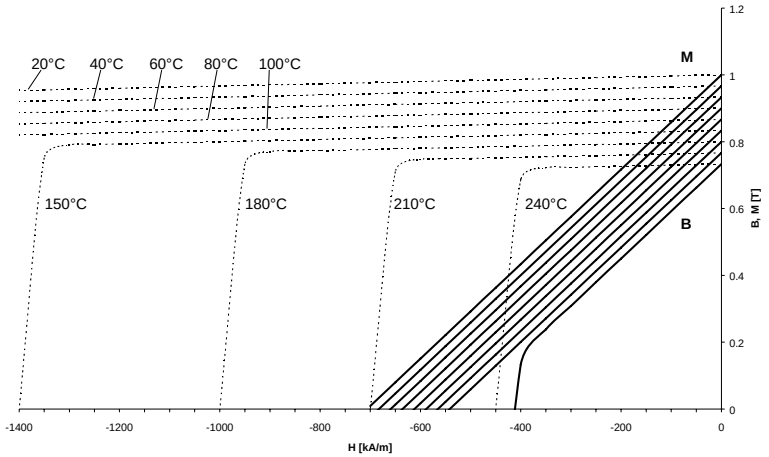

Figure 4.3 Sample NdFeB temperature dependent magnetisation characteristic.

To quantify the temperature influence, a set of relative temperature coefficients is defined in Figure 4.4. H_c^* is the linear extrapolation of the *B*-*H*-curve, beyond the irreversible demagnetisation point. The temperature coefficient associated with this extrapolated coercitive field, α_{Hc}^*, is important for the FEM modelling, since the magnetisation characteristic is assumed to be linear. In a post-processing step, it is checked whether demagnetisation occurred for that temperature. Because of the almost parallel shift, α_{Hc}^* can be assumed equal to α_{Br}, the temperature coefficient associated with the remanent field. Therefore, this parameter becomes the most important parameter with respect to the coupled thermal problem.

$$\alpha_{B_r} = \frac{B_r - B_{r,T_{ref}}}{B_{r,T_{ref}}\left(T - T_{ref}\right)} \tag{4.9}$$

$$\alpha_{H_{cJ}} = \alpha_{H_{cB}} = \frac{H_{cB/J} - H_{cB/J,T_{ref}}}{H_{cB/J,T_{ref}}\left(T - T_{ref}\right)} \tag{4.10}$$

$$\alpha_{H_c^*} = \frac{H_c - H_{c,T_{ref}}^*}{H_{c,T_{ref}}^*\left(T - T_{ref}\right)} \approx \alpha_{B_r} \tag{4.11}$$

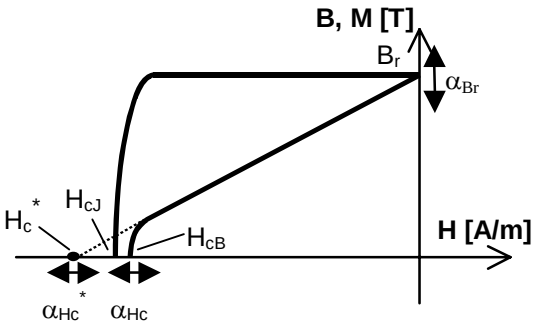

Figure 4.4 Temperature coefficients definitions for permanent magnet materials

The parameters α_{Br} and α_{Hc}^* are always negative. The parameter α_{Hc} may have a different sign, depending on the material family behaviour: it is negative for rare-earth magnets (higher demagnetisation risk for increasing temperatures) and positive for ferrite magnets.

For the major permanent magnet material families, typical values are given in Table 4.2. The electrical conductivity is mentioned since it is important for the magnets' internal loss mechanism, mostly Joule losses due to eddy currents, when they are subject to non-constant external magnetic fields. The other parameters are important for the thermal field modelling.

Material	*Ferrite*	*AlNiCo*	*SmCo*	*NdFeB*
B_r [T]	0.4	0.9	1.0	1.0
α_{Br} [K^{-1}]	$-2\cdot10^{-3}$	$-2\cdot10^{-4}$	$-3\cdot10^{-4}$	$-1\cdot10^{-3}$
H_c [kA/m]	300	50	760	760
α_{Hc} [K^{-1}]	$+3\cdot10^{-3}$	$-7\cdot10^{-4}$ - $+3\cdot10^{-4}$	$-2\cdot10^{-3}$ - $-3\cdot10^{-3}$	$-5\cdot10^{-3}$
μ_r [-]	1.1	1.5 –3.0	1.1	1.1
λ [W/mK]	2 - 4	10 - 100	12	9
ρ [kg/m^3]	5000	7000	8400	7500
c [J/kgK]	800	350 - 500	390	440
T_C [°C]	450	800 - 900	800	300
T_{max} [°C]	200	500	300	200
σ [$\Omega^{-1}m^{-1}$]	≈0 (10^{-6})	$2\cdot10^6$	$1.25\cdot10^6$	$0.7\cdot10^6$

Table 4.2 Indicative permanent magnet material data (at 20 ºC)

Considering Table 4.2, one may conclude that in general SmCo and AlNiCo are the most temperature resistant magnet materials when it comes to extremal temperatures, but AlNiCo requires longer magnets due to the small H_c. NdFeB has a very good magnetic performance, is cheaper than for instance SmCo, but cannot sustain high temperatures, though new material evolutions will extend its limits.

All but the polymer bonded ferrite magnets have a significant electrical conductivity, therefore exhibiting loss generating eddy current when submitted to an external non-constant field.

4.1.4 Phase transformations

When phase transformations are to be considered, the thermal and coupled electromagnetic-thermal problems become more complicated. This is the case for heating of metal alloys, for example steel alloys having phase fractions of ferrite, pearlite, austenite, bainite, martensite, … depending on temperature and the material's history.

For steady-state solutions, it is important to know what the transition temperatures are. To obtain steady-state solutions, appropriate relaxation techniques are required to cope with the discontinuous characteristics. At first, the discontinuities are replaced by continuous linear changes, with a slope steeper towards the end of the calculation process, to enhance the convergence of the non-linear calculation loop.
To obtain transient solutions, the kinetics behind the transformation need to be considered (e.g. [JACO] for an induction heating). The changes of the relative volume fractions of the different phases are modelled by time and temperature dependent equations:

$$V = V_{\mathrm{ph,max}}(T)\left[1 - \exp\left(-\beta_{\mathrm{ph}}(T)t^{n_{\mathrm{ph}}}\right)\right], \tag{4.12}$$

where $V_{\mathrm{ph,max}}$ is the maximum volume fraction at thermodynamic equilibrium; β_{ph} and n_{ph} are material kinetic parameters, modelling the crystallographic processes.

4.2 Direct interaction through loss calculation

4.2.1 Joule losses

4.2.1.1 Joule loss expressions

Joule losses are present in every current carrying conductor (non-superconductor). The Joule loss density q_{Joule} is given by:

$$q_{\text{Joule}} = \frac{J_{\text{tot}}^2}{\sigma}. \tag{4.13}$$

To know the Joule loss density within a prescribed volume or area of the cross-section of a conductor, more in particular a finite element, (4.13) is integrated over that area Ω_e:

$$q_{\text{Joule},\Omega_e} = \frac{1}{\Omega_e}\int_{\Omega_e}\frac{J_{\text{tot}}^2}{\sigma}\,\mathrm{d}\Omega. \tag{4.14}$$

When the total current density within the area of interest is described by voltage, both applied and/or induced, the Joule loss becomes:

$$q_{\text{Joule},\Omega_e} = \frac{1}{\Omega_e}\int_{\Omega_e}\sigma\left(V_{\text{s}} + \frac{\partial A}{\partial t}\right)^2\mathrm{d}\Omega. \tag{4.15}$$

When the sources and eddy current contribution are studied in the frequency domain, containing a single frequency, the loss integral becomes expression (4.16) (" * " indicates the complex conjugate). Similar expressions are developed for current densities calculated as spectra (convolved harmonic series, see section 3.2.6) or 'envelope' functions (see section **Error! Reference source not found.**).

$$q_{\text{Joule},\Omega_e} = \frac{1}{\Omega_e}\int_{\Omega_e}\sigma\left(V_{\text{s}} + j\omega\underline{A}\right)\left(V_{\text{s}}^* - j\omega\underline{A}^*\right)\mathrm{d}\Omega \tag{4.16}$$

$$q_{\text{Joule},\Omega_e} = \frac{1}{\Omega_e}\int_{\Omega_e}\sigma\left(\left\{V_{\text{s},h} + j\omega\underline{A}_h\right\}_h * \left\{V_{\text{s},h}^* - j\omega\underline{A}_h^*\right\}_h\right)\mathrm{d}\Omega \tag{4.17}$$

$$q_{\text{Joule},\Omega_e} = \frac{1}{\Omega_e}\int_T\int_{\Omega_e}\sigma\left(V_{\text{s}} + j\omega\underline{A} + \frac{\partial\underline{A}}{\partial t}\right)\left(V_{\text{s}}^* - j\omega\underline{A}^* + \frac{\partial\underline{A}^*}{\partial t}\right)\mathrm{d}\Omega\,\mathrm{d}t \tag{4.18}$$

Basically, the Joule loss is a function of time since the integrand is time dependent as well. If the current is sinusoidal at frequency f, the Joule loss contains a constant term and a term at frequency $2f$. However, q_{Joule} is perceived to be a constant in time, which is explained by the fact that losses are understood as 'thermal

phenomena' associated with large time constants. Therefore, the double frequency contribution can be omitted, since for the long-term, compared to the period of the loss function, the non-constant terms have no effect. In fact, all that matters is the locally averaged heat source density. Only when the solution is written as an 'envelope' with time constants having the magnitude of the thermal time constants, an averaging integration in time may be required in (4.18), though these time derivatives usually only deliver small contributions.
Although both terms 'Joule loss' and 'eddy current loss' are frequently used, it is theoretically not possible to separate the contributions of source and eddy currents in (4.15) - (4.18), since both feature as part of the squared total current. Therefore, the term 'eddy current loss' should be used with care and only for the occasions without imposed source voltage, such as massive conductors.

4.2.1.2 Joule loss calculation in FEM

When the magnetic field and circuit solutions in (4.15)-(4.18) are obtained using the FEM, the surface or volume integral (4.15) becomes, assuming the temperature dependent electrical conductivity to be a constant (zero-order shape functions) within the element:

$$q_{\mathrm{Joule},\Omega_e} = \frac{\overline{\sigma}}{\Omega_e} \int_{\Omega_e} \left(V_\mathrm{s} + \sum_{k=1}^{m_k^A} N_k \frac{\partial A_k}{\partial t} \right)^2 \mathrm{d}\Omega \,. \tag{4.19}$$

The square in the integrand can be expanded further yielding simpler analytically integrable terms. Since this soon becomes a complicated operation for higher element orders, it is more interesting to integrate (4.19) numerically using weighted function evaluations in sample points (Gauss points).

$$q_{\mathrm{Joule},\Omega_e} = \frac{\overline{\sigma}}{\Omega_e} \sum_{p=1}^{n_\mathrm{G}} w_\mathrm{G}(p) \left(V_\mathrm{s} + \sum_{k=1}^{m_k^A} N_k(p) \frac{\partial A_k(p)}{\partial t} \right)^2 \tag{4.20}$$

The order of the integrand is twice the order of the finite element representation. When the field within the element evolves smoothly, for instance when the element is small enough, the current density can be approximated as a constant $\overline{J_\mathrm{eq}}$. Expression (4.14) reduces to:

$$q_{\mathrm{Joule},\Omega_e} = \frac{\overline{J_\mathrm{eq}}^2}{\overline{\sigma}} \,. \tag{4.21}$$

Despite the apparent loss in accuracy, some black-box solver programs only possess the possibility to produce lists of an averaged current density per element. In this case, (4.21) is the only practical expression to approximate the Joule loss density.
The integral (4.15) becomes more complicated when the material is represented by a finite element approximation as well (see section **Error! Reference source not found.**):

$$q_{\mathrm{Joule},\Omega_e} = \frac{1}{\Omega_e}\int_{\Omega_e}\left(\sum_{k=1}^{m_k^\sigma} N_k^\sigma \sigma_k\right)\left(V_\mathrm{s} + \sum_{k=1}^{m_k^A} N_k^A \frac{\partial A_k}{\partial t}\right)^2 \mathrm{d}\Omega \tag{4.22}$$

Considering the solid/stranded conductor paradigm discussed in section 3.2.3, often the Joule loss integrals can be simplified: the stranded conductor is assumed to have a constant current density. Its losses also have to be calculated, considering the filling factor.

However, not all the Joule losses occurring in a stranded conductor are calculated. A problem arises when strong leakage fields pass through the stranded conductor (e.g. transformer coils). Due to the limited strand cross-section, they are not influenced macroscopically, but small local eddy currents cause extra losses in individual strands. To account for these additional losses, a separate set of correction factors, function of the local flux density, are calculated in a detailed FEM model of an individual conductor present in the stranded conductor, in which it is treated as a little solid conductor (section **Error! Reference source not found.**).

4.2.2 Dielectric losses

In non-ideal dielectric materials subject to time dependent electric fields at frequency *f*, dielectric losses are generated [META], [ORFE]. The dielectric loss density q_{diel} in an electric field with pulsation ω is expressed using the loss angle δ_E or an imaginary component of the complex permittivity $\varepsilon_{\mathrm{im}}$:

$$q_{\mathrm{diel},\Omega_e} = \frac{1}{\Omega_e}\int_{\Omega_e}\omega\varepsilon_0\varepsilon_\mathrm{r}\tan\left(\delta_\mathrm{E}\right)E^2\,\mathrm{d}\Omega = \frac{1}{\Omega_e}\int_{\Omega_e}\omega\varepsilon_{\mathrm{im}}E^2\,\mathrm{d}\Omega\,. \tag{4.23}$$

This integral can be treated in the same way as the Joule loss integral (4.14). The loss angle can also be interpreted as a delay between the *D* and *E* field.

4.2.3 Iron losses

Iron losses are a generic name for loss phenomena connected to non-constant magnetic fields present in ferromagnetic, often laminated, materials. They are split in pure hysteresis losses, associated with the magnetic hysteresis loop, and dynamic iron losses due to local eddy currents. The latter occur due to the fact that ferromagnetic materials are almost always electrically conducting as well. The dynamic losses themselves are distinguished in classical (macroscopic) Joule (eddy current) losses and excess or anomalous losses representing the loss contribution due to the motion of magnetic domain walls and interactions of the domain walls with the crystal lattice.

$$q_{\mathrm{tot}} = q_{\mathrm{hys}} + q_{\mathrm{dyn}} = q_{\mathrm{hys}} + \left(q_{\mathrm{class}} + q_{\mathrm{exc}}\right) \tag{4.24}$$

The local magnetic field vectors can be simply oscillating in magnitude (indicated as alternating) or rotating. Both modes call for different calculation methods to obtain the global combined elliptical field loss:

$$q^{\mathrm{ellipt}} = q^{\mathrm{alt}} + q^{\mathrm{rot}} \tag{4.25}$$

The terms in (4.24) and (4.25) are discussed individually in the following sections, based on a large history of research [SAIT]. Where necessary, a distinction is made between sinusoidal and non-sinusoidal flux patterns.

This subject is treated from the point of view of the need for fast, practical, but accurate calculations. There is no doubt that better models are available than those presented here, for instance the scalar and vector Preisach and the Jiles-Atherton models, but they require far more time-consuming computational efforts [DUPR] [JILE]. Moreover, these more complicated models are only justified when iron losses form a substantial part of the overall losses in a magnetic device, which is not always the case.

Another limitation of the accurate iron loss calculations is the lack of sufficiently accurate material parameters. It is not always possible to analyse material samples in dedicated measuring setups and manufacturer supplied data (formulae, look-up tables) have to be used.

4.2.3.1 Hysteresis loss term

The hysteresis loss density is linked to the surface within the B/H characteristic followed in a period T (Figure 4.5) of the local magnetic field vectors:

$$q_{\text{hyst}} = \frac{1}{T}\int_T \boldsymbol{H}\,\mathrm{d}\boldsymbol{B}\,. \tag{4.26}$$

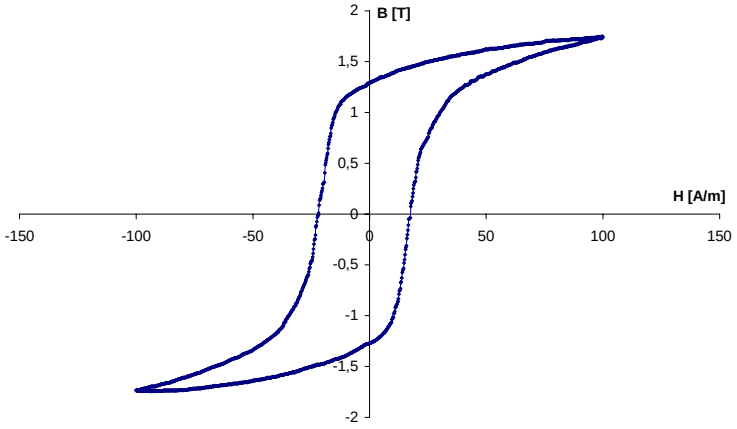

Figure 4.5 Typical course of the magnetisation characteristic of ferromagnetic material used for core lamination

The hysteresis loss density can be split into an alternating and a rotating component:

$$q_{\text{hyst}}^{\text{ellipt}} = \frac{1}{T}\int_T \left|\boldsymbol{H}\right| \frac{\mathrm{d}\left|\boldsymbol{B}\right|}{\mathrm{d}t}\,\mathrm{d}t + \frac{1}{T}\int_T \omega\left(\boldsymbol{H}\times\boldsymbol{B}\right)_z\,\mathrm{d}t\,. \tag{4.27}$$

The magnetic hysteresis phenomenon is also visible on the time plot of B and H. Saturation harmonics in H are clearly visible. Hysteresis is presented by a time lag t_d between the fundamentals of both waveforms:

$$H(t) = \upsilon B(t + t_\mathrm{d}) \tag{4.28}$$

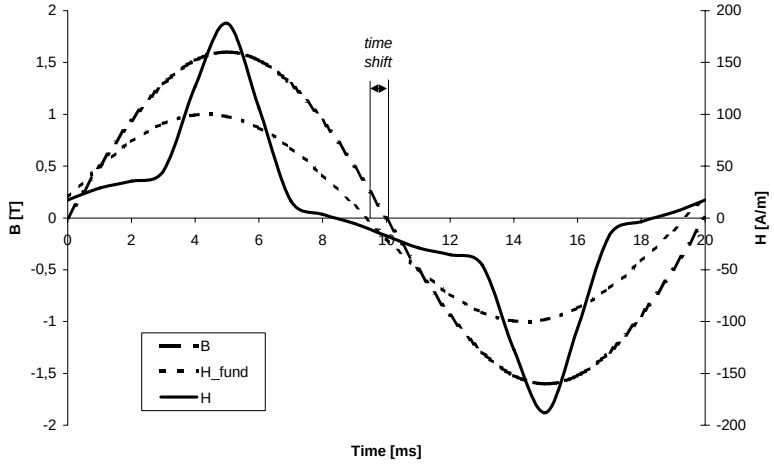

Figure 4.6 Time evolution of *B*, *H* and the fundamental wave of *H*; the time shift is indicated

In the frequency domain the equivalent of this delay is the hysteresis angle θ_B, a function of B due to the saturation. Using this quantity, a frequency dependent complex reluctivity is defined [NIEM]:

$$\underline{H} = \left(\upsilon e^{j\omega t_\mathrm{d}}\right)\underline{B} = \left(\upsilon e^{j\theta_\mathrm{B}}\right)\underline{B} = \underline{\upsilon}\,\underline{B}\,. \tag{4.29}$$

Equation (4.27) can be rewritten in terms of θ_B:

$$q_\mathrm{hyst}^\mathrm{ellipt} = \frac{1}{T}\int_T \left(HB\sin\theta_\mathrm{B} + H\cos\theta_\mathrm{B}\frac{\partial B}{\partial \varphi_\mathrm{B}} - HB\sin\theta_\mathrm{B}\frac{\partial \theta_\mathrm{B}}{\partial \varphi_\mathrm{B}}\right)\mathrm{d}t \tag{4.30}$$

with φ_B the phase angle of the rotating B. The first term in the integrand indicates the alternating hysteresis loss, while the second term is related to the rotating losses. The last term refers to the non-linearity of the loss angle. However, it is not always possible to use closed expressions such as (4.27) and (4.30), since the hysteresis loss angle is often unknown.

More often expressions based on the Steinmetz equation (4.31) are used. They give the hysteresis loss density as a function of the peak value $\hat{B}$ of the flux density:

$$p_\mathrm{hyst} = C_\mathrm{h} f \hat{B}^{n_\mathrm{St}} \tag{4.31}$$

with $n_\mathrm{St}\approx 1.6$ for many steel types [MICH]. When the flux is non-sinusoidal, the hysteresis track is not followed as indicated in Figure 4.5. Minor loops may arise

locally. In this case, the losses increase. A correction factor is then added to (4.31). It is a function of the magnitudes B_i of the local loops [LIU1]:

$$p_{\mathrm{hyst}} = K_{\mathrm{h}} C_{\mathrm{h}} f \hat{B}^n \,, \tag{4.32}$$

with:

$$K_{\mathrm{h}} = 1 + \frac{0.6 \ldots 0.7}{\hat{B}} \sum_i \Delta B_i \,. \tag{4.33}$$

Alternatively, other weighting functions have been proposed as well [ARKK].

Theoretically, these equations are only valid for alternating fluxes, but often are used as an approximation for elliptic losses [LIU1]. In general, the hysteresis loss for circular flux requires a different expression or experimentally obtained values. Elliptic losses are then calculated as a weighted sum of an alternating and a circular loss, for every harmonic. The weighting factor is a function of the ratio of the major and minor axes of the ellipse:

$$q_{\mathrm{hyst}}^{\mathrm{ellip}} = \sum_h \left(\frac{B_{h,\min}}{B_{h,\mathrm{maj}}} q^{\mathrm{circ}} + \left(1 - \frac{B_{h,\min}}{B_{h,\mathrm{maj}}} \right)^2 q^{\mathrm{alt}} \right). \tag{4.34}$$

The circular loss is expressed as a multiple of the alternating loss, allowing the transformation of (4.34) into a simpler expression, with a measured parameter r_{ca}.

$$q^{\mathrm{circ}} = r_{\mathrm{ca}} q^{\mathrm{alt}} \tag{4.35}$$

4.2.3.2 Classical eddy current loss term

The classical eddy current loss term is a local Joule loss in the electrically conductive ferromagnetic material. It is calculated assuming a constant flux density amplitude over the (thin) cross section d of the lamination. The metal sheet is assumed to be perfectly electrically insulated (e.g. by the coating) from the adjacent lamination sheets:

$$q_{\mathrm{class}}^{\mathrm{alt}} = \frac{\sigma d^2}{12} \frac{1}{T} \int_T \left(\frac{\partial B}{\partial t} \right)^2 \mathrm{d}\, t \,. \tag{4.36}$$

When the coating is conductive, additional intersheet eddy currents may arise. In case of a sinusoidal flux, this reduces to:

$$q_{\mathrm{class}}^{\mathrm{alt}} = \frac{\pi^2 \sigma d^2 f^2}{6} B^2 \,. \tag{4.37}$$

When the flux is periodic, the effect of the different harmonics can be combined in a local linear phenomenon using:

$$q_{\mathrm{class}}^{\mathrm{alt}} = \frac{\pi^2 \sigma d^2 f^2}{6} \sum_h h^2 B_h^2 \,. \tag{4.38}$$

For elliptic losses, this expression is extended to:

$$q_{\text{class}}^{\text{ellip}} = \frac{\pi^2 \sigma d^2 f^2}{6} \sum_h h^2 \left(B_{h,\text{maj}}^2 + B_{h,\text{min}}^2 \right). \tag{4.39}$$

The most general expression taking into account the change of the magnetic field density as a vector, is:

$$q_{\text{class}}^{\text{ellip}} = \frac{\sigma d^2}{12} \frac{1}{T} \int_T \left[\left(\frac{\partial B_x}{\partial t} \right)^2 + \left(\frac{\partial B_y}{\partial t} \right)^2 \right] dt \, . \tag{4.40}$$

This expression requires the full knowledge of the magnetic trajectory to be evaluated by numerical time integration.

$$q_{\text{class}}^{\text{ellip}} = \frac{\sigma d^2}{12} \frac{1}{N} \sum_{i=1}^{N} \left[\left(\frac{\Delta B_x}{\Delta t} \right)^2 + \left(\frac{\Delta B_y}{\Delta t} \right)^2 \right], \tag{4.41}$$

with N the number of discrete time steps.

4.2.3.3 Excess loss term

The excess loss term is more difficult to quantify because of the complicated underlying mechanism. For sinusoidal fluxes, it is often represented by [ZHU]:

$$q_{\text{exc}}^{\text{alt}} = 8.7634 \, C_{\text{e,a}} \left(\hat{B} f \right)^{3/2}, \tag{4.42}$$

or, for a non-sinusoidal flux:

$$q_{\text{exc}}^{\text{alt}} = \frac{C_{\text{e,a}}}{T} \int_T \left| \frac{\partial B}{\partial t} \right|^{3/2} \mathrm{d}t \, . \tag{4.43}$$

The most general expression, to be used for an elliptic flux:

$$q_{\text{exc}}^{\text{ellip}} = \frac{C_{\text{e,r}}}{(2\pi)^{3/2}} \frac{1}{T} \int_T \left[\left(\frac{\partial B_x}{\partial t} \right)^2 + \left(\frac{\partial B_y}{\partial t} \right)^2 \right]^{3/4} dt \tag{4.44}$$

This expression is evaluated numerically as in (4.41).

As is the case with the hysteresis loss expressions, these excess loss functions require the knowledge of material parameters, which is not always available. Therefore, many approximations are made for the computations, for instance equating the loss coefficient for rotating ($C_{\text{e,r}}$) and the alternating ($C_{\text{e,a}}$) excess loss [LIU1].

4.2.4 Incorporation of loss terms in electromagnetic FEM methods

The losses influence the electromagnetic field since they represent a physical energy dissipation. For instance, in magnetic devices, an active current component is connected to the iron losses (in-phase component of the magnetisation current).
Obviously Joule losses and the associated current components are included in the magnetic equation through the eddy current and source current terms.
The incorporation of the iron and dielectric losses is less obvious [JANS], [RAPP]. Material equations relating B and H, and D and E respectively, should be used in their time delayed form, such as (4.28) for the hysteresis losses, in the derivation of the formulations in sections 3.2 and 3.3. For frequency domain formulations, complex material tensors $\underline{\upsilon}$ and $\underline{\varepsilon}$ with imaginary components based on the relevant frequency, such as in (4.29), are applicable.

The use of these complex material parameters alters nothing regarding the FEM methodology, the same integral expressions remain applicable. The symmetry properties are maintained [NIEM], [LED1]. The use of a constant magnetic loss angle can be interpreted as an elliptic approximation of the magnetic hysteresis characteristic.

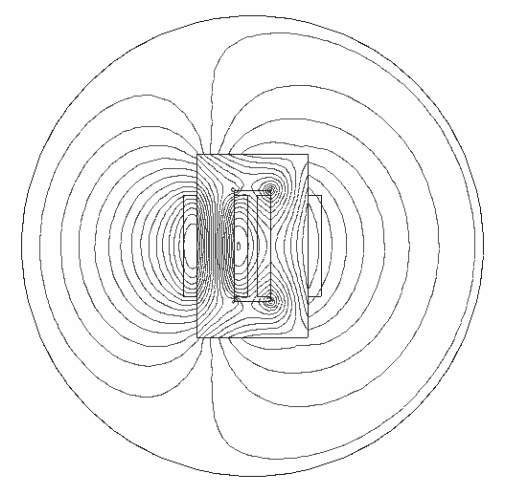

Figure 4.7 Real component field of a no-load simulation of a single phase transformer associated with the iron losses, modelled using a complex reluctivity

Figure 4.7 shows the real component of a no-load simulation of a single phase transformer, with the voltage having a zero phase angle, leading to an imaginary main flux. This real component of the field is completely associated with the iron loss: the field lines concentrate in the iron around the saturated corners (higher iron losses).

The redefinition of the material property leaves open a possibility to incorporate more than just the hysteresis iron losses. The loss angle can be generalised for sinusoidal (elliptic) conditions using:

$$\theta_{\mathrm{P}}(B) = \arcsin\left(\frac{q}{2\pi\mu B^2}\right). \tag{4.45}$$

The loss density q may include dynamic losses as well. The denominator represents the surface elliptically approximated hysteresis loop. The use of (4.45) is obviously limited to expressions with a ratio of loss density to elliptic surface smaller than one.

An alternative approach is to add concentrated equivalent loss resistances, though this does not reflect the continuous nature of the loss mechanisms.

Regarding the rotational losses, one has to consider the limitations of the time modelling. When purely transient approaches are used, numerical integrations, such as (4.41), are applicable. All changes of the field vectors can be modelled, limited by the Nyquist criterion (the maximum frequency taken into account equals half the 'sampling frequency', equal to the inverse of the time-step).

When frequency domain methods are used, it is implicitly assumed that field quantities such as the vector component B_x and B_y have a sinusoidal time evolution. As a consequence, only 'soft' spatial elliptical field changes can be modelled. Therefore, iron losses based on frequency domain methods, as an approximation for complex field evolution as found with power electronics sources (e.g. PWM), are underestimated since loss generating field patterns such as minor loops are lost.

4.3 Indirect interactions

4.3.1 General: indirect coupled field influence

The most important indirect interactions are found in the subproblem's non-linear coefficients, depending on the same subproblem's solution (section 2.1.3). The aim of a coupled calculation is to calculate the field considering the influence of other fields. Therefore, by definition, when the subproblem solution is corrected, the subproblem's own non-linearities change as well. Nevertheless, this indirect influence is often neglected and calculations with 'fixed' non-linearities determined in the beginning of the computation process are made. For instance, a magnetic saturation state is calculated using an initial non-linear subproblem solution. Consequently, linear models are used with the saturation fixed and the magnetic field changes due to thermally induced electrical conductivity corrections. Basically, this is a less accurate attitude and re-iteration is required.

4.3.2 Thermal expansion

Thermal expansion is a mechanical phenomenon. It indirectly influences electromagnetic fields because the dimensions in the computation domain change. Usually, the deformation is small and it will only result in material stress. Except for electrothermal heating considering a large temperature range, this influence is negligible. Alternatively, the temperature coefficients could be corrected; e.g., a conductor that is freely expandable in all directions [SERW]:

$$\sigma = \frac{\sigma_{\text{ref}}}{\left(1+\alpha_{\sigma,\text{ref}}\Delta T\right)\left(1+\kappa_{\text{l}}\Delta T\right)} \approx \frac{\sigma_{\text{ref}}}{\left(1+\left(\alpha_{\sigma,\text{ref}}+\kappa_{\text{l}}\right)\Delta T\right)}, \tag{4.46}$$

with κ_{l} the linear thermal expansion coefficient. For copper the ratio of the conductive coefficient and the expansion coefficient is $4.3 \cdot 10^{-3}/17 \cdot 10^{-6}$ K^{-1}, equal to 253 K^{-1}. Therefore, almost no error is made when thermal expansion is ignored.
A similar reasoning can be made about the influence of thermal parameters on the mass density in the thermal equation.

4.3.3 Mechanical losses

A class of losses indirectly related to electromagnetic fields are the motion related losses. These are related to the macroscopic mechanical description of the system, in which these losses are represented by their equivalent force or torque. The most common motion related losses are:

- *friction and ventilation losses:* The movement relative to the fluid (mostly air) causes friction and associated heat production. When the air movement is induced for cooling purposes, these losses are called ventilation losses. These types of losses are very important for high-speed machines [SAAR].
- *bearing losses:* The bearings are subject to internal friction. The associated losses play an important role in the heat management of rotating machines and contribute to the temperature rise of the rotor and shaft.

4.4 Conclusion

The electromagnetic field depends directly on the temperature distribution through changing material characteristics. In particular, the electrical conductivities and characteristics of permanent magnets are temperature sensitive.

The direct sources in the thermal field of electromagnetic nature are discussed.
The currents, both source as well as eddy current densities, cause Joule losses. These are calculated by numerical integration over the set of finite elements in the conductive region.
Iron losses, consisting of hysteresis, eddy currents and additional losses, are approximated by numerically integrating the reconstructed evolution in time of the magnetic field vector. These losses are incorporated in the magnetic field calculation by using loss angles and complex material properties.

Indirect interactions are present due to mechanical effects.

5 The numerical calculation of coupled electromagnetic-thermal problems

5.1 Non-linear calculation algorithms

5.1.1 General problem

In this chapter, non-linear problems in several variables are discussed in general terms, for a set $\boldsymbol{G}$ of n coupled functions (mappings) G_i applied on a vector of field unknowns $\boldsymbol{x}$. When a steady-state solution is sought, the following system is to be solved:

$$\boldsymbol{G}(\boldsymbol{x}) = \left[G_i(\boldsymbol{x})\right]_{i=1(1)n} = \boldsymbol{0}\,, \tag{5.1}$$

with:

$$\boldsymbol{x} \equiv \left(x_1, x_2, ..., x_n\right) \tag{5.2}$$

or as a general transient problem:

$$\boldsymbol{G}(\boldsymbol{x}) + \frac{\mathrm{d}\boldsymbol{x}}{\mathrm{d}t} = \left[G_i(\boldsymbol{x}) + \frac{\mathrm{d}x_i}{\mathrm{d}t} \right]_{i=1(1)n} = \boldsymbol{0}\,. \tag{5.3}$$

Eq. (5.3) is usually solved using a finite difference discretisation for the time derivative. The transient problem can be considered as a special version of (5.1), with an additional linear term:

$$\begin{aligned} &\boldsymbol{G}\left(\boldsymbol{x}\left[t_{l+1}\right]\right) + \frac{\boldsymbol{x}\left[t_{l+1}\right] - \boldsymbol{x}\left[t_l\right]}{\Delta t_{l+1}} \\ &= \left[G_i\left(\boldsymbol{x}\left[t_{l+1}\right]\right) + \frac{x_i\left[t_{l+1}\right] - x_i\left[t_l\right]}{\Delta t_{l+1}} \right]_{i=1(1)n} = \boldsymbol{0} \end{aligned}\,. \tag{5.4}$$

In general, a transient problem contains an extra outer time-loop setting up a sequence of non-linear problems (5.4).

The exact solution $\boldsymbol{x}^*$ of (5.1) or (5.3) is approximated $\boldsymbol{x}$, which contains an error $\boldsymbol{\varepsilon}$,

$$\boldsymbol{x}^* = \boldsymbol{x} + \boldsymbol{\varepsilon} = \left[x_i + \varepsilon_i\right]_{i=1(1)n}\,. \tag{5.5}$$

It must be noted that non-linear problems, such as coupled electromagnetic-thermal problems, not necessarily have a unique solution. Therefore, algorithms may converge to non-physically viable, numerical solutions.

5.1.2 Non-linear problem solution methods

Since it is very troublesome and doubtful to transform realistic non-linear equations into ‘easier-to-solve’ linear equations by means of a variable transformation, numerical iterative methods are required. Two of the commonly used methods are discussed here for the general coupled physical field problems of section 2.1.

5.1.2.1 Picard iterations

The Picard iterative method, also known as fixed point iteration, is based on the consecutive application of a non-linear function of the previously obtained solution vector until a fixed point is reached:

$$\boldsymbol{x} = \boldsymbol{G}^*(\boldsymbol{x}). \tag{5.6}$$

A candidate for this function could be:

$$\boldsymbol{G}^*(\boldsymbol{x}) = \boldsymbol{x} - \boldsymbol{A}^{-1}\boldsymbol{G}(\boldsymbol{x}), \tag{5.7}$$

with $\boldsymbol{A}$ an non-singular matrix, representing the linear system solution, forming an iterative loop by itself. Convergence is assured when the function ‘contracts’ around the fixed point, which is numerically translated as [ORTE]:

$$\rho\left(\frac{\partial \boldsymbol{G}^*}{\partial x}\right) = \rho\left(\boldsymbol{I} - \boldsymbol{A}^{-1}\frac{\partial \boldsymbol{G}}{\partial x}(\boldsymbol{x}^*)\right) < 1, \tag{5.8}$$

with ρ the spectral radius (largest absolute eigenvalue). The convergence rate is higher when this spectral radius is closer to zero. The yet undetermined matrix can be used to influence the convergence behaviour. Figure 5.1 shows a graphical interpretation of the single-function contraction. The typical 'jumpy' convergence is illustrated.

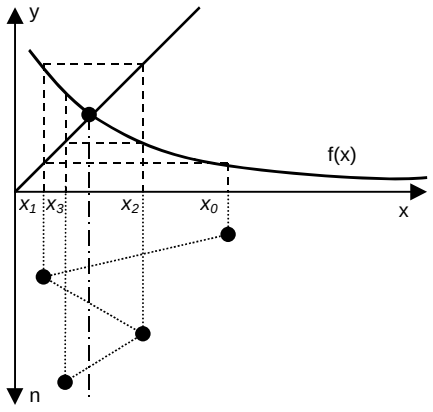

Figure 5.1 Graphical interpretation of the Picard substitution method

It is not necessary to treat the entire set of coupled functions G_i as a unit. The considered matrix $\boldsymbol{A}$ can be written in block form, with blocks having the size of the related subfield variable vectors. This results in the practical implementations of

this method for coupled fields: the block Jacobi en block Gauss-Seidel method [ORTE]. In the Jacobi approach, the function evaluations are calculated independently and can therefore be parallelised:

$$x_i^{(k+1)} = x_i^{(k)} - \zeta_i^{(k+1)} G_i\left(...,x_{i-1}^{(k)},x_i^{(k)},x_{i+1}^{(k)},...\right),\ i=1(1)n\,. \tag{5.9}$$

In the Gauss-Seidel approach, the newly obtained subfield solutions are immediately used in the next evaluations. As a consequence, this method requires sequential calculations:

$$x_i^{(k+1)} = x_i^{(k)} - \zeta_i^{(k+1)} G_i\left(...,x_{i-1}^{(k+1)},x_i^{(k)},x_{i+1}^{(k)},...\right),\ i=1(1)n\,. \tag{5.10}$$

The parameter ζ_i is a relaxation parameter, or represents a set of relaxation parameters, introduced to enhance the global convergence (section 5.1.3.1).

5.1.2.2 Newton methods

Newton methods are based on local Taylor approximations of the non-linear function in $\boldsymbol{x}$, an approximation to $\boldsymbol{x}^*$:

$$\boldsymbol{G}\left(\boldsymbol{x}^*\right) = \boldsymbol{G}\left(\boldsymbol{x}\right) + \boldsymbol{J}\left(\boldsymbol{x}\right)\left(\boldsymbol{x}^* - \boldsymbol{x}\right) + ... = \boldsymbol{0}\,, \tag{5.11}$$

with the Jacobian matrix $\boldsymbol{J}$:

$$\boldsymbol{J}\left(\boldsymbol{x}\right) = \frac{\partial \boldsymbol{G}}{\partial x}\left(\boldsymbol{x}\right) = \left[\frac{\partial G_i}{\partial x_j}\left(\boldsymbol{x}\right)\right]_{i=1(1)n}\,. \tag{5.12}$$

Defining the correction vector $\boldsymbol{\delta}$:

$$\boldsymbol{\delta} = \boldsymbol{x}^* - \boldsymbol{x}\,, \tag{5.13}$$

yielding the linearised system to be solved in the Newton-Raphson method:

$$\boldsymbol{J}\left(\boldsymbol{x}\right)\boldsymbol{\delta} = -\boldsymbol{G}\left(\boldsymbol{x}\right). \tag{5.14}$$

This system is solved iteratively:

$$\boldsymbol{J}\left(\boldsymbol{x}^{(k)}\right)\boldsymbol{\delta}^{(k+1)} = -\boldsymbol{G}\left(\boldsymbol{x}^{(k)}\right). \tag{5.15}$$

To ensure global convergence, a relaxation parameter is required as well:

$$\boldsymbol{x}^{(k+1)} = \boldsymbol{x}^{(k)} + \boldsymbol{\zeta}^{(k+1)} \boldsymbol{J}\left(\boldsymbol{x}^{(k)}\right)^{-1} \boldsymbol{G}\left(\boldsymbol{x}^{(k)}\right). \tag{5.16}$$

In fact, the Jacobian occupies the place of the matrix $\boldsymbol{A}$ in (5.7). Close to the exact solution, the spectral radius (5.8) becomes almost zero, yielding an optimal (quadratic) *local* convergence behaviour.

Hence, the cost of Newton methods is obviously two-fold:

1. computation of the (approximate) Jacobian (5.12), requiring all the partial derivatives.
2. resolution of the correction equation using the inversion of the Jacobian in (5.16).

These cost considerations lead to various approximate methods.

5.1.2.3 Approximate quasi-Newton methods

Since the computation of the Jacobian (5.12) can be a complicated procedure, as will be demonstrated further on, and since the elements often cannot be obtained by means of analytic differentiation, numerical approximations to $\boldsymbol{J}$ exist (indicated as $\tilde{\boldsymbol{J}}$).

A first approximation consists of calculating the derivative entries using differences. This generally requires a function evaluation per entry, plus one evaluation common to all entries. For large systems, it soon becomes a prohibitively computationally time-consuming manipulation. Another way is to calculate the Jacobian exactly and keep it constant for a few calculations. An alternative is to use a direct Jacobian matrix approximation, the Broyden method [PRES], which can be interpreted as a multi-dimensional extension of the secant method. This secant method locally uses a chord instead of a tangential approximation to non-linear functions. In these methods, an iterative approximation of J is built by matrix-vector operations. However, it is not guaranteed that it has the same sparse fill-in pattern as the exact matrix.

A totally different approach is not to approximate $\boldsymbol{J}$ itself, but the operations in which it features. More in particular, the matrix-vector product with a relatively small vector can be approximated by:

$$\boldsymbol{J}(\boldsymbol{x})\boldsymbol{v} = \left[\frac{\partial G_i}{\partial x}(\boldsymbol{x})v_i\right]_{i=1(1)n} \approx \left[\frac{G_i(\boldsymbol{x}+\kappa_i\boldsymbol{v})-G_i(\boldsymbol{x})}{\kappa_i}\right]_{i=1(1)n} \tag{5.17}$$

These matrix-vector products are performed when solving (5.14) by means of an iterative linear system solver such as GMRES and TFQMR (Generalised Minimal Residual method and Transpose-Free Quasi-Minimum Residual: see section 5.2) [BRO1] [BRO2]. Higher order differences can be defined as well, but require more calculations.
Calculating (5.17) for coupled problems, in which the matrix $\boldsymbol{J}$ can be arranged in blocks, is a relatively cheap manipulation. Normally, the right term is known already, since it is found in the right-hand side of the matrix equation. When the block structure is exploited, the required independent product functions can be calculated in parallel.

5.1.3 Common aspects

5.1.3.1 Relaxation for global convergence

The solution algorithms presented here all show excellent convergence behaviour when close to the solution, but to get in the vicinity of the solution is often a major problem. The global convergence requirement calls for additional measures in the calculation process. The in (5.9)-(5.10) or (5.16) calculated corrections to the previous solutions may not be going into the right direction or may be too large and pass the desired solution.

To ensure an evolution in the desired direction, an extra line search along the calculated direction indicated by the obtained correction vector, is introduced. This leads to a value for the relaxation parameter(s) ζ_i, usually limited to the interval]0,1]. The parameter should be chosen in such a way, that the value of the residual is decreasing [NEAG], [O'DWY]:

$$\left\| G_i\left(\boldsymbol{x}^{(k+1)}\right)\right\| < \left\| G_i\left(\boldsymbol{x}^{(k)}\right)\right\| . \tag{5.18}$$

For Newton methods, extra conditions can be defined to fulfil (5.18), requiring additional tests involving gradients to be computed (Goldstein and Armijo conditions, [DENN]). These tests are derived from imposing descent directions for the residual vector and limits on the angles between the correction and residual vector [KOSM].

5.1.3.2 Stopping criteria

To detect convergence, the residual or the difference between two consecutive solutions can be used as a measure. It is possible to use a dominating subproblem as in (5.19), or the entire solution vector (5.20). The latter is only advisable when the unknowns are sufficiently scaled to be comparable. A combination of subproblem criteria (5.19) is a good alternative when no scaling is available.

$$\left\| x_i^{(k+1)} - x_i^{(k)} \right\| < \varepsilon^{(k+1)} \text{ or } \left\| \delta_i^{(k+1)} \right\| < \varepsilon^{(k+1)} \tag{5.19}$$

$$\left\| \boldsymbol{x}^{(k+1)} - \boldsymbol{x}^{(k)} \right\| < \varepsilon^{(k+1)} \text{ or } \left\| \boldsymbol{\delta}^{(k+1)} \right\| < \varepsilon^{(k+1)} \tag{5.20}$$

The norms to be used in (5.19) and (5.20) can be the 1-, 2- or the ∞-norm. The latter stresses extreme values the most. It is used in most calculations further on.
To construct relative norms, a representative vector in the same vector space has to be used. The residual (the right-hand side in the Newton methods) is a candidate for this approach. However, when far away from the solution, local, non-global, minima may let this approach fail. In practice, the non-linear solution vector itself proves to be a good alternative as well, though it is mathematically not ideal since it is not located in the same vector space.

To combine the different subproblem residuals, a weighted sum is be constructed to build a generalised residual:

$$R = \sum_i w_i G_i\left(\boldsymbol{x}\right) \tag{5.21}$$

The error bound $\varepsilon^{(k+1)}$ should not be a constant throughout the entire computation. In the beginning of the iterative solution process, it is only of importance to find a good search direction. Therefore, the error-bound can be chosen larger in the beginning, to obtain a result that is 'just good enough' and gradually decrease it when near to the solution. However, it is difficult to know the appropriate parameter and often semi-heuristic rules are used (e.g. check the evolution of the residual). These methodologies are known under the name 'inexact' Newton methods [FOKK]. In practice, often the parameter is kept constant, for reasons of robustness, at a larger computational expense.

5.1.3.3 Starting solutions

The convergence at non-linear level is enhanced significantly when a good starting solution vector is available [JÄNI]. Several options exist:

- *Continuation*: A determining (coupling) parameter can be altered step by step to end up with the problem to be solved. For coupled problems this can be interpreted as making the coupling 'stronger'.
- *Nested iterations*: The problem can be solved for coarser discretisations. This solution is projected onto the next level, a finer mesh. This approach is related to the multigrid method for non-linear problems [BRIG]. On the coarse grid, the 'lowest spatial frequencies' are resolved in a relatively inexpensive way, followed by a projection, to calculate correction for the highest frequencies on the fine mesh. However, the coarse mesh must be sufficiently fine to obtain a good starting solution.
- *Solution from a previous time step*: When the time steps in a transient or pseudo-transient problem are well chosen, the previous solution is an excellent starting point. A trade-off has to be made between the time step, influencing the total number of non-linear problems and the non-linear convergence behaviour.

5.1.4 Solution procedures for coupled magnetic-thermal problems

The electromagnetic-thermal problem in general consists of two finite element systems and two coupling functions (losses and thermal dependency of the material parameters). Theoretically, it is possible to eliminate the coupling functions and the related variables, but in practice it is not always advantageous, when complicated calculation models are applicable. It is also assumed that the solution of one field is available on the mesh of the other field by means of projection (indicated by a ´). The two-field coupled problem is written as:

$$\begin{cases} G_A\left(A, T'\right) = 0 \\ G_T\left(A', T\right) = 0 \end{cases}. \tag{5.22}$$

The function G_A represents a magnetic formulation in static (3.37), time-harmonic (3.48), multi-harmonic **Error! Reference source not found.**, transient time-harmonic **Error! Reference source not found.** or general transient form (3.40). The function G_T represents a thermal problem in static or transient form (3.61).

Decoupled multi-harmonic algorithms are in principle solved using the same methodologies. Their coupling mechanism is the harmonic series updating procedure. In this case (5.22) becomes:

$$\begin{cases} G_{A_1}\left(A_1, \ldots, A_N', T'\right) = 0 \\ \qquad \vdots \\ G_{A_N}\left(A_1', \ldots, A_N, T'\right) = 0 \\ \\ \left[G_T\left(A', T\right) = 0\right] \end{cases} \tag{5.23}$$

In the methods discussed in the following paragraphs, the magnetic problem is treated as a whole, for reason of simplicity.

5.1.4.1 Steady-state problems: Picard methods

The block Jacobi iteration algorithm to solve (5.22) is plotted symbolically in Algorithm 5.1:

1	calculate initial $A^{(0)}$ (e.g. assume $T^{(0)}=T_{ambient}$)	calculate initial $T^{(0)}$ (e.g. assume $A^{(0)}=0$)
2	**while not converged & k<k_{max}**	
3	calculate $T'^{(k)}$	calculate $A'^{(k)}$
4	update material parameters	calculate losses
5	solve $A^{(k+½)}$ from $G_A(A^{(k+½)},T'^{(k)})=0$	solve $T^{(k+½)}$ from $G_T(A'^{(k)},T^{(k+½)})=0$
6	calculate relaxation parameters $\zeta_A^{(k+1)}$ and $\zeta_T^{(k+1)}$	
7	$A^{(k+1)}=A^{(k)}+\zeta_A^{(k+1)}(A^{(k+½)}-A^{(k)})$	$T^{(k+1)}=T^{(k)}+\zeta_T^{(k+1)}(T^{(k+½)}-T^{(k)})$
8	calculate convergence criterion (residuals)	
9	k=k+1	
10	**go to step 2**	
11	**end**	

Algorithm 5.1 Block Jacobi algorithm

The individual field solutions in step 5 are non-linear problems on their own, considering the problem-own non-linearities such as magnetic saturation. The same methods as discussed in section 5.1.2 are applicable on a smaller scale. It is possible to combine (simpler) Newton methods on this level with the less complicated substitution algorithm on the block level. However, the subproblem convergence is usually not so troublesome, since a good starting solution is available, namely the previous iteration solution. For some problem-own non-linearities that prove to be not very sensitive to the coupling variables, it is possible to calculate them in step 1 and 'freeze' them for the calculations in steps 4 and 5. This often yields linear problems in step 5 (e.g. a fixed saturation yields a linear magnetic problem).

The parallelism in steps 1, 3-5 and 7 can be exploited to minimise the calculation time. In principle, the information to be exchanged between the parallel branches consists of two partial solution vectors, containing the relevant information (e.g. only the solution associated to elements containing coupled non-linearities). These vectors may become very large, so a fast communication channel is required. In this respect, a parallel implementation is advisable on a multi-processor machine, over single-processor machines in a network.
The convergence of this algorithm is rather slow, but relatively stable. Severe oscillations may occur when relaxation is omitted.

The block *Gauss-Seidel* iteration algorithm to solve (5.22) is plotted symbolically in Algorithm 5.2:

1	calculate initial $A^{(0)}$ (e.g. assume $T^{(0)}=T_{ambient}$)	calculate initial $T^{(0)}$ (e.g. assume $A^{(0)}=0$)
2	**while not converged & k<k$_{max}$**	
3	calculate $T'^{(k)}$	
4	update material parameters	
5	solve $A^{(k+½)}$ from $G_A(A^{(k+½)},T'^{(k)})=0$	
6	calculate relaxation parameter $\zeta_A^{(k+1)}$	
7	$A^{(k+1)}=A^{(k)}+\zeta_A^{(k+1)}(A^{(k+½)}-A^{(k)})$	
3	calculate $A'^{(k+1)}$	
4	calculate losses	
5	solve $T^{(k+½)}$ from $G_T(A'^{(k+1)},T^{(k+½)})=0$	
6	calculate relaxation parameters $\zeta_T^{(k+1)}$	
7	$T^{(k+1)}=T^{(k)}+\zeta_T^{(k+1)}(T^{(k+½)}-T^{(k)})$	
8	calculate convergence criterion (residuals)	
9	k=k+1	
10	**go to step 2**	
11	**End**	

Algorithm 5.2 Block Gauss-Seidel algorithm

This algorithm is essentially sequential and therefore, cannot benefit from the time saving parallel calculations. However, the convergence is generally faster than its block Jacobi variant. This convergence rate is obtained due to the direct use of the partial magnetic solution to calculate the next thermal solution. In numerical experiments, the gain is about a factor of two.
In theory, the magnetic and the thermal block could be interchanged, but this yields an initial slower convergence in practice (it is more logical to start with a loss calculation).

5.1.4.2 Steady-state problems: Newton-Raphson method

The steady-state Newton-Raphson method requires the calculation of the Jacobian of (5.22). The correction equation becomes:

$$\begin{bmatrix} \dfrac{\partial G_A}{\partial A} & \dfrac{\partial G_A}{\partial T'}\dfrac{\partial T'}{\partial T} \\ \dfrac{\partial G_T}{\partial A'}\dfrac{\partial A'}{\partial A} & \dfrac{\partial G_T}{\partial T} \end{bmatrix} \begin{bmatrix} \delta_A \\ \delta_T \end{bmatrix} = -\begin{bmatrix} G_A \\ G_T \end{bmatrix}, \tag{5.24}$$

with a non-symmetric Jacobian matrix, though the diagonal blocks may be symmetric.

The derivatives of the magnetic function to the temperature are calculated using the temperature dependencies. These are calculated by differentiating the appropriate material characteristic expressions in section 4.1. When analytical functions are available, it is possible to construct analytical expressions. In the case data samples are provided, the use of a smooth interpolating function is required, e.g. bicubic splines [KREY]. The smoothness is important to avoid oscillations in the derivative. The derivative of the saturation is modelled by a spline interpolation as well [SILV]. In this method the distinction between problem-own and coupled non-linearities has disappeared.

The off-diagonal derivative of the thermal function reflects the variation of the losses with respect to the magnetic variables. The calculation of this expression can become very complicated. For instance, the procedure required to calculate the iron loss, which is a function of the core's temperature, may involve a set of separate computations and therefore, is not easily differentiable. Approximations are necessary having inherently an influence on the quadratic rate of convergence.
The problem-own derivative is due to temperature dependent thermal material parameters in the equation (e.g. a changing thermal conductivity) and the loss expressions (e.g. the electrical conductivity in the Joule loss). These are calculated using the same techniques as for the magnetic subproblem.

Often additional derivatives can occur when circuit equations are present in the magnetic or thermal system.

The extra derivative factors in the off-diagonal terms arise due to the use of independent meshes. They are calculated using the polynomial projection equations (section **Error! Reference source not found.**). Obviously, these factors equal one when identical meshes are used in the overlapping sections. When the interpolating projection method is used, every degree of freedom is expressed as a weighted sum of a limited number of MDOFs in the other mesh (e.g. **Error! Reference source not found.**). The derivatives consisting of these weights will cause additional entries in the off-diagonal blocks for every MDOF in the other mesh (min. three for each MDOF in first order triangular elements). Figure 5.2 illustrates how the three MDOFs of one element of the first mesh are connected to 6 MDOFs in the second mesh.

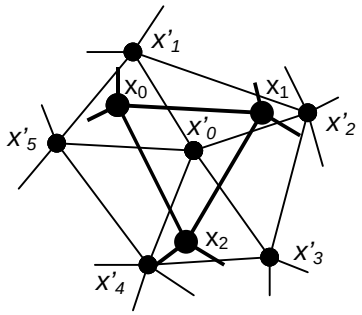

Figure 5.2 Related MDOFs for first order triangular elements in coupled meshes

The use of the weighted residual method requires a non-trivial inversion of the matrix equation **Error! Reference source not found.**. Actually, it is required to include these matrix systems explicitly instead of implicitly (indicated as $P_{AA'}$ and $P_{TT'}$), as extra blocks in (5.24):

$$\begin{bmatrix} \frac{\partial G_A}{\partial A} & 0 & \frac{\partial G_A}{\partial T'} & 0 \\ \frac{\partial P_{AA'}}{\partial A} & \frac{\partial P_{AA'}}{\partial A'} & 0 & 0 \\ 0 & 0 & \frac{\partial P_{TTA}}{\partial T'} & \frac{\partial P_{TT'}}{\partial T} \\ 0 & \frac{\partial G_T}{\partial A'} & 0 & \frac{\partial G_T}{\partial T} \end{bmatrix} \begin{bmatrix} \delta_A \\ \delta_{A'} \\ \delta_{T'} \\ \delta_T \end{bmatrix} = -\begin{bmatrix} G_A \\ G_{A'} \\ G_{T'} \\ G_T \end{bmatrix}. \tag{5.25}$$

The Jacobian construction has an extra difficulty when the magnetic field is calculated in the frequency domain. To be differentiable, the complex function has to fulfil the Cauchy-Riemann conditions. In general, this is not the case [LED2]:

$$\frac{\partial \operatorname{Re}\{G_A\}}{\partial \operatorname{Re}\{A\}} \neq \frac{\partial \operatorname{Im}\{G_A\}}{\partial \operatorname{Im}\{A\}} \;\&\; \frac{\partial \operatorname{Re}\{G_A\}}{\partial \operatorname{Im}\{A\}} \neq -\frac{\partial \operatorname{Im}\{G_A\}}{\partial \operatorname{Re}\{A\}}. \tag{5.26}$$

Then, G_A has to be split up in a real and an imaginary function. This seems to make the matrix larger, but the reduction of a complex MDOF, having two parts, to two separate MDOFs does not change the computational effort in practice. The symmetry within the magnetic diagonal block may be lost. Equation (5.24) becomes:

$$\begin{bmatrix} \frac{\partial \operatorname{Re}\{G_A\}}{\partial \operatorname{Re}\{A\}} & \frac{\partial \operatorname{Re}\{G_A\}}{\partial \operatorname{Im}\{A\}} & \frac{\partial \operatorname{Re}\{G_A\}}{\partial T'}\frac{\partial T'}{\partial T} \\ \frac{\partial \operatorname{Im}\{G_A\}}{\partial \operatorname{Re}\{A\}} & \frac{\partial \operatorname{Im}\{G_A\}}{\partial \operatorname{Im}\{A\}} & \frac{\partial \operatorname{Im}\{G_A\}}{\partial T'}\frac{\partial T'}{\partial T} \\ \frac{\partial G_T}{\partial \operatorname{Re}\{A'\}}\frac{\partial \operatorname{Re}\{A'\}}{\partial \operatorname{Re}\{A\}} & \frac{\partial G_T}{\partial \operatorname{Im}\{A'\}}\frac{\partial \operatorname{Im}\{A'\}}{\partial \operatorname{Im}\{A\}} & \frac{\partial G_T}{\partial T} \end{bmatrix} \begin{bmatrix} \operatorname{Re}\{\delta_A\} \\ \operatorname{Im}\{\delta_A\} \\ \delta_T \end{bmatrix} = -\begin{bmatrix} \operatorname{Re}\{G_A\} \\ \operatorname{Im}\{G_A\} \\ G_T \end{bmatrix} \tag{5.27}$$

The magnetic subfield projection derivatives, being geometrical functions, remain unchanged, whether they refer to the real or imaginary part:

$$\frac{\partial A'}{\partial A} = \frac{\partial \operatorname{Re}\{A'\}}{\partial \operatorname{Re}\{A\}} = \frac{\partial \operatorname{Im}\{A'\}}{\partial \operatorname{Im}\{A\}}. \tag{5.28}$$

To obtain a good starting solution, required for fast convergence of this method, some less expensive Picard-type iteration steps may be executed in the beginning of the overall iteration. The ‘cascade’ algorithm becomes:

1	calculate initial $A^{(0)}$ (e.g. assume $T^{(0)}=T_{ambient}$)	calculate initial $T^{(0)}$ (e.g. assume $A^{(0)}=0$)
2	**while not converged & k<k$_{max}$**	
3	calculate Jacobian (residuals stored previously)	
4	solve correction equation (approximately)	
5	calculate relaxation parameters $\zeta_A^{(k+1)}$ and $\zeta_T^{(k+1)}$	
6	$A^{(k+1)}=A^{(k)}+\zeta_A^{(k+1)}\delta_A^{(k+1)}$	$T^{(k+1)}=T^{(k)}+\zeta_T^{(k+1)}\delta_T^{(k+1)}$
7	calculate convergence criterion (residuals)	
8	k=k+1	
9	**go to step 2**	
10	**end**	

Algorithm 5.3 Newton algorithm

Theoretically, the inner linear loop and outer non-linear loop, both solved iteratively, could be interchanged [ORTE], but this yields increasing computation times for coupled problems, due to the increased number of Jacobians to be computed.

Here, it must be noted that the solution of the correction equation in step 4 is not easy. The reason for this is that the numerical properties of the asymmetric Jacobian matrix are not very favourable and a large condition number is obtained. In experiments on realistic problems, numbers ranging from 10^{10} to 10^{20}, even after scaling and reordering, were obtained. To solve such asymmetric systems, memory consuming iterative solvers, such as the GMRES algorithm, are required. As a consequence of these large condition numbers, only few digits of the solution can be considered accurate.

The explanation for this large difference is partially due to the large magnitude differences of the matrix coefficients, even after the scaling, caused by the magnitude difference of the underlying physical phenomenon parameters, such as the large electrical conductivities.

The most favourable matrix arrangement is found, when coefficients of associated MDOFs are put together in the Jacobian, yielding loss of the block structure, but leading to an increased diagonal dominance. This is easy to accomplish for identical meshes, but not when projections are involved.

In the literature only a limited amount of true ‘strong coupled’ systems are solved with Newton methods. As far as known to the author, the method has only been successful in the simulation of simplified fusion reactor systems (plasma) [MOL1], [MOL2] on an identical, relatively small, mesh. In this case, the material coefficients magnitudes seem to have values leading to a smaller condition number.

In other types of coupled problems, more in particular couplings with mechanical equations, this ‘full-coupled approach’ seems to be more common [KALT], [REN], [ALUR], though some can be reduced to a decoupling [GROS], [FELI]. Numerical problems are reported in MEMS structures [WHIT]. Again, this is explained by an apparently more favourable parameter set. The partial derivatives are determined by elastic displacements and force computations. Also the smaller amount of variables active in the coupling (non-zero off-diagonal elements) is an advantage. For

instance, in the force computation only the local field on a boundary matters, unlike entire regions for loss calculations.

5.1.4.3 (Pseudo-)Transient problems

In the calculation of coupled transient thermal-magnetic systems, a major problem may occur when the time constants of the dynamic phenomena in the magnetic problem significantly differ from the time constants in the thermal problem. Although the time constants are not known in advance, this difference is present as soon as non-*DC* sources are used. In that case, the coupled problem has a stiff nature (section **Error! Reference source not found.**).
Several approaches can be chosen:

- *Simulate at the time step of the magnetic problem*: This is required when the standard transient magnetic equation (3.40) is combined with the transient thermal equation (3.61), possibly in a full-coupled system. This is not an advantage, since the thermal variables will hardly change in the short time span.

- *Simulate at the time step of the thermal problem*: The system to be solved is extremely stiff in practice and requires special transient methods, e.g. BDF methods. These time stepping methods can be interpreted as an averaging of the fast phenomena yielding the underlying slow variation. For practical problems, this approach is stable, but yields less accurate solutions.

- *Simulate using two time scales*: An extension of the previous method is to keep the slowly varying thermal variables constant during a number of magnetic time steps. The magnetic time marching is stopped when a (local) steady state is obtained. It is even possible to use different time integration methods for the subproblem (for a discussion in the field of mechanical coupled problems, see [LIUW], [WOOD]). This method is not ideal either, since the knowledge of the magnetic solution 'now and then' to determine the thermal solution may introduce erroneous extrapolations. For very non-linear magnetic problems, demanding a (too) large harmonics series, this is the best possible approach (for a highly saturated induction heat example, see [CHAB]). Obviously, this approach is only possible after decoupling the equations.

- *Assume the fast method is 'in a continuously changing steady state'*: This approach is the most used. The slow thermally initiated, dynamics in the fast changing problem are neglected. The calculated steady state is updated at the pace of the thermal problem. Mathematically, this means that a steady-state frequency domain method with one or more harmonics is combined with a transient thermal method. The loss values calculated for this 'local steady state' are assumed to remain constant over each time interval. The systematic error introduced this way, by *over*estimating the losses, may make the problem unstable, even for very small time steps. However, for problems with limited interaction, an acceptable approximation is found. In the literature, many coupled problems are presented this way and solved using a cascade algorithm (e.g. actuators: [XYPT]; induction heating: [CHAB]; MEMS: [WHIT]).

- *The envelope approach*: A reformulation of the fast changing magnetic problem to separate slow and fast dynamic effects yields a far more stable and correct solution. In this approach, the transient time harmonic method, modelling the amplitude and phase change at the pace of the thermal dynamics, (sections 2.1.2 and **Error! Reference source not found.**) is combined with the transient thermal equation, the time step being identical for both. The losses are not extrapolated, but interpolated. This method reduces to the previous one if for the magnetic problem, a full implicit transient method with an extremely large time step is used.

The algorithm describing the coupled (pseudo-)transient solution methodology using a single time step is given below. It is assumed that the goal of the calculation is to end up at steady state. The internal non-linear problem is solved using an appropriate method as discussed before.
As mentioned, the internal non-linear problem, having a good starting solution, converges faster when compared to steady-state formulations, especially when the time step is not too large. Therefore, the internal n_{max} value is generally smaller (often equal to one). This method can be interpreted as a predictor-corrector scheme.

1	calculate initial $A[0]^{(0)}$ (e.g. assume $T[0]^{(0)}=T_{ambient}$)	calculate initial $T[0]^{(0)}$ (e.g. assume $A[0]^{(0)}=0$)
2	**while not converged & $t<t_{max}$**	
3	project initial $A[t_{l+1}]^{(0)}$ from prev. step (if not 1st)	project initial $T[t_{l+1}]^{(0)}$ from prev. step (if not 1st)
4	**while not converged & $k<k_{max}$**	
5	solve & relax non-linear coupled problem	
6	calculate convergence criterion (residuals)	
7	$k=k+1$	
8	**go to step 4**	
9	check steady-state condition	
10	$l=l+1$	
11	Estimate Δt_l	
12	$t_{l+1}=t_l+\Delta t_l$	
13	**go to step 2**	
14	**end**	

Algorithm 5.4 (Pseudo-)transient algorithm

5.1.5 Benchmark: conductive heating

5.1.5.1 Benchmark problem

In the literature, no real benchmark problem is published yet. Therefore, a simple 2D model is built, containing a simple but significant coupling, for testing different coupled algorithms.

The problem consists of a free, long, massive busbar with an applied voltage (Figure 5.3). The frequency is 50 Hz and the phase angle is 0 °. The busbar is made of copper with a temperature dependent electrical conductivity. No convergence problem causing circuit equations are present. The only losses in the model are

caused by the source and eddy currents in the conductor. It is cooled by convection at all faces. One edge is assumed to be cooled with a lower convection coefficient, introducing a moderately asymmetrical cooling. The bar's cross-section surface is equal, but the ratio of height to thickness is variable, so skin effects can change. The bar is surrounded by air at a temperature of 20 °C. For model details, see appendix **Error! Reference source not found.**.

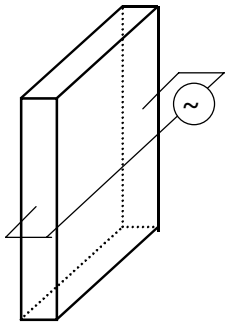

Figure 5.3 Busbar benchmark model

The non-linear coupled problem has (at least) two solutions. The first, physical, solution results in a moderate increase of the bar temperature to a hot spot temperature of about 55 °C at the edge, where the highest current density is located (Figure 5.4).

The second solution is not possible in the physical reality, as it is a result of the unconstrained extrapolation of the material characteristics involved in the coupling. Figure 5.5 shows such a result for the conductor having a height/width ratio of 40. The final temperature distribution is extremely asymmetrical with a hot spot of more than a 1000 °C, at which the material would melt. The numerical solution is stable: local minima in the residuals are obtained.
Although this solution is not physically viable with this type of material and cooling conditions, it is not to be excluded that for other materials, configurations and conditions, multiple stable states may exist in the physical reality. In that case, the object's history will determine which state eventually is reached.

Whether the solution converges to the physical or non-physical field, depends on the algorithm, its parameters and the starting point. It is possible to force an algorithm towards one of the solutions by using a starting solution obtained by means of continuation.

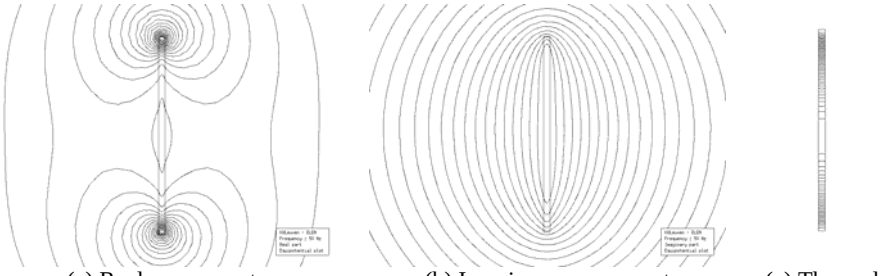

(a) Real component of magnetic solution (b) Imaginary component of magnetic solution (c) Thermal solution

Figure 5.4 'Physical' solution to the coupled busbar problem with a high aspect ratio (the hot spot temperature is 55 °C ; h/w ratio of 40)

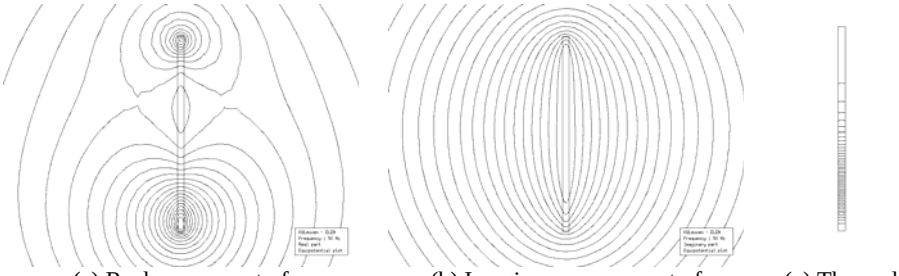

(a) Real component of magnetic solution (b) Imaginary component of magnetic solution (c) Thermal solution

Figure 5.5 'Non-physical' solution to the coupled busbar problem with a high aspect ratio (the hot spot temperature is 1220 °C ; h/w ratio of 40)

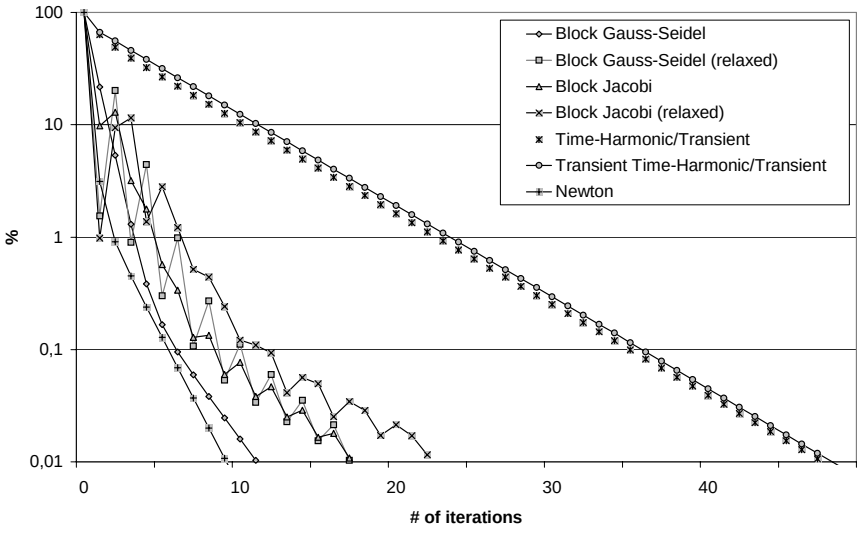

Figure 5.6 Convergence parameter evolution for the different algorithms at a size ratio h/w of 30

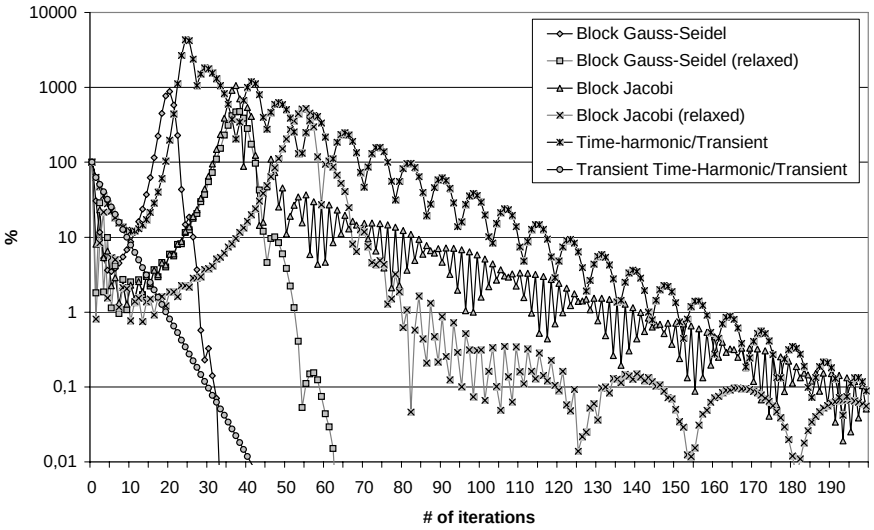

Figure 5.7 Convergence parameter evolution for the different algorithms at a size ratio h/w of 38

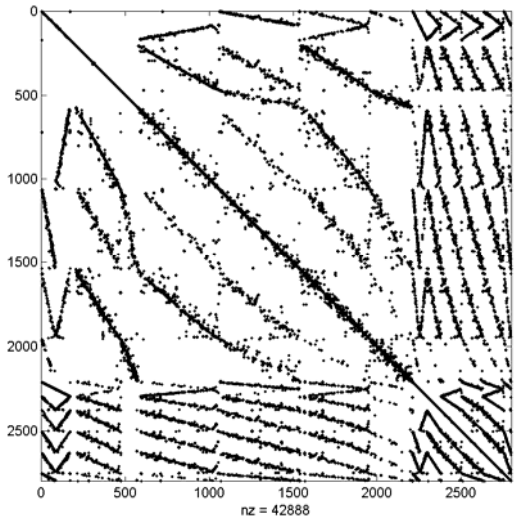

Figure 5.8 Fill-in pattern of the Jacobian matrix of the benchmark problem; the four main blocks can be distinguished

5.1.6 Example

To illustrate the use of the shell program, the coupled electromagnetic-thermal problem of a three-phase power cable is solved (Figure 5.9).

Figure 5.9 Picture and cross-section of the studied three-phase cable

Three phase power cables exist in many variations and types [HEUC], [VADO], differing in conductor shape, material choice, conductor arrangement, etc. They consist mainly of the following parts, in which several of the previously mentioned loss mechanisms are found:

- *Conductor*, usually made of copper, exhibiting Joule losses caused by the current.
- *Insulation layers and filling materials*, loaded by an alternating electric field and therefore subject to dielectric losses.
- *Grounded lead sheath* around the primary insulation, shielding the electric field; due to its (relatively low) conductance, internal eddy currents may develop.
- *Mechanical protection (armour)*, sometimes made of magnetic steel and therefore, possibly subject to hysteresis and eddy current losses.

To compute the coupled solution, three different meshes are constructed (Figure 5.10). The electric field mesh contains 9943 triangular first order elements, the magnetic 15378 and the thermal 15560. The material representing the soil in the thermal model has scaled properties; normally, the cable is buried about one meter deep in the soil. The boundary conditions of the electrical field are of the Dirichlet type. In the infinite magnetic and semi-infinite thermal domain, a domain transformation is used [DR03].

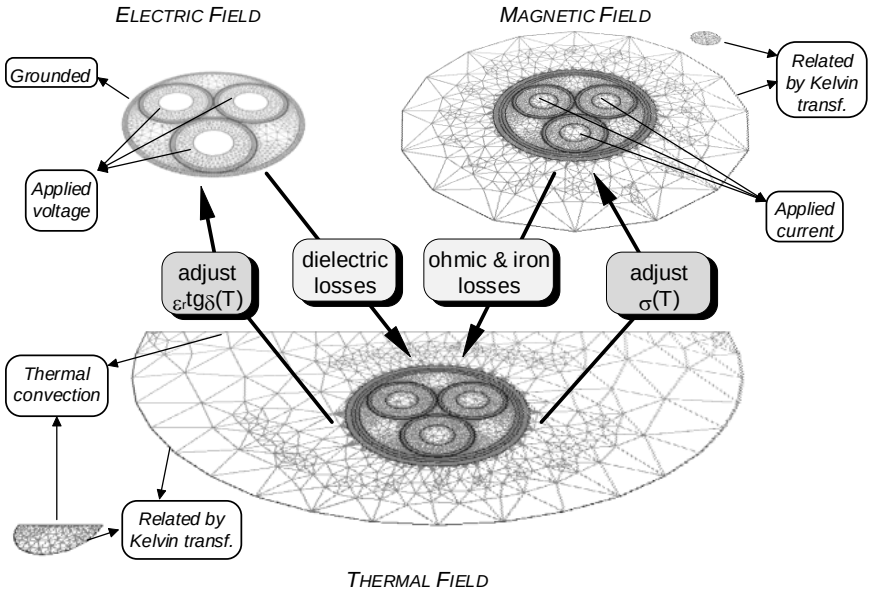

Figure 5.10 Mesh relations of the three-phase cable example

One script steers the iterative relaxed Gauss-Seidel solution. A stopping criterion is evaluated using the 2-norm of the thermal solutions. Subscripts describe the electrical and magnetic field calculation, followed by the relevant loss calculations and their projection on the thermal mesh. These two subscripts are executed with maximum efficiency in parallel (on a two-processor workstation HP J2-240), with a minimum of communication delay (no network traffic). The results are shown in Figure 5.11.

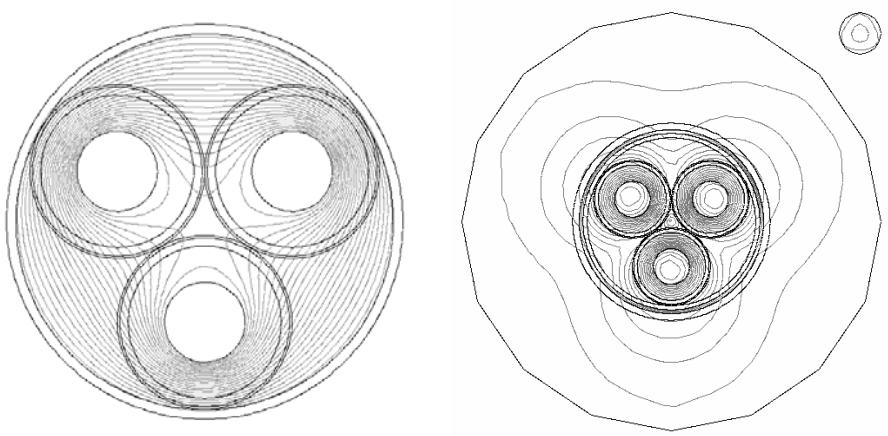

(a) Magnitude of electrical field (b) Magnitude of magnetic field

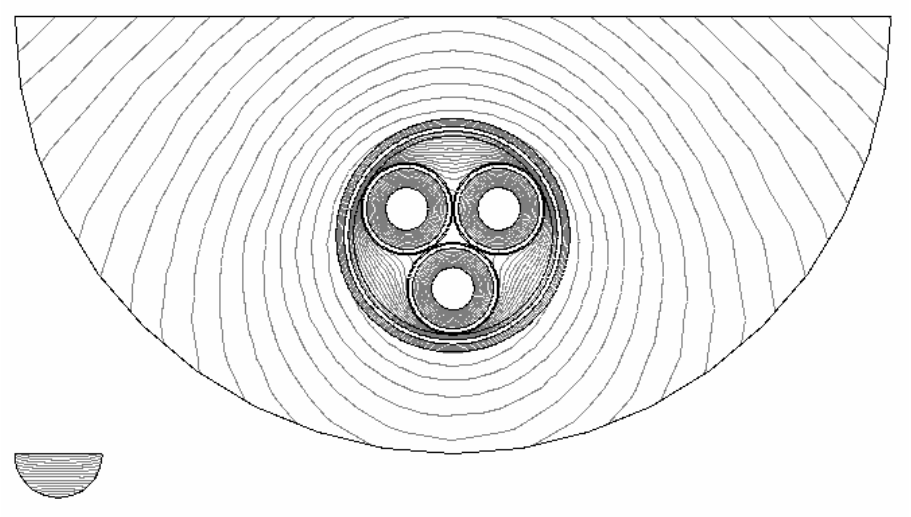

(c) Thermal field lines

Figure 5.11 Subproblem field solutions of the cable example

5.2 Linear system solution

Since this work is mostly application oriented, it was originally intended not to investigate the numerical aspects of the large-scale algebraic system solving thoroughly and consider this part of the calculation process as a 'black box'. Therefore, only a general discussion is given here. However, it is a major mistake to underestimate the influence to the numerical properties of the system to solve, as they are related to the physical properties: a system difficult to describe with physical equations, is most of the time difficult to solve numerically, which is not different for coupled problems …

5.2.1 Krylov subspace solution methods

The iterative solvers for the linear systems (5.29) belong to the family of Krylov subspace methods. These only require matrix-vector products and therefore benefit from the sparsity of the FEM equation systems without circuit equations. The solution is approximated in the Krylov subspace K of order *k*, smaller than the number of unknowns:

$$\boldsymbol{A}\boldsymbol{x} = \boldsymbol{B}\ , \tag{5.29}$$

$$\mathrm{K}^{k} = \left\{ \boldsymbol{R}_0, \boldsymbol{A}\boldsymbol{R}_0, \boldsymbol{A}^2\boldsymbol{R}_0, ..., \boldsymbol{A}^k\boldsymbol{R}_0 \right\}, \tag{5.30}$$

with $\boldsymbol{A}$ a sparse matrix and $\boldsymbol{B}$ the right-hand side vector. The subspace is based on products of powers of the system matrix with the initial solution residual $\boldsymbol{R}_0$:

$$\boldsymbol{R}_0 = \boldsymbol{B} - \boldsymbol{A}\boldsymbol{x}_0 \tag{5.31}$$

Consecutive iterates can be calculated using different approaches. The most important are [BARR], [GOLU], [DONG], [SAAD]:

- *Orthogonalise the residual with respect to the Krylov subspace*: The CG (Conjugate Gradient) method belongs to this family. It is applicable to symmetric positive definite systems [GOLU]. The memory use is limited, since short recurrences are feasible due to symmetry.

$$\boldsymbol{R}^{(k)} = \boldsymbol{B} - \boldsymbol{A}\boldsymbol{x}^{(k)} \perp \mathrm{K}^{k} \tag{5.32}$$

- *Orthogonalise the residual with respect to the an alternative subspace*: The BiCG (Bi-Orthogonal Conjugate Gradient) method uses another subspace for orthogonalisation. This method still uses recurrences and a limited amount of memory. It is suitable for non-symmetric matrices as well, but requires matrix-vector products with the transpose.
- *Minimise the norm of the residual*: The GMRES (Generalised Minimal Residual) method does not use short recurrences and has to calculate an orthogonal basis for the subspace over which a true minimisation of the residual norm is performed. Therefore this method consumes an amount of memory proportional with the number of iterations.

$$\boldsymbol{x}^{(k)} = \min_{\boldsymbol{x} \in x_0 + K^k} \left\| \boldsymbol{B} - \boldsymbol{A}\boldsymbol{x} \right\|_2 \tag{5.33}$$

  This method can be used for non-symmetric matrices as well. It is very robust, even for badly conditioned systems, but is expensive. Therefore, it is often restarted after a fixed number of iterations.
- *Quasi-minimise the norm of the residual*: The QMR (Quasi-Minimal Residual) method uses another subspace to orthogonalise and can be used for non-symmetric matrices. The residual norm is approximately minimised. In general, it has a smoother convergence than BiCG. It also has an excellent convergence behaviour for complex systems [DEG2].

The convergence behaviour of these methods is determined by the eigenvalue spectrum of the matrix $\boldsymbol{A}$. The condition number, being the ratio of the largest absolute value of the eigenvalues to the smallest is a good measure. The spatial distribution in the complex plane is of importance as well. Figure 5.12 shows the spectra of the Jacobian matrices obtained from the strong coupled benchmark problem. Both the version with the symmetrised magnetic block, but with negative elements on the diagonal, and the asymmetric block version are shown. These systems have a condition number of 10^8-10^9 (after scaling) and are solved using GMRES. The magnetic block symmetrisation may lead to a less complicated spectrum, but with significant positive and negative parts. In the asymmetric version, more complex eigenvalues are present. This high condition number is explained by the large differences in underlying physical parameters.

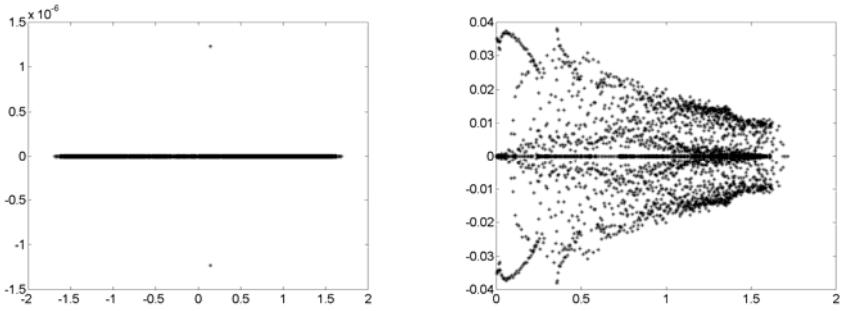

symmetric magnetic block asymmetric magnetic block

Figure 5.12 Eigenvalue spectrum of the Jacobian in the correction equation of the strong coupled benchmark problem

A totally different approach is taken in domain decomposition (DD) [SMIT] and multigrid (MG) methods [BRIG].

In DD methods the computational domain is split into different, possibly overlapping parts jointly solved with appropriate interfacing. Block elimination schemes, in which the matrix is decomposed followed by iterations on the obtained non-overlapping blocks can be considered simple DD methods. Good results can be obtained using this approach, since the numerical properties of the individual blocks are determined by the individual subproblem and therefore are usually more favourable. For instance, the diagonal magnetic and thermal blocks in the benchmark problem have condition numbers in the range of 10^3-10^4, being 6 orders lower than the global condition number.

In MG methods, nested grids are used to smooth out errors having different spatial frequencies. Recent advances in numerical research [MER1] show that they are very promising solvers and preconditioners.

5.2.2 Preconditioning

To enhance the convergence of the iterative method, it is often more interesting to solve a (left) preconditioned system:

$$\boldsymbol{M}^{-1}\boldsymbol{A}\boldsymbol{x} = \boldsymbol{M}^{-1}\boldsymbol{B} \tag{5.34}$$

The preconditioner $\boldsymbol{M}$ can be a constant matrix (stationary preconditioning) or may depend on iteration parameters (non-stationary). It may represent the limited application of another iterative method such as SSOR (Successive Symmetric Over-Relaxation) in an inner loop. Another possibility is to calculate an approximation to the inverse of the system matrix, having an easy to compute inverse. For systems with an obvious block structure, it may be interesting to organise the preconditioning in blocks as well [AARD].

It is important that the preconditioner is effective and efficient: it has to decrease the number of required iterations, but the increased computational effort per step may not cause an increase in total computation time.

References

[AARD] J.M.C. Aarden, K.E. Karlsson, *Preconditioned CG-type Methods for Solving the Coupled System of Fundamental Semiconductor Equations*, report 8924, Univ. of Nijmegen, Dept. of Mathematics, 1989.

[ALBA] G. Albanese, G. Rubinacci, "Numerical procedures for the solution of nonlinear electromagnetic problems," *IEEE Trans. on Magnetics*, vol. 28, 1992, pp. 1228-1231.

[ALUR] N. Aluru, J. White, "Algorithms for Coupled Domain MEMS Simulation," *Proc. Design Automation Conference '97*, 9-13 June 1997, Anaheim, California, USA, pp. 686-690.

[ANSY] *ANSYS user manuals*, Ansys Inc.

[ANUS] J. Anuszczyk, Z. Gmyrek, "Calculation of Field Distribution and Rotational Power Loss in Three Phase Induction Motor," *Proc. 8th Int. IGTE Symposium on Numerical Field Calculation in Electrical Engineering '98*, 21-24 September 1998, Graz, Austria, pp. 495-498.

[ARKK] A. Arkkio, A. Niemenmaa, "Estimation of Losses in Cage Induction Motors using Finite Element Techniques," *Proc. Int. Conf. On Electrical Machines (ICEM) '92*, 15-17 September 1992, Manchester, UK, pp. 317-321.

[ARM1] A.F. Armor, M.V.K. Chari, "Heat Flow in the Stator Core of Large Turbine-Generators, by the Method of Three-Dimensional Finite Elements (Part I: Analysis by Scalar Potential Formulation)," *IEEE Trans. on Power Apparatus and Systems*, vol. PAS-95, no. 5, 1976, pp. 1648-1656.

[ARM2] A.F. Armor, M.V.K. Chari, "Heat Flow in the Stator Core of Large Turbine-Generators, by the Method of Three-Dimensional Finite Elements (Part II: Temperature Distribution in the Stator Iron)," *IEEE Trans. on Power Apparatus and Systems*, vol. PAS-95, no. 5, 1976, pp. 1657-1668.

[ATAL] K. Atallah, D. Howe, P.H. Mellor, D.A. Stone, "Rotor Loss in Permanent Magnet Brushless AC Machines," *Proc. IEEE International Electric Machines and Drives Conference 1999 (IEMDC'99)*, 9-12 May 1999, Seattle, Washington, USA, pp. 60-62.

[BALL] K.S. Ball, B. Farouk, V.C. Dixit, "An experimental study of heat transfer in a vertical annulus with a rotating inner cylinder," *Int. Journ. of Heat & Mass Transfer*, vol. 32, 1989, pp. 1517-1527.

[BANK] E. Bank, H. Sherman, A. Weiser, "On the regularity of local mesh refinement," *Proc. IMACS World Congress on System Simulation and Scientific Computing*, 8-13 August 1982, Montréal, Canada, pp. 61-64.

[BARR] R. Barrett et al., *Templates for the Solution of Linear Systems: Building Blocks for Iterative Methods*, SIAM, 1994.

[BAST] J. Bastos, N. Ida, R. Mesquita, "A Variable Local Relaxation Technique in Non-linear Problems," *IEEE Trans. on Magnetics*, vol. 31, no. 3, 1995, pp. 1733-1736.

[BEAT] H.W. Beaty, *Electrical Engineering Materials Reference Guide*, McGraw-Hill, 1990.

[BEC1] K.M. Becker, J. Kaye, "Measurement of Adiabatic Flow in an Annulus with an Inner Rotating Cylinder," *Trans. of the ASME, Journ. of Heat Transfer*, vol. 84, 1962, pp. 97-105.

[BEC2] K.M. Becker, J. Kaye, "The Influence of a Radial Temperature Gradient on the Instability of Fluid flow in an Annulus with Inner Rotating Cylinder," *Trans. of the ASME, Journ. of Heat Transfer*, 1962, pp. 106-110.

[BINN] K.J. Binns, P.J. Lawreson, C.W. Trowbridge, *The Analytical and Numerical Solution of Electric and Magnetic Fields*, Wiley, 1992.

[BISH] M.T. Bishop, J.F. Baranowski, D. Heath, S.J. Benna, "Evaluating Harmonic-Induced Transformer Heating," *IEEE Trans. on Power Delivery*, vol. 11, no. 1, 1996, pp. 305-311.

[BOSS] A. Bossavit, *Electromagnétisme, en vue de la modélisation*, Springer Verlag, 1991.

[BOUA] B. Boualem, F. Piriou, "Numerical Models for Rotor Cage Induction Machines using Finite Element Method," *IEEE Trans. on Magnetics*, vol. 34, no. 5, 1988, pp. 3202-3205.

[BOUS] A. Bousbaine, M. McCormick, W.F. Low, "In-situ Determination of Thermal Coefficients for Electrical Machines," *IEEE Trans. on Energy Conversion*, vol. 10, no. 3, 1995, pp. 385-391.

[BRIG] W.L. Briggs, *A Multigrid tutorial*, SIAM, 1987.

[BRO1] P.N. Brown, "A local convergence theory for combined inexact-newton/finite difference projection methods," *SIAM J. Numer. Anal.*, vol. 24, no. 2, 1987, pp. 407-434.

[BRO2] P.N. Brown, Y. Saad, "Hybrid krylov methods for nonlinear systems of equations," *SIAM J. Sci. Stat. Comput.*, vol. 11, no. 3, 1990, pp. 450-481.

[CAME] F. Cameron, R. Pinché, K. Forsman, "Variable Step Size Time Integration Methods for Transient Eddy Current Problems," *IEEE Trans. on Magnetics*, vol. 34, no. 5, 1998, pp. 3319-3322.

[CHAB] C. Chaboudez, S. Clain, R. Glardon, J. Rappaz, M. Swierkosz, R. Touzani, "Numerical Modelling of Induction Heating of Long Workpieces," *IEEE Trans. on Magnetics*, vol. 30, no. 6, 1994, pp. 5028-5037.

[CHEN] S. Chen, K.J. Binns, Z. Liu, D.W. Shimmin, "Finite element analyis of the magnetic field in rare-earth permanent magnet systems with consideration of temperature dependence," *IEEE Trans. on Magnetics*, vol. 28, no. 2, 1992, pp. 1303-1306.

[CHEZ] Y.S. Chen, Z.Q. Zhu, D. Howe, "Influence of Inaccuracies in Machine Parameters on Field-Weakening Performance of PM Brushless AC Drives," *Proc. IEEE International Electric Machines and Drives Conference 1999 (IEMDC'99)*, 9-12 May 1999, Seattle, Washington, USA, pp. 691-693.

[DANI] L. Daniel, C.R. Sullivan, S.R. Sanders, "Design of Microfabricated Inductors," *IEEE Trans. on Power Electronics*, vol. 14, no. 4, 1999, pp. 709-723.

[DEG1] H. De Gersem, R. Mertens, U. Pahner, R. Belmans, K. Hameyer, "A topological method used for field-circuit coupling," *IEEE Trans. on Magnetics*, vol. 34, no. 5, 1998, pp. 3190-3193.

[DEG2] H. De Gersem, D. Lahaye, S. Vandewalle, K. Hameyer, "Comparison of quasi minimal residual and bi-conjugate gradient iterative methods to solve complex symmetric systems arising from time-harmonic magnetic simulations," *COMPEL*, vol. 18, no. 3, 1999, pp. 298-310.

[DELA] M. Delanaye, *Polynomial Finite Volume Schemes for the Compressible Euler and Navier-Stokes Equations on Unstructured Adaptive Grids*, Ph.D. thesis, Univ. de Liège, 1996.

[DENN] J.E. Dennis, R.B. Schabel, *Numerical Methods for Unconstrained Optimization and Nonlinear Equations*, SIAM, 1983.

[DEWE] R. De Weerdt, *Eindige elementen modellering van kooiankerinductiemotoren*, Ph.D. thesis, K.U.Leuven, 1995.

[DONG] J. Dongarra, I. Duff, D. Sorensen, H. Van der Vorst, *Numerical Linear Algebra for High-Performance Computers*, SIAM, 1998.

[DORF] R.C. Dorf, *The Electrical Engineering Handbook*, CRC Press, 1993.

[DR01] J. Driesen, T. Van Craenenbroeck, R. Reekmans, D. Van Dommelen, "Analysing Time-Varying Power System Harmonics using Wavelet Transform," Proc. *IEEE Instrumentation and Measurement Technology Conference (IMTC) '96*, 4-6 June 1996, Brussels, Belgium, pp. 474-479.

[DR02] J. Driesen, T. Van Craenenbroek, D. Van Dommelen, "The registration of harmonic power by analog and digital power meters," *IEEE Trans. on Instrumentation and Measurement*, vol. 47, no. 1, 1998, pp. 195-198.

[DR03] J. Driesen, J. Fransen, R. Belmans, K. Hameyer, "A general-purpose environment for the calculation of coupled thermo-electromagnetic problems," *Proc. 4th Int. Workshop on electric and magnetic fields '98*, 12-15 May 1998, Marseille, France, pp. 541-546.

[DR04] J. Driesen, H. De Gersem, R. Belmans, K. Hameyer, "Coupled thermal-magnetic analysis of a saturated permanent magnet motor," *Proc. Symposium on Power Electronics, Electrical Drives, Advanced machines, power quality (SPEEDAM) '98*, 3-5 June 1998, pp. 1.1-6.

[DR05] J. Driesen, J. Fransen, H. De Gersem, R. Belmans, K. Hameyer, "Object oriented storage of material data for coupled problems," *IEEE Trans. on Magnetics*, vol. 34, no. 5, 1998, pp. 3415-3418.

[DR06] J. Driesen, R. Belmans, K. Hameyer, A. Arkkio, T. Jokinen, "Efficient magnetic-thermal coupled simulation of electrical machines using a double combined FEM-circuit approach," *Proc. Int. Conf. On Electrical Machines (ICEM) '98*, 2-4 September 1998, Istanbul, Turkey, pp. 1402-1407.

[DR07] J. Driesen, R. Belmans, K. Hameyer, "Study of Eddy currents in transformer windings caused by a non-linear rectifier load," *Proc. XV Symposium on Electromagnetic phenomena in nonlinear circuits (EPNC) '98*, 22-24 September 1998, Liège, Belgium, pp. 114-117.

[DR08] J. Driesen, W. Ruythooren, R. Belmans, J. De Boeck, J.-P. Celis, K. Hameyer, "Electric and magnetic FEM modeling strategies for micro-inductors," *IEEE Trans. on Magnetics*, vol. 35, no. 5, 1999, pp. 3577-3579.

[DR09] J. Driesen, R. Belmans, K. Hameyer, "Adaptive relaxation algorithms for thermo-electromagnetic FEM problems," *IEEE Trans. on Magnetics*, vol. 35, no. 3, 1999, pp. 1622-1625.

[DR10] J. Driesen, R. Belmans, K. Hameyer, "Finite element modelling of thermal contact resistances and insulation layers in electrical machines," *Proc. IEEE International Electric Machines and Drives Conference 1999 (IEMDC'99)*, 9-12 May 1999, Seattle, Washington, USA, pp. 222-224.

[DR11] J. Driesen, R. Belmans, K. Hameyer, "Coupled magneto-thermal simulation of thermally anisotropic electrical machines," *Proc. IEEE International Electric Machines and Drives Conference 1999 (IEMDC'99)*, 9-12 May 1999, Seattle, Washington, USA, pp. 469-471.

[DR12] J. Driesen, G. Deliège, T. Van Craenenbroeck, K. Hameyer, "Implementation of the harmonic balance FEM method for large-scale saturated electromagnetic devices," ELECTROSOFT '99 Conf., 17-19 May 1999, Sevilla, Spain, pp. 75-84; published in book *Software for Electrical Engineering – Analysis and Design IV*, WIT Press.

[DR13] J. Driesen, K. Hameyer, "Frequency Domain Finite Element Approximations for Saturable Electrical Machines under Harmonic Driving Conditions," to be published in *COMPEL Journal*, April 2000, 4p.

[DR14] J. Driesen, G. Deliège, K. Hameyer, "Coupled thermo-magnetic simulation of a foil-winding transformer connected to a non-linear load," *Proc. 12th Conf. on the Computation of Electromagnetic Fields (COMPUMAG) '99*, 25-28 October, Sapporo, Japan, pp. II.588-589; extended version (4p.) to be published in *IEEE Trans. on Magnetics*, September 2000.

[DR15] J. Driesen, K. Hameyer, "Practical Method to Determine Additional Load Losses due to Harmonic Currents in Transformers with Wire and Foil Windings," *IEEE Power Engineering Society Winter Meeting*, 23-27 January 2000, Singapore, 6 p.

[DR16] J. Driesen, K. Hameyer, "The simulation of magnetic problems with combined fast and slow dynamics using a transient time-harmonic method," *NUMELEC*, 21-22 March 2000, Poitiers, France, pp.166-167.

[DR17] J. Driesen, K. Hameyer, "Transient Coupled Magnetic Thermal Analysis of a Permanent Magnet Synchronous Electrical Vehicle Motor," accepted for *Int. Conf. On Electrical Machines (ICEM) '00*, 28-30 August 2000, Espoo, Finland, 6 p.

[DUGH] F. Dughiero, M. Forzan, S. Lupi, "Solution of Coupled Electromagnetic and Thermal Problems in Induction Heating Applications," *IEE-Computation in Electromagnetics*, Conference Publication no. 420, 1996, pp. 301-305.

[DUL1] P. Dular, *Modélisation du champ magnétique et des courants induits dans des systèmes tridimensionnels non linéaires*, Ph.D. thesis, Univ. de Liège, 1996.

[DUL2] P. Dular, W. Legros, H. De Gersem, K. Hameyer, "Floating Potentials in Various Electromagnetic Problems using the Finite Element Method," *Proc. 4th Int. Workshop on electric and magnetic fields '98*, 12-15 May 1998, Marseille, France, pp. 409-414.

[DUPR] O. Bottauscio, M. Chiampi, L. Dupré, M. Repetto, M. von Rauch, J. Melkebeek, "Dynamic Preisach modelling of ferromagnetic laminations: a comparison of different finite element formulations," *Journ. de Physique IV*, vol. 8, 1998, pp. 647-650.

[EMAN] IEEE Working Group on Nonsinusoidal Situations: Effects on Meter Performance and Definitions of Power (conv. A.E. Emanuel), "Practical Definitions for Powers in Systems with Nonsinusoidal Waveform and Unbalanced Loads: A Discussion," *IEEE Trans. on Power Delivery*, vol. 11, no. 1, 1996, pp. 79-101.

[FAGU] J.C.S. Fagundes, A.J. Batista, P. Viarouge, "Thermal Modeling of Pot Core Magnetic Components Used in High Frequency Static Converters," *IEEE Trans. on Magnetics*, vol. 33, no. 2, 1997, pp. 1710-1713.

[FEL1] P. Feldmann, B. Melville, D. Long, "Efficient Frequency Domain Analysis of Large Nonlinear Analog Circuits," *IEEE Custom Integrated Circuits Conference (CICC) '96*, 5-8 May 1996, San Diego, California, USA, pp. 461-464.

[FEL2] P. Feldmann, J. Roychowdhury, "Computation of Circuit Waveform Envelops using an Efficient, Matrix-decomposed Harmonic Balance Algorithm," *Proc. Int. Conf. on Computer Aided Design (ICCAD) '96*, 10-14 November 1996, San Jose, California, USA.

[FELI] M. Féliachi, G. Develey, "Magneto-Thermal Behavior Finite Element Analysis for Ferromagnetic Materials in Induction Heating Devices," *IEEE Trans. on Magnetics*, vol. 27, no. 6, 1991.

[FIN1] R.D. Findlay, N. Stranges, "Importance of Rotational Iron Loss Data for Accurate Prediction of Rotating Machine Core Loss," *Proc. IEEE Industry Applications Society Annual Meeting '94*, 2-6 October 1994, Denver, Colorado, USA, 1994, vol. 1, pp. 123-127.

[FIN2] R.D. Findlay, N. Stranges, D.K. MacKay, "Losses due to Rotational Flux in Three Phase Induction Motors," *Proc. 2nd Int. Workshop on Electric and Magnetic Fields*, Leuven, Belgium, 17-20 May 1994, pp. 25-28.

[FOKK] D.R. Fokkema, G.L.G. Sleijpen, H.A. Van Der Vorst, "Accelarated inexact Newton schemes for large systems of nonlinear equations," *SIAM J. Sci. Comput.*, vol. 19, no. 2, pp. 657-674.

[FRE1] E.M. Freeman, D.A. Lowther, "A Novel Mapping Technique for Open Boundary Finite Element Solutions to Poisson Equation," *IEEE Trans. on Magnetics*, vol. 24, no. 6, 1988, pp. 2934-2936.

[FRE2] E.M. Freeman, D.A. Lowther, "An Open Boundary Technique for Axisymmetric and three Dimensional Magnetic and Electric Field Problems," *IEEE Trans. on Magnetics*, vol. 25, no. 5, 1989, pp. 4135-4137.

[FUJI] H. Fujita, "Microactuators and Micromachines," *Proceedings of the IEEE*, vol. 86, no. 8, 1998, pp. 1721-1732.

[FUJW] K. Fujiwara, T. Nakata, N. Okamoto, K. Muramatsu, "Method for Determining Relaxation Factor for Modified Newton-Raphson," *IEEE Trans. on Magnetics*, vol. 29, no. 2, 1992, pp. 1962-1965.

[GALL] A.W. Galli, M.D. Cox, "Temperature Rise of Small Oil-Filled Distribution Transformers Supplying Nonsinusoidal Load Currents," *IEEE Trans. on Power Delivery*, vol. 11, no. 1, 1996, pp. 283-291.

[GAZL] C. Gazley, "Heat-Transfer Characteristic of the Rotational and Axial Flow between Concentric Cylinders," *Trans. of the ASME*, vol. 80, 1958, pp. 79-90.

[GEI1] A. Geist, A. Beguelin, J. Dongorra, W. Jiang, R. Manchek, V. Sunderam, *PVM: Parallel Virtual Machine, A Users' Guide and Tutorial for Networked Parallel Computing*, The MIT Press, 1994.

[GEI2] A. Geist, et al, *PVM3 User's Guide and Reference Manual*, Oak Ridge National Laboratory, September 1994.

[GIAN] D. Giannacopoulos, S. McFee, "Towards Optimal h-p Adaptation Near Singularities in Finite Element Electromagnetics," *IEEE Trans. on Magnetics*, vol. 30, no. 5, 1994, pp. 3523-3526.

[GOLU] G.H. Golub, C.F. Van Loan, *Matrix Computations*, 3rd ed., The John Hopkins University Press, 1996.

[GÖTT] G. Götter, *Erwärmung und Kühlung elektrischer Maschinen*, Springer Verlag, Berlin, 1954.

[GROS] L. Gros, G. Reyne, C. Body, G. Meunier, "Strong Coupling Magneto Mechanical Methods Applied to Model Heavy Magnetostrictive Actuators," *IEEE Trans. on Magnetics*, vol. 34, no. 5, 1998, pp. 3150-3153.

[HAK01] J. Hak, "Lösung eines Wärmequellen-Netzes mit Berücksichtigung der Kühlströme," *Arch. für Elektrotechnik*, 42. Band, 3. Heft, 1956, pp. 137-154.

[HAK02] J. Hak, "Der Luftspalt-Wärmewiderstand einer elektrischen Maschine," *Arch. für Elektrotechnik*, 47. Band, 5. Heft, 1956, pp. 257-272.

[HAK03] J. Hak, "Möglichkeiten und Aussichten einer unbeschränkten Lösing des Wärmeproblems von elektrischen Maschinen," *Elektrotechnik und Maschinenbau*, 74. Jahrgang, Wien, Heft 14, 1957, pp. 305-311.

[HAK04] J. Hak, "Wärmequellen-Netze elektrischer Maschinen," *Elektrotechnik und Maschinenbau*, 76. Jahrgang, Wien, 1959, Heft 11, pp. 236-243.

[HAK05] J. Hak, "Einseitig geheitzte Kanäle in elektrischen Maschinen," *Arch. für Elektrotechnik*, 44. Band, Heft 2, 1959, pp. 107-116.

[HAK06] J. Hak, "Der Wärmewiderstand zwischen Zahn und Joch," *Arch. für Elektrotechnik*, 45. Band, 1. Heft, 1960, pp. 49-58.

[HAK07] J. Hak, "Zwei Ergänzungen zur Wärmequellen-Netzmethode," *Arch. für Elektrotechnik*, 45. Band, 6. Heft, 1960, pp. 407-417.

[HAK08] J. Hak, "Einige zwei- und dreidimensionale Wärmeströmungsprobleme und ihre Näherungslösungen," *Arch. für Elektrotechnik*, 48. Band, 3. Heft, 1963, pp. 190-212.

[HAK09] J. Hak, "Einfluss der Unsicherheit der Berechnung von einzelnen Wärmewiderständen auf die Genauigkeit des Wärmequellen-Netzes," *Arch. für Elektrotechnik*, 47. Band, 6. Heft, 1963, pp. 370-383.

[HAK10] J. Hak, "Die inneren axialen Wärmewiderstände einer elektrischen Maschine," *Arch. für Elektrotechnik*, 48. Band, 1. Heft, 1967, pp. 58-76.

[HAM1] K. Hameyer, J. Driesen, H. De Gersem, R. Belmans, "Computation of quasi static electromagnetic fields with respect to coupled problems," *Proc. 8th Int. IGTE Symposium on Numerical Field Calculation in Electrical Engineering '98*, 21-23 September 1998, Graz, Austria, pp. 100-104.

[HAM2] K. Hameyer, J. Driesen, H. De Gersem, R. Belmans, "The classification of coupled field problems," *IEEE Trans. on Magnetics*, vol. 35, no. 3, 1999, pp. 1618-1621.

[HAM3] K. Hameyer, R. Belmans, *Numerical Modelling and Design of Electrical Machines and Devices*, WIT Press, Southampton-Boston, 1999.

[HAMD] E.S. Hamdi, *Design of Small Electrical Machines*, Wiley, 1994.

[HASH] H. Hashizume, S. Toda, "Electromagnetic Thermal Analysis of Low/High Tc Superconducting Wire," *IEEE Trans. on Magnetics*, vol. 34, no. 5, pp. 3016-3019.

[HAYA] T. Hayase, J.A.C. Humphrey, R. Greif, "Numerical Calculation of Convective Heat Transfer between Rotating Coaxial Cylinders with Periodically Embedded Cavities," *Trans. of the ASME, Journ. of Heat Transfer*, vol. 114, 1992, pp. 589-597.

[HENN] G. Henneberger, K.B. Yahia, M. Schmitz, "Calculation and Identification of a Thermal Equivalent Circuit of a Water Cooled Induction Motor for Electrical Vehicle Applications," *Proc. IEE International Conference on Electrical Machines and Drives '95*, 11-13 September 1995, Durham, UK, pp. 6-10.

[HENS] S. Henneberger, *Design and development of a permanine magnet synchronous motor for a hybrid electric vehicle drive*, Ph.D. thesis, K.U.Leuven, 1998.

[HEUC] K. Heuck, K.-D. Dettmann, *Elektrische Energieversorgung*, Vieweg, 1995, pp. 169-180.

[HO] S.L. Ho, W.N. Fu, H.C. Wong, "Estimation of Stray Losses of Skewed Rotor Induction Motors using Coupled 2-D and 3-D Time Stepping Finite Element Methods, Part I: Main Methods," *IEEE Transaction on Magnetics*, vol. 34, no. 5, Sept. 1998 , pp. 3102-3105.

[HOUT] G. Houtappel, J. Driesen, R. Belmans, K. Hameyer, "Coupled magnetic-thermal behaviour of a single phase transformer," *Proc. 6th Int. Conf. ELECTRIMACS '99*, 14-16 Septmber 1999, Lisboa, Portugal, pp. I/79-I/84.

[HRIB] B. Hribernik, M. Trlep, A. Hamler, "Thermal Evaluation of New Housing of Electrical Machine," *Proc. Int. Conf. On Electrical Machines (ICEM) '98*, 2-4 September 1998, Istanbul, Turkey, pp. 200-202.

[HUEB] K.H. Huebner, E.A. Thornton, T.G. Byrom, *The Finite Element Method for Engineers*, 3rd ed., Wiley, 1995.

[JACO] A. Jacot, M. Swierkosz, J. Rappaz, D. Mari, "Modelling of Electromagnetic Heating, Cooling and Phase Transformations during Surface Hardening of Steels," *Journ. de Physique IV*, vol. 6, 1996.

[JÄNI] L. Jänicke, A. Kost, "Convergence Properties of the Newton-Raphson Method for Nonlinear Problems," *IEEE Trans. on Magnetics*, vol. 34, no. 5, 1998, pp. 2505-2508.

[JANS] H.H.J.M. Janssen, E.J.W. ter Maten, D. van Houwelingen, "Simulation of Coupled Electromagnetic and Heat Dissipation Problems," *IEEE Trans. on Magnetics*, vol. 30, no. 5, 1994, pp. 3331-3334.

[JILE] D. Jiles, *Introduction to magnetism and magnetic materials*, Chapman and Hall London, 1994.

[JOHN] C. Johnson, *Numerical solution of partial differential equations by the finite element method*, Cambridge University Press, 1987.

[JOKI] T. Jokinen, J. Saari, "Modelling of the Coolant Flow with Heat Flow Controlled Temperature Sources in Thermal Networks," *IEE Proc.-Electr. Power Appl.*, vol. 144, no. 5, 1997, p. 338-343.

[KALT] M. Kaltenbacher, H. Landes, R. Lerch, "An Efficient Calculation Scheme for the Numerical Simulation of Coupled Magnetomechanical Systems," *IEEE Trans. on Magnetics*, vol. 33, no. 2, 1997, pp. 1646-1649.

[KAYS] W.M. Kays, I.S. Bjorklund, "Heat Transfer from a rotating cylinder with and without crossflow," *Trans. of the ASME*, vol. 80, 1958, pp. 70-78.

[KELL] C.T. Kelley, D.E. Keyes, "Convergence analysis of pseudo-transient continuation," *SIAM J. Numer. Anal.*, vol. 35, no. 2, 1996, pp. 588-523.

[KOSM] P. Kosmol, *Methoden zur numerischen Behandlung nichtlinearer Gleichungen und Optimierungsaufgaben*, Teubner Studienbücher, 1989.

[KOST] A. Kost, *Numerische Methoden in der Berechnung elektromagnetischer Felder*, Springer Verlag, 1994.

[KREY] E. Kreyszig, *Advanced Engineering Mathematics*, 7th ed., Wiley, 1993.

[KRIS] R. Krishnan, F.C. Doran, "Study of Parameter Sensitivity in High-Performance Inverter-Fed Induction Motor Drive Systems," *IEEE Trans. on Industry Applications*, vol. 23, no. 4, 1987, pp. 623-635.

[KUND] K.S. Kundert, G.B. Sorkin, A. Sangiovanni-Vincentelli, "Applying Harmonic Balance to Almost-Periodic Circuits," *IEEE Trans. on Microwave Theory and Techniques*, vol. 36, no. 2, 1988, pp. 366-378.

[KUT1] N.H. Kutkut, D.M. Divan, "Optimal Air-Gap Design in High-Frequency Foil Windings," *IEEE Trans. on Power Electronics*, vol. 13, no. 5, 1998, pp. 942-949.

[KUT2] N.H. Kutkut, "A Simple Technique to Evaluate Winding Losses Including Two-Dimensional Edge Effects," *IEEE Trans. on Power Electronics*, vol. 13, no. 5, 1998, pp. 950-958.

[KWO] B.-I. Kwon, B.-T. Kim, C.-S. Jun, S.-C. Park, "Analysis of Axially Non-Uniform Loss Distribution in 3-Phase Induction Motor Considering Skew Effect," *IEEE Trans. on Magnetics*, vol. 35, no. 3, 1998, pp. 1298-1301.

[KYLA] G. Kylander, *Thermal Modelling of Small Cage Induction Motors*, techn. report no. 265, Chalmers Univ., Göteborg, Sweden, 1995.

[LAMP] D. Lampard, J. Mugglestone, S.J. Pickering, "Effects of End Winding Porosity upon the Flow Field and Ventilation Losses in the End Region of TEFC Induction Motors," *Proc. IEE International Conference on Electrical Machines and Drives '97*, 1-3 September 1997, Cambridge, UK, pp. 6-10.

[LED1] D. Lederer, A. Kost, "Modelling of Nonlinear Magnetic Material using a Complex Effective Refluctivity," *IEEE Trans. on Magnetics* , vol. 34, no. 5, 1998, pp. 3060-3063.

[LED2] D. Lederer, H. Igarashi, A. Kost, "The Newton-Raphson Method for Complex Equation Systems," *Proc. 7th Int. IGTE Symposium on Numerical Field Calculation in Electrical Engineering '96*, 23-25 September 1996, Graz, Austria, pp. 391 -394.

[LIAO] C. Liao, C.-L. Chen, T. Katcher, "Thermal Management of AC Induction Motors using Computational Fluid Dynamics Modeling," *Proc. IEEE International Electric Machines and Drives Conference 1999 (IEMDC'99)*, 9-12 May 1999, Seattle, Washington, USA, pp. 189-191.

[LIEN] J.H. Lienhard, *A Heat Transfer Textbook*, Prentice-Hall, Engelwood Cliffs, N.J., 1981.

[LIU1] Z.J. Liu, D. Howe, P.H. Mellor, M.K. Jenkins, "Coupled Thermal and Electromagnetic Analysis of a Permanent Magnet Brushless DC Servo Motor," *Proc. IEE International Conference on Electrical Machines and Drives '93*, 8-10 September 1993, Oxford, UK, pp. 631-635.

[LIU2] Z.J. Liu, D. Howe, P.H. Mellor, M.K. Jenkins, "Thermal Analysis of Permanent Magnet Machines," *Proc. IEE International Conference on Electrical Machines and Drives '93*, 8-10 September 1993, Oxford, UK, pp. 359-364.

[LIUW] W.K. Liu, "Parallel Computations for Mixed-time Integrations," ch. 13 in *Numerical Methods for Transient and Coupled Problems*, Wiley, 1987.

[LOW1] D.A. Lowther, E.M. Freeman, B. Forghani, "A Sparse Matrix Open Boundary Method for Finite Element Analysis," *IEEE Trans. on Magnetics*, vol. 25, no. 4, 1989, pp. 2810-2812.

[LOW2] D.A. Lowther, E.M. Freeman, "Other Aspects of the Kelvin Transformation Method for dealing with Open Boundaries," *IEEE Trans. on Magnetics*, 1992, pp. 1667-1670.

[LU1] J. Lu, Y. Li, C. Sun, S. Yamada, "A Parallel Computation Model for Nonlinear Electromagnetic Field Analysis by Harmonic Balance Finite Element Method," *Proc. IEEE Int. Conf. on Algorithms and Architectures for Parallel Processing*, April, 1995, pp. 780-787.

[LU2] J.W. Lu, S. Yamada, H. B. Harrison, "Application of Harmonic Balance-Finite Element Method (HBFEM) in the Design of Switching Power Supplies," *IEEE Trans. on Power electronics*, vol. 11, no. 2, 1996, pp. 347-355.

[LUEP] R.M. Lueptow, A. Docter, K. Min, "Stability of Axial Flow in an Annulus with Rotating Inner Cylinder," *Phys. Fluids A*, vol. 4, no. 11, 1992, pp. 2446-2455.

[LUK1] G.E. Luke, "The cooling of electric machines," *Trans. AIEE*, vol. 45, 1923, pp. 1278-1288.

[LUK2] G.E. Luke, "Surface Heat Transfer in Electric Machines with Forced Air Flow," *Trans. AIEE*, vol. 48, 1926, pp. 1036-1047.

[LUOM] J. Luomi, A. Niemenmaa, A. Arkkio, "On the Use of Effective Reluctivities in Magnetic Field Analysis of Induction Motors fed from a Sinusoidal Voltage

Source," *Proc. Int. Conf. On Electrical Machines (ICEM) '86*, 8-10 September, 1986, München, Germany, pp. 706-709.

[MADH] C.V. Madhusudana, *Thermal Contact Conductance*, Springer, 1996.

[MAGN] *MagNet users manuals*, Infolytica Corp.

[MAYL] R.E. Mayle, C. Hirsch, S. Hess, J. von Woldersdorf, "Rotor-Stator Gap Flow Analysis and Experiments," *IEEE Trans. on Energy Conversion*, vol. 13, no. 2, 1998, pp. 101-110.

[MCCL] C.I. McClay, S. Williamson, "The Influence of Rotor Skew on Cage Motor Losses," *Proc. IEE-International Conference on Electrical Machines and Drives '97*, 1-3 September 1997, Cambridge, UK, pp. 263-267.

[MEL1] P.H. Mellor, D. Roberts, D.R. Turner, "Lumped Parameter Thermal Model for Electrical Machines of TEFC Design," *IEE Proceedings-B*, vol. 138, no. 5, 1991, pp. 205-218.

[MEL2] P.H. Mellor, D.R. Turner, D. Roberts, "Microprocessor Based Induction Motor Thermal Protection," *2nd Int. Conf. on Electrical Machines - Designs and Applications*, London, UK, 1985, pp. 16-20.

[MEMC] *MEMCAD user manuals*, Microcosm Technologies Inc.

[MER1] R. Mertens, *Dynamische eindige elementen simulatie van een inductiemotor in een aandrijfsysteem*, Ph.D. thesis, K.U.Leuven, 1999.

[MER2] R. Mertens, H. De Gersem, R. Belmans, K. Hameyer, D. Lahaye, S. Vandewalle, D. Roose, "An algebraic multigrid method for solving very large electromagnetic systems," *IEEE Trans. on Magnetics*, vol. 34, no. 5, 1998, pp. 3327-3330.

[META] A.C. Metaxas, *Foundations of Electroheat*, Wiley, 1996.

[MICH] L. Michalowsky et al., *Magnettechnik – Grundlagen und Anwendungen*, Fachbuchverlag Leipzig-Köln, 1993.

[MILA] P. Milanfar, J.H. Lang, "Monitoring the Thermal Condition of Permanent-Magnet Synchronous Motors," *IEEE Trans. on Aerospace and Electronic Systems*, vol. 32, no. 4, 1996, pp. 1421-1429.

[MOHA] N. Mohan, T.M. Undeland, W.P. Robbins, *Power Electronics, Converters, Applications and Design*, 2nd ed., Wiley, 1995.

[MOL1] P. Molfino, M. Repetto, "Fully Coupled 'Quasi Axisymmetric' Magneto-Thermal Model for Skin Effects Analysis in Resistive Tokamak Coils," *IEEE Trans. on Magnetics*, vol. 25, no. 5, 1989, pp. 3940-3942.

[MOL2] P. Molfino, M. Repetto, "Comparison of Different Strategies for the Analysis of Nonlineair Coupled Thermo-Magnetic Problems under Pulsed Conditions," *IEEE Trans. on Magnetics*, vol. 26, no. 2, 1990, pp. 559-562.

[MORI] Y. Mori, W. Nakayami, "Forced convective heat transfer in a straight pipe rotating about a parallel axis," *Int. Jounal of Heat & Mass Transfer*, vol. 10, 1966, pp. 1179-1194.

[MUGG] J. Mugglestone, S.J. Pickering, D. Lampard, "Prediction of the Heat Transfer from the End Winding of a TEFC Strip-Wound Induction Motor," *Proc. IEEE International Electric Machines and Drives Conference 1999 (IEMDC'99)*, 9-12 May 1999, Seattle, Washington, USA, pp. 484-486.

[MÜLL] M.A. Müller, S. Williamson, T.J. Flack, K. Atallah, B. Baholo, D. Howe, P.H. Mellor, "Calculation of Iron Losses from Time-Stepped Finite-Element Models of Cage Induction Machines," *Proc. IEE International Conference on Electrical Machines and Drives '95*, 11-13 September 1995, Durham, UK, pp. 88-92.

[NEAG] C. Neagoe, F. Ossart, "Analysis of Convergence on Nonlinear Magnetostatic Finite Elements Problems," *IEEE Trans. on Magnetics*, vol. 30, no. 5, 1994, pp. 2865-2868.

[NEST] H. Nestler, Ph.K. Sattler, "On-Line-Estimation of Temperatures in Electrical Machines by an Observer," *Electric Machines and Power Systems*, 21, 1993, pp. 39-50.

[NIEM] A. Niemenmaa, "Complex Reluctivity Modelling of Iron Losses in Induction Machines," *Proc. Int. Conf. On Electrical Machines (ICEM) '88*, 12-14 September 1988, Pisa, Italy, pp. 633-636.

[NOVO] D.W. Novotny, T.A. Lipo, *Vector control and dynamics of AC drives*, Clarendon Oxford, 1996.

[O'DWY] J. O'Dwyer, T. O'Donnel, "Choosing the relaxation parameter for the solutions of nonlinear magnetic field problems by the Newton-Raphson method," *IEEE Trans. on Magnetics*, vol. 31., 1995, pp. 1484-1487.

[ORFE] M. Orfeuil, *Electric Process Heating*, Battelle Presss, 1987.

[ORTE] J.M. Ortega, W.C. Rheinboldt, *Iterative solutions of nonlinear equations in several variables*, Academic Press New York, 1970.

[PAHN] U. Pahner, *A general design tool for the numerical optimisation of electromagnetic energy transducers*, Ph.D. thesis, K.U.Leuven, 1998.

[PIC1] S.J. Pickering, D. Lampard, N. Hay, T.F. Roylance, "Heat Transfer from the Stator End-Windings of a Low Voltage Concentric-Wound Induction Motor," *Proc. IEE International Conference on Electrical Machines and Drives '95*, 11-13 September 1995, Durham, UK, pp. 477-481.

[PIC2] S.J. Pickering, D. Lampard, N. Hay, T.F. Roylance, "Heat Transfer in a High Voltage, Through-Ventilated 4-pole Induction Motor," *Proc. IEE International Conference on Electrical Machines and Drives '97*, 1-3 September 1997, Cambridge, UK, pp. 11-15.

[PIER] L.W. Pierce, "Transformer Design and Application Considerations for Nonsinusoidal Load Currents," *IEEE Trans. on Industry Applications*, vol. 32, no. 3, 1996, pp. 633-645.

[PLEJ] M. Plejic, B. Hribernik, "Parameter Identification for FEM Thermal Models of Electrical Machines," *Proc. Int. Conf. On Electrical Machines (ICEM) '96*, 10-12 September 1996, Vigo, Spain, pp. 282-285.

[POLI] H. Polinder, M.J. Hoeijmakers, "Eddy-current losses in the segmented surface-mounted magnets of a PM machine," *IEE Proc.-Electr. Power Appl.*, vol. 146, no. 3, 1999, pp. 261-266.

[PRES] W.H. Press, W.T. Vetterling, S.A. Teukolsky, B.P. Flannery, *Numerical Recipes in C*, Cambridge University Press, 1992.

[PUCH] G. Puchner, M. Lindner, D. Roseburg, "Numerische Magnet- und Wärmefeldberechnungen in Grosstransformatoren," *Elektrie*, vol. 43, 12, 1989, pp. 450-452.

[RABI] R. Rabinovici, "Eddy current losses of permanent magnet motors," *IEE Proc-Electr. Power Appl.*, vol. 141, no. 1, 1994, pp. 7-11.

[RAO] S.S. Rao, *The Finite Element Method in Engineering*, 2nd ed., Pergamon Press, 1989.

[RAPP] J. Rappaz, M. Swierkosz, "Mathematical Modelling and Numerical Simulation of Induction Heating Processes," *Appl. Math. Comp. Sci.*, vol. 6, no. 2, 1996, pp. 207-221.

[REN] Z. Ren, A. Razek, "A Strong Coupled Model for Analysing Dynamic Behaviours of Non-linear Electromechanical Systems," *IEEE Trans. on Magnetics*, vol. 30, no. 5, 1994, pp. 3252-3255.

[ROBE] F. Robert, P. Mathys, J.-P. Schauwers, "Ohmic Losses Calculation in SMPS Transformers: Numerical Study of Dowell's approach accuracy," *IEEE Trans. on Magnetics*, vol. 34, no. 4, 1998, pp. 1255-1257.

[SAAD] Y. Saad, *Iterative Methods for Sparse Linear Systems*, PWS Publishing Company, 1996.

[SAAR] J. Saari, *Thermal Analysis of High-Speed Induction Machines*, Ph.D. thesis, Helsinki Univ. of Technology, Lab. of Electromechanics, 1998.

[SAIT] J. Saitz, *Calculation of iron losses in electrical machines*, report no. 51, Helsinki Univ. of Technology, Lab. of Electromechanics, 1997.

[SCHO] N. Schofield, K. Ng, Z.Q. Zhu, D. Howe, "Parasitic Rotor Losses in a Brushless Permanent Magnet Traction Machine," *Proc. IEE International Conference on Electrical Machines and Drives '97*, 1-3 September 1997, Cambridge, UK, pp. 200-204.

[SEBA] T. Sebastian, "Temperature Effects on Torque Production and Efficiency of PM Motors Using NdFeB Magnets," *IEEE Trans. on Industry Applications*, vol. 31, no. 2, 1995, pp. 353-357.

[SERW] R.A. Serway, *Physics for Scientists & Engineers*, 3rd Ed., Saunders College Publishing, 1990.

[SHEW] J.R. Shewchuk, "Triangle: Engineering a 2D Quality Mesh Generator and Delaunay Triangulator," *Proc. 1st Workshop on Applied Computational Geometry*, pp. 124-133, Philadelphia, USA, May 1996.

[SHYL] Y.P. Shylov, Y.A. Ganin, "Thermal Resistance of Metal lic Contacts," *Int. Jounal of Heat & Mass Transfer*, vol. 7, 1963, pp. 921-929.

[SILV] P.P. Silvester, R.L. Ferrari, *Finite elements for electrical engineers*, 3rd ed., Cambridge University Press, 1996.

[SMIT] B.F. Smith, P.E. Bjørstad, W.D. Gropp, *Domain decomposition: parallel multilevel methods for elliptic partial differential equations*, Cambridge University Press, 1996.

[SODE] R. Soderberg, "Steady Flow of Heat in Large Turbine-Generators," *Trans. AIEE.*, 1931, pp. 782-802.

[STEP] R. Stephen et al., "The thermal behaviour of overhead conductors, section 4: mathematical model for evaluation of conductor temperature in the adiabatic state," *Electra*, no. 185, Aug. 1999.

[STRO] B. Stroustrup, *C++ Programming Language*, 3rd ed., Addison-Wesley, 1997.

[THOM] R.E.Thomas, A.J.Rosa, *The analysis and design of linear circuits*, Prentice Hall, 1994.

[TMAT] E.J.W. ter Maten, J.B.M. Melissen, "Simulation of Inductive Heating," *IEEE Trans. on Magnetics*, vol 28, no. 2, 1992, pp. 1287-1290.

[TRIC] D. Trichet, J. Fouladgar, G. Develey, "An Estimator for Equivalent Properties of a Bundle of Conductors using the Inverse Problem Method," *IEEE Trans. on Magnetics*, vol. 34, no. 5, 1998, pp. 2889-2892.

[VACH] A. Vachoux, E. Moser, "VHDL-AMS as a Discrete and Continuous Time Modelling and Simulation Language," published by *IEEE Working Group 1076.1*, 1996.

[VADO] D. Van Dommelen, N. Germay, "Complementary Results of a New Method for the Calculation of Buried Cable Heating," *Revue E*, vol. 6, no. 12, pp. 347-354.

[VAHA] S. Van Haute, *Regeling van synchrone motoren met permanente magneten voor toepassingen met variabele invertorvoedingsspanning*, Ph.D. thesis, K.U.Leuven, 1998.

[VANT] M.G. Vanti, A. Raizer, "Optimal Meshes and h-p Adaptivity," *IEEE Trans. on Magnetics*, vol. 33, no. 2, 1997, pp. 1752-1755.

[VASS] E. Vassent, G. Meunier, J.C. Sabonnadiere, "Simulation of Induction Machine Operation using Complex Magnetodynamic Finite Elements," *IEEE Trans. on Magnetics*, vol. 25, no. 4, 1989, pp. 3064-3066.

[VAVE] L. Vandevelde, J.J.C. Gyselinck, J.A.A. Melkebeek, "Steady-State Finite Element Analysis in the Frequency Domain of Inverter-Fed Squirrel Cage Induction Motors," *Proc. Symposium on Power Electronics, Electrical Drives, Advanced Electrical Motors (SPEEDAM '94)*, Taormina, Italy, June 1994, pp. 29-34.

[WAGN] IEEE Task Force on the Effects of Harmonics on Equipment (conv. V.E. Wagner), "Effects of Harmonics on Equipment," *IEEE Trans. on Power Delivery*, vol. 8, no. 2, 1993, pp. 672-682.

[WHIT] J.K. White, N.R. Aluru, "Coupled-Domain and Mixed Regime Numerical Techniques for Micro-electromechanical Simulations," in *Final Report Workshop Structured Design Methods for MEMS*, 12-15 November 1995, Pasadena, California, USA, pp. 121-122.

[WILL] W.L. Willard, *Numerical methods for stiff equations and singular perturbation problems*, D. Reidel Publishing Company, 1981.

[WONG] H.Y. Wong, *Heat Transfer for Engineers*, Longman, London-New York, 1977.

[WOOD] W.L. Wood, "Some Transient and Coupled Problems – A State-of-the-Art Review," ch. 8 in *Numerical Methods for Transient and Coupled Problems*, Wiley, 1987.

[XYPT] J. Xypteras, V. Hatziathanassiou, "Transient Thermal Field of a Squirrel Gage Motor with Deep-Bar Effect," *Proc. Int. Conf. On Electrical Machines (ICEM) '98*, 2-4 September 1998, Istanbul, Turkey, pp. 429-433.

[YAM1] S. Yamada, K. Bessho, J. Lu, "Harmonic Balance Finite Element method Applied to Nonlinear AC Magnetic Analysis," *IEEE Trans. on Magnetics*, vol. 25, no. 4, 1989, pp. 2971-1973.

[YAM2] S. Yamada, P.P. Biringer, K. Hirano, K. Bessho, "Finite Element Analysis of Nonlinear Dynamic Magnetic Field with DC Component in the Harmonic Domain," *IEEE Trans. on Magnetics*, vol. 26, no. 5, 1990, pp. 2199-2201.

[YOSH] K. Yoshida, K. Kesamaru, Y. Hita, "Eddy Currents Analysis of Surface-Mounted-PMSM by Finite Element Method," *Proc. Int. Conf. On Electrical Machines (ICEM) '98*, 2-4 September 1998, Istanbul, Turkey, pp. 1821-1825.

[ZHU] J. Zhu, S. Hui, V. Ramsden, "Discrete modelling of magnetic cores including hysteresis, eddy current and anomalous losses," *IEE Proc.-A*, vol. 140, pp. 317-322.

[ZIE1] O.C. Zienkiewicz, R.L. Taylor, *The Finite Element Method, Vol. 1, Basic Formulations and Linear Problems*, 4th ed., McGraw-Hill, 1994.

[ZIE2] O.C. Zienkiewicz, R.L. Taylor, *The Finite Element Method, Vol. 2, Solid and Fluid Mechanics, Dynamics and Non-linearity*, 4th ed., McGraw-Hill, 1994.

Appendix A : FEM building blocks

A.1 Standard FEM building blocks for first order elements

In the section 2.3.4, dealing with Finite Element Methods, a number of matrix expressions are introduced, being the basic building blocks of the magnetic, electrical and thermal field computations in the subsequent chapters:

$$H_{ij} = \int_{\Omega_e} \left(N_i \, N_j \right) \mathrm{d}\Omega \tag{A.1}$$

$$K_{ij} = \int_{\Omega_e} \left(\nabla N_i \, \nabla N_j \right) \mathrm{d}\Omega \tag{A.2}$$

$$M_{ij} = \int_{\Omega_e} \left(N_i \, \nabla N_j \right) \mathrm{d}\Omega \tag{A.3}$$

$$F_i = \int_{\Omega_e} N_i \, \mathrm{d}\Omega \tag{A.4}$$

$$C_{ij} = \int_{\Gamma_e} \left(N_i \, N_j \right) \mathrm{d}\Omega \tag{A.5}$$

$$T_{ij} = \int_{\Gamma_e} N_i \, \mathrm{d}\Omega \tag{A.6}$$

The mass matrix contribution K_{ij} has to be altered when the coefficient is an anisotropic tensor quantity. In that case, the coefficient has to be kept within the integrand. Expression (A.2) is to be replaced by:

$$\left(\overline{\lambda} K \right)_{ij} = \int_{\Omega_e} \left(\nabla N_i \cdot \overline{\lambda} \cdot \nabla N_j \right) \mathrm{d}\Omega \tag{A.7}$$

Further on, this constant tensor is assumed to be diagonal with entries λ_x, λ_y and λ_z. Likewise, the contribution due to motion is best considered including the speed term. Thus, (A.3) is replaced by:

$$\left(\vec{v} \cdot M \right)_{ij} = \vec{v} \cdot \int_{\Omega_e} \left(N_i \cdot \nabla N_j \right) \mathrm{d}\Omega \tag{A.8}$$

For the contributions due to the boundary conditions (C_{ij} and T_{ij}), the indices denote the edge, with length or area Γ_e connecting the indicated degrees of freedom.

The function N_i associated with the i^{th} MDOF is one of the shape functions discussed in section 2.3.2. For 2D or 3D first order triangular or tetrahedron elements, this function is written as:

$$\text{2D: } N_i(x,y) = \frac{1}{2\Omega_e}\left(a_i + b_i x + c_i y\right) \tag{A.9}$$

$$\text{3D: } N_i(x,y,z) = \frac{1}{2\Omega_e}\left(a_i + b_i x + c_i y + d_i z\right) \tag{A.10}$$

with x, y and z the global spatial coordinates inside the element's span. The function is zero outside this area. The coefficients and the surface are calculated based on the coordinates of the i^{th} GDOF to which this MDOF is associated (the indices j, k and l indicate the remaining MDOFs/GDOFs):

2D		*3D*	
$a_i = \begin{vmatrix} x_j & y_j \\ x_k & y_k \end{vmatrix}$	(A.11)	$a_i = \begin{vmatrix} x_j & y_j & z_j \\ x_k & y_k & z_k \\ x_l & y_l & z_l \end{vmatrix}$	(A.12)
$b_i = -\begin{vmatrix} 1 & y_j \\ 1 & y_k \end{vmatrix}$	(A.13)	$b_i = -\begin{vmatrix} 1 & y_j & z_j \\ 1 & y_k & z_k \\ 1 & y_l & z_l \end{vmatrix}$	(A.14)
$c_i = -\begin{vmatrix} x_j & 1 \\ x_k & 1 \end{vmatrix}$	(A.15)	$c_i = -\begin{vmatrix} x_j & 1 & z_j \\ x_k & 1 & z_k \\ x_l & 1 & z_l \end{vmatrix}$	(A.16)
-		$d_i = -\begin{vmatrix} x_j & y_j & 1 \\ x_k & y_k & 1 \\ x_l & y_l & 1 \end{vmatrix}$	(A.17)
$\Omega_e = \frac{1}{2}\begin{vmatrix} 1 & x_i & y_i \\ 1 & x_j & y_j \\ 1 & x_k & y_k \end{vmatrix}$	(A.18)	$\Omega_e = \frac{1}{6}\begin{vmatrix} 1 & x_i & y_i & z_i \\ 1 & x_j & y_j & z_j \\ 1 & x_k & y_k & z_k \\ 1 & x_l & y_l & z_l \end{vmatrix}$	(A.19)

Table A.1 First order shape function coefficients

The integrals (A.1)-(A.8) are calculated by means of numerical or analytical integration. Numerical methods, using sampling points, must be of sufficient order. An analytical integration yields the building blocks of Table A.2:

2D		3D	
$\boldsymbol{H} = \frac{\Omega_e}{12}\begin{bmatrix} 2 & 1 & 1 \\ 1 & 2 & 1 \\ 1 & 1 & 2 \end{bmatrix}$	(A.20)	$\boldsymbol{H} = \frac{\Omega_e}{20}\begin{bmatrix} 2 & 1 & 1 & 1 \\ 1 & 2 & 1 & 1 \\ 1 & 1 & 2 & 1 \\ 1 & 1 & 1 & 2 \end{bmatrix}$	(A.21)
$\left(\bar{\lambda}K\right)_{ij} = \frac{1}{4\Omega_e}\left(\lambda_x\left[b_i b_j\right] + \lambda_y\left[c_i c_j\right]\right)$	(A.22)	$\left(\bar{\lambda}K\right)_{ij} = \frac{1}{36\Omega_e}\left(\lambda_x\left[b_i b_j\right] + \lambda_y\left[c_i c_j\right] + \lambda_z\left[d_i d_j\right]\right)$	(A.23)
$\left(M\bar{v}\right)_{ij} = \frac{1}{6}\left[v_x b_i + v_y c_j\right]$	(A.24)	$\left(M\bar{v}\right)_{ij} = \frac{1}{24}\left[v_x b_i + v_y c_j + v_z d_k\right]$	(A.25)
$\boldsymbol{F} = \frac{\Omega_e}{3}\begin{bmatrix} 1 \\ 1 \\ 1 \end{bmatrix}$	(A.26)	$\boldsymbol{F} = \frac{\Omega_e}{3}\begin{bmatrix} 1 \\ 1 \\ 1 \\ 1 \end{bmatrix}$	(A.27)
$\boldsymbol{C} = \frac{\Gamma_e}{6}\begin{bmatrix} 2 & 1 & 0 \\ 1 & 2 & 0 \\ 0 & 0 & 0 \end{bmatrix}$	(A.28)	$\boldsymbol{C} = \frac{\Gamma_e}{12}\begin{bmatrix} 2 & 1 & 1 & 0 \\ 1 & 2 & 1 & 0 \\ 1 & 1 & 2 & 0 \\ 0 & 0 & 0 & 0 \end{bmatrix}$	(A.29)
$\boldsymbol{T} = \frac{\Gamma_e}{2}\begin{bmatrix} 1 \\ 1 \\ 0 \end{bmatrix}$	(A.30)	$\boldsymbol{T} = \frac{\Gamma_e}{3}\begin{bmatrix} 1 \\ 1 \\ 1 \\ 0 \end{bmatrix}$	(A.31)

Table A.2 Standard FEM building block for first order triangular or tetrahedron elements

ADAPTIEVE MESHVERFIJNING

7.1 Inleiding

Adaptieve meshverfijning is de combinatie van een a-posteriori foutenschatter en een verfijningsalgoritme. De foutenschatter geeft aan welke elementen verfijnd moet worden en een verfijningsalgoritme zal de aangeduide elementen daadwerkelijk verfijnen. Het verfijnen van de elementen op basis van een foutenschatter geeft een betere convergentie dan wanneer alle elementen verfijnd worden. De helling van de globale fout $|e|$ in figuur 7.1 is een maat voor de convergentiesnelheid.

$$|e| = \left| \frac{W - W_{N_n=\infty}}{W_{N_n=\infty}} \right| \tag{0.1}$$

met

W: energie in het model
N_n: aantal knooppunten
$W_{N_n=\infty}$: energie in een model met een oneindig aantal knooppunten

Praktisch wordt $W_{N_n=\infty}$ bij een voldoend hoog aantal knooppunten bepaald, d.w.z. het aantal knooppunten is 'beduidend' hoger dan bij de modellen die men wenst te onderzoeken.

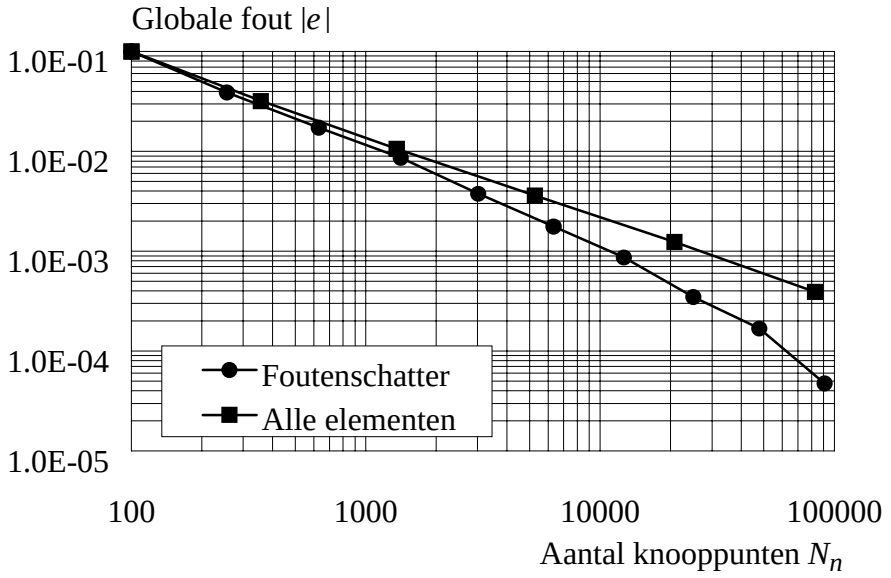

figuur 0.1: *Globale fout in functie van het aantal knooppunten: convergentiesnelheid*

7.2 A-posteriori foutenschatter

7.2.1 Bepaling van de te verfijnen elementen

Een a-posteriori foutenschatter maakt op basis van een reeds berekende oplossing een schatting van de lokale fout e_k per element. Deze lokale fout wordt genormeerd d.w.z. gedeeld door de maximale fout over alle elementen om een lokale fout per element tussen 0 en 1 te bekomen ofwel tussen 0 en 100 %.

$$e_k = \frac{e_k}{\max\left(e_k\right)} \tag{0.2}$$

Door de gebruiker wordt nu een maximaal toegelaten lokale fout ε_{lokaal} ingesteld. Alle elementen met een fout groter dan deze maximaal toegelaten lokale fout (bv. 10 %) komen in aanmerking voor verfijning.

$$e_k > \varepsilon_{lokaal} \tag{0.3}$$

Al deze elementen worden gerangschikt naar hun fout. De elementen met de grootste fout worden het eerst verfijnd. Het aantal elementen dat verfijnd wordt, wordt bepaald door het maximum percentage van nieuwe elementen *p* ingesteld door de gebruiker (bv. 100 %). Het maximum aantal elementen N_v dat verfijnd wordt, wordt gegeven door

$$N_v = p \cdot c \cdot N_e \tag{0.4}$$

met

N_e : aantal elementen
c: constante afhankelijk van de gebruikte verfijningsmethode

De constante *c* is een maat voor de verhouding van het aantal verfijnde elementen tot het aantal nieuwe elementen: $c = 1/4$ voor een edge gebaseerde verfijning en $c = 1/3$ voor een element gebaseerde verfijning.

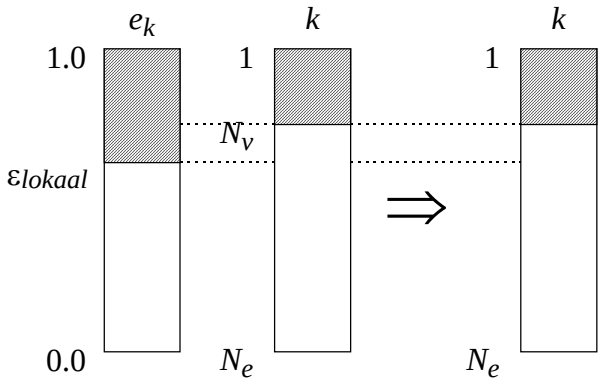

figuur 0.2: *Bepaling van de te verfijnen elementen*

7.2.2 Model gebaseerd ↔ label gebaseerd

Een model gebaseerde foutenschatter berekent de lokale fout van alle elementen in het model en de lokale fout wordt genormeerd door deling met de maximale lokale fout in het model. Het maximum aantal elementen dat verfijnd wordt, wordt bepaald door het totaal aantal elementen in het model.

Een label gebaseerde foutenschatter berekent voor elk label afzonderlijk de lokale fout en de normering is op basis van de maximale fout binnen het label. Het maximum aantal elementen $N_{v,l}$ dat verfijnd wordt, wordt bepaald door het aantal elementen $N_{e,l}$ met eenzelfde label.

$$N_{v,l} = p \cdot c \cdot N_{e,l} \tag{0.5}$$

Dit heeft als voordeel dat er elementen verfijnd worden over het ganse model. Maar er wordt ook verfijnd in gebieden waar het niet echt nodig is.

7.2.3 Voorbeelden van foutenschatters

7.2.3.1 Energie in een element

De energie W_k in een element is een indicatie voor de lokale fout e_k.

$$e_k = W_k \tag{0.6}$$

7.2.3.2 Magnetische inductie in een knooppunt

De magnetische inductie $B_{n,i}$ in een knooppunt i is het gewogen gemiddelde van de grootte van de magnetische inducties $B_{e,k}$ van de omliggende elementen k behorende tot hetzelfde label (figuur 7.3). De weging is op basis van de oppervlakte Δ_k van de elementen.

$$B_{n,i} = \frac{\sum_{k=1}^{n} B_{e,k} \cdot \Delta_k}{\sum_{k=1}^{n} \Delta_k} \tag{0.7}$$

De lokale fout e_k in een element is berekend als het verschil tussen de grootte van de magnetische inductie in het element en het gemiddelde van de drie knooppuntswaarden.

$$e_k = \left| B_{e,k} - \frac{\sum_{i=1}^{3} B_{n,i}}{3} \right| \tag{0.8}$$

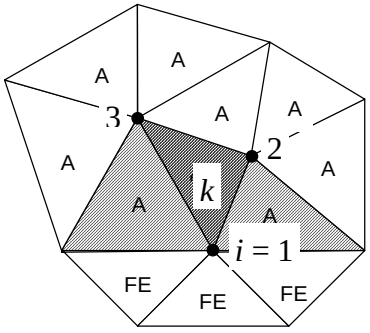

figuur 0.3: *Berekening van de magnetische inductie in een knooppunt*

7.2.3.3 Magnetische inductie in een knooppunt gewogen met de energie

De lokale fout e_k op basis van de magnetische inductie in de knooppunten wordt gewogen met de energie W_k in een element.

$$e_k = W_k \left| B_{e,k} - \frac{\sum_{i=1}^{3} B_{n,i}}{3} \right| \tag{0.9}$$

7.3 Verfijningsalgoritme

7.3.1 Verfijningsmethode

Er bestaan twee methodes om elementen te verfijnen. De eerste methode is een element gebaseerde methode d.w.z. een nieuw knooppunt wordt in het midden van een element geplaatst (figuur 7.4). De tweede methode is een edge gebaseerde methode d.w.z. drie nieuwe knooppunten worden op de drie zijden van een element geplaatst.

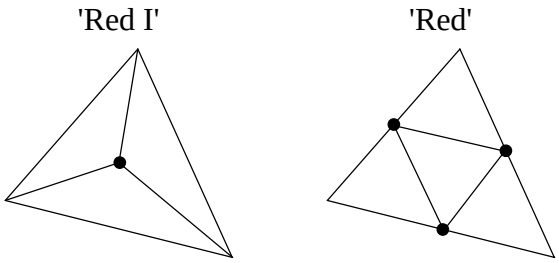

figuur 0.4: *Element en edge gebaseerde verfijning*

De element gebaseerde methode heeft als voordeel dat het aantal nieuwe knooppunten per element en dus ook het aantal nieuwe elementen per adaptiestap laag is. Bij deze methode van verfijnen heeft de verfijning van een element geen onmiddelijke invloed op de naburige elementen. Een nadeel is dat de initiële aspect ratio van de nieuwe elementen slechter is dan die van het oorspronkelijk element. Bovendien moeten de randen speciaal behandeld worden (figuur 7.5).

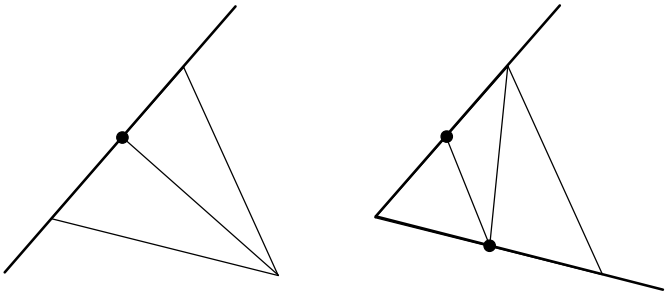

figuur 0.5: *Verfijning van randen bij de element gebaseerde methode*

De edge gebaseerde methode heeft als nadeel dat het aantal nieuwe knooppunten per element hoog is en dat naburige elementen beïnvloed worden door de verfijning van een element. Daarom kan men bij deze methode drie verschillende te verfijnen elementen onderscheiden naargelang het aantal te verfijnen zijden van het element (figuur 7.6). Deze manier van verfijnen heeft als voordeel dat er geen onderscheid gemaakt moet worden tussen randen en interne zijden van elementen. Bovendien is de initiële aspect ratio van de nieuwe elementen gelijk aan die van het oorspronkelijk element.

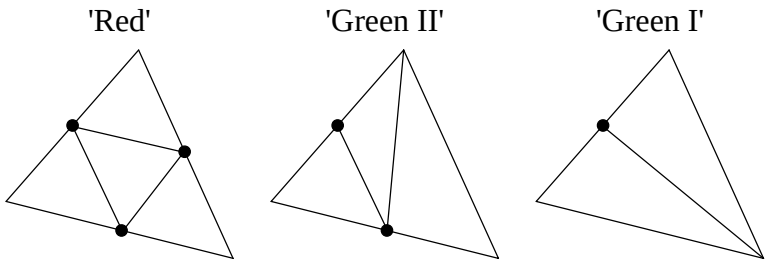

figuur 0.6: *Red, Green II en Green I elementen*

7.3.2 Aspect ratio

De aspect ratio γ van een driehoekig element is berekend als de verhouding van de straal *R* van de omschreven cirkel tot tweemaal de straal *r* van de ingeschreven cirkel (figuur 7.7). Een gelijkzijdige driehoek heeft een aspect ratio van 1.

$$\gamma = \frac{R}{2r} \tag{0.10}$$

$$\gamma = \frac{abc}{8(s-a)(s-b)(s-c)} \tag{0.11}$$

met *a*, *b* en *c* de lengte van de drie zijden en *s* de halve omtrek van de driehoek.

$$s = \frac{a+b+c}{2} \tag{0.12}$$

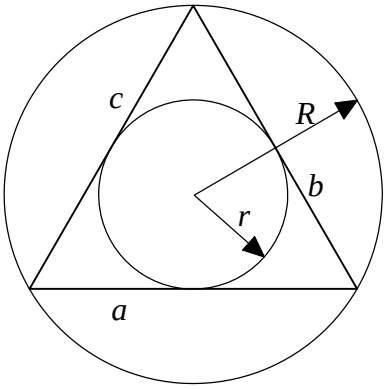

figuur 0.7: *Ingeschreven en omschreven cirkel van een driehoek*

7.3.3 Delaunay vermazing

De kwaliteit van een vermazing wordt gekenmerkt door

- de grootte van de elementen,
- een gemiddelde aspect ratio dicht bij de eenheid,
- een lage slechtste aspect ratio,
- de mogelijkheid om de originele geometrie te herstellen.

Een Delaunay vermazing is een eerste stap naar een vermazing met een lage gemiddelde aspect ratio. De definitie van zo een vermazing luidt: 'voor elk paar van naast elkaar liggende elementen geldt dat het minimum van de zes hoeken in de twee driehoeken groter is dan dat van de twee driehoeken gevormd door het omwisselen van de diagonaal van de gevormde vierhoek'.

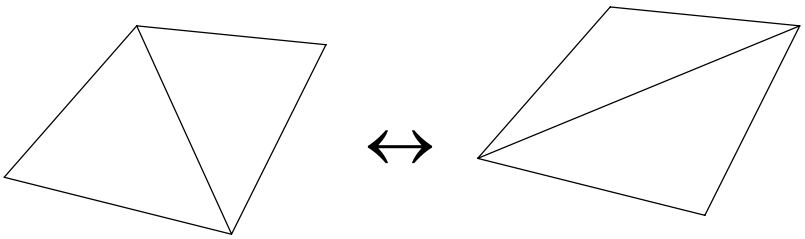

figuur 0.8: *Omwisseling van de diagonaal van de gevormde vierhoek*

Elk paar van naast elkaar liggende elementen behorend tot hetzelfde label wordt getest. De omschreven cirkel van een van de twee driehoeken wordt bepaald. Ligt het vierde knooppunt binnen de omschreven cirkel (figuur 7.9), dan moet de diagonaal van de gevormde vierhoek omgewisseld worden. Praktisch wordt echter nooit de omgeschreven cirkel berekend daar dit teveel rekentijd vergt.

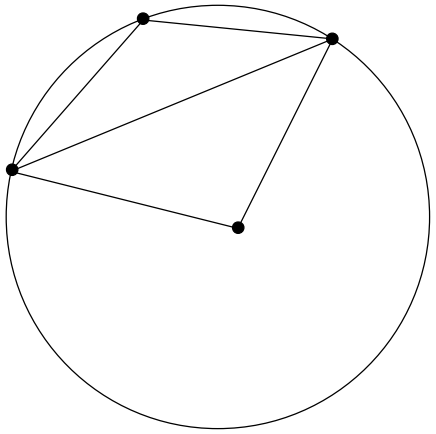

figuur 0.9: *Testen van de Delaunay vermazing*

7.3.4 Cline & Renka test

Wanneer knooppunt *b* binnen de omschreven cirkel van de driehoek gevormd door de knooppunten *a*, *c* en *d* ligt, geldt overeenkomstig figuur 7.10

$$2\pi R - 2R\alpha < 2R\beta \tag{0.13}$$

$$\alpha + \beta > \pi \tag{0.14}$$

ofwel

$$\sin(\alpha + \beta) < 0 \tag{0.15}$$

$$\sin(\alpha)\cdot\cos(\beta) + \cos(\alpha)\cdot\sin(\beta) < 0 \tag{0.16}$$

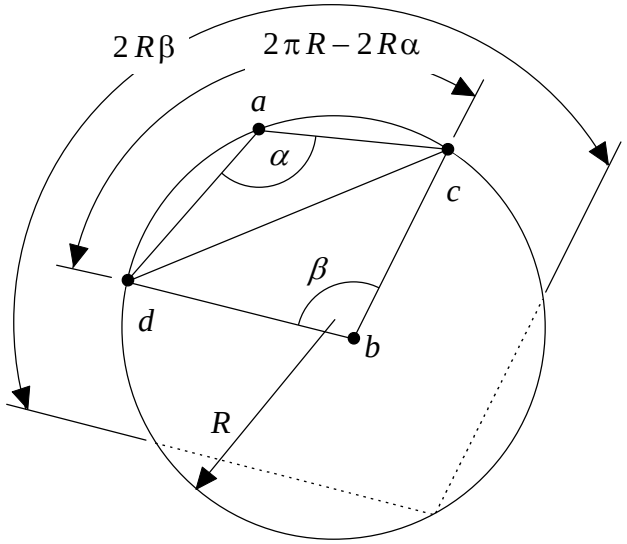

figuur 0.10: *Cline & Renka test*

Afrondingsfouten kunnen problemen veroorzaken wanneer $\sin(\alpha + \beta)$ naar nul nadert. Dit treedt op wanneer

- $\alpha + \beta$ naar π nadert,
- α en β beide naar 0 naderen,
- α en β beide naar π naderen.

In het eerste geval ligt knooppunt *b* nagenoeg op de omschreven cirkel en zal het omwisselen van de diagonaal geen slechte gevolgen hebben. In de laatste twee gevallen kan het omwisselen van de diagonaal tot een foutieve vermazing aanleiding geven. Daarom worden in het algoritme een aantal voorafgaande testen ingebouwd.

Stap 1:
$$\cos(\alpha) = (x_a - x_c)\cdot(x_a - x_d) + (y_a - y_c)\cdot(y_a - y_d)$$
$$\cos(\beta) = (x_b - x_c)\cdot(x_b - x_d) + (y_b - y_c)\cdot(y_b - y_d)$$

Stap 2: if $(\cos(\alpha) \geq 0 \quad \text{en} \quad \cos(\beta) \geq 0)$
then swap=TRUE
exit

Stap 3: if $(\cos(\alpha) < 0 \quad \text{en} \quad \cos(\beta) < 0)$
then swap=FALSE
exit

Stap 4:
$$\sin(\alpha) = (x_a - x_c)\cdot(y_a - y_d) - (y_a - y_c)\cdot(x_a - x_d)$$
$$\sin(\beta) = (x_b - x_c)\cdot(y_b - y_d) - (y_b - y_c)\cdot(x_b - x_d)$$
$$\sin(\alpha + \beta) = \sin(\alpha)\cdot\cos(\beta) + \cos(\alpha)\cdot\sin(\beta)$$

Stap 5: if $(\sin(\alpha + \beta) < 0)$
then swap=TRUE
exit
else swap=FALSE
exit

figuur 0.11: *Cline & Renka algoritme*

7.3.5 Delaunay algoritme van Lawson

Telkens een nieuw knooppunt aan de bestaande vermazing wordt toegevoegd, dient de bestaande vermazing aangepast te worden opdat opnieuw een Delaunay vermazing bekomen wordt. Praktisch wil dit zeggen dat in het verfijningsalgoritme knooppunt per knooppunt wordt toegevoegd en er telkens getest wordt. Dit kan gebeuren met het Delaunay algoritme van Lawson dat geschikt is voor een element gebaseerde verfijningsmethode. Figuur 7.11 toont de initiële vermazing met 11 knooppunten en 12 elementen.

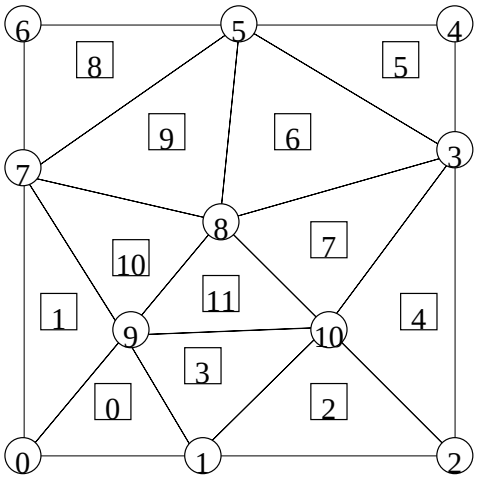

figuur 0.12: *Initiële vermazing*

In het Delaunay algoritme van Lawson worden de elementen die naast de zijde tegenover het nieuw knooppunt liggen op een LIFO-stapel (last-in, first-out) geplaatst. Dit zijn maximaal drie elementen. Alle elementen worden een voor een van de stapel gehaald en telkens wordt er getest of het nieuw knooppunt binnen de omschreven cirkel van het element ligt. Ligt het nieuw knooppunt binnen de omschreven cirkel, dan wordt de diagonaal van de beschreven vierhoek gewisseld om twee betere elementen te genereren. De elementen de nu naast een zijde van de nieuwe elementen tegenover het nieuwe knooppunt liggen, worden op de stapel geplaatst.

Figuur 7.13 illustreert dit algoritme voor de initiële vermazing van figuur 7.12. Volgens een a-posteriori foutenschatter dient het element met nummer 6 verfijnd te worden. Het nieuw knooppunt dat het nummer 11 krijgt, wordt in het midden van het element geplaatst (figuur 7.13a). Figuur 7.13b toont de drie nieuwe elementen. Een van de drie elementen krijgt het oude elementnummer. De andere twee elementen krijgen de nummers 12 en 13. Per nieuw knooppunt neemt het aantal elementen met twee toe. De drie elementen die naast de zijde tegenover het nieuw knooppunt liggen worden op de stapel geplaatst (figuur 7.13c). Het element dat het laatst op de stapel is geplaatst, wordt er het eerst afgehaald. Er wordt getest of het nieuw knooppunt binnen de omschreven cirkel van het element ligt (figuur 7.13d). Dit blijkt het geval te zijn en de diagonaal van de beschreven vierhoek wordt gewisseld (figuur 7.13e). Omdat er geen elementen zijn die nu naast een zijde van de nieuwe elementen tegenover het nieuwe knooppunt liggen, dienen er geen elementen op de stapel geplaatst te worden. Het volgende element wordt van de stapel gehaald en er wordt getest of het nieuw knooppunt binnen de omschreven ligt (figuur 7.13f). Ook nu dient de diagonaal van de gevormde vierhoek gewisseld te worden (figuur 7.13g). Omdat er nu twee elementen zijn die naast een zijde van de nieuwe elementen tegeover het nieuw knooppunt liggen, worden deze op de stapel geplaatst (figuur 7.13h). Er zitten nu drie elementen op de stapel. Het volgende element wordt van de stapel gehaald en er wordt getest (figuur 7.13i). Er dient niet gewisseld te worden en hetzelfde geldt voor het volgende element op de stapel (figuur 7.13j). Tenslotte wordt het laatste element op de stapel van de stapel gehaald en er wordt getest (figuur 7.13k). Het nieuw knooppunt ligt niet binnen de omschreven cirkel van het laatst van de stapel gehaalde element. Figuur 7.13l toont de resulterende Delaunay vermazing.

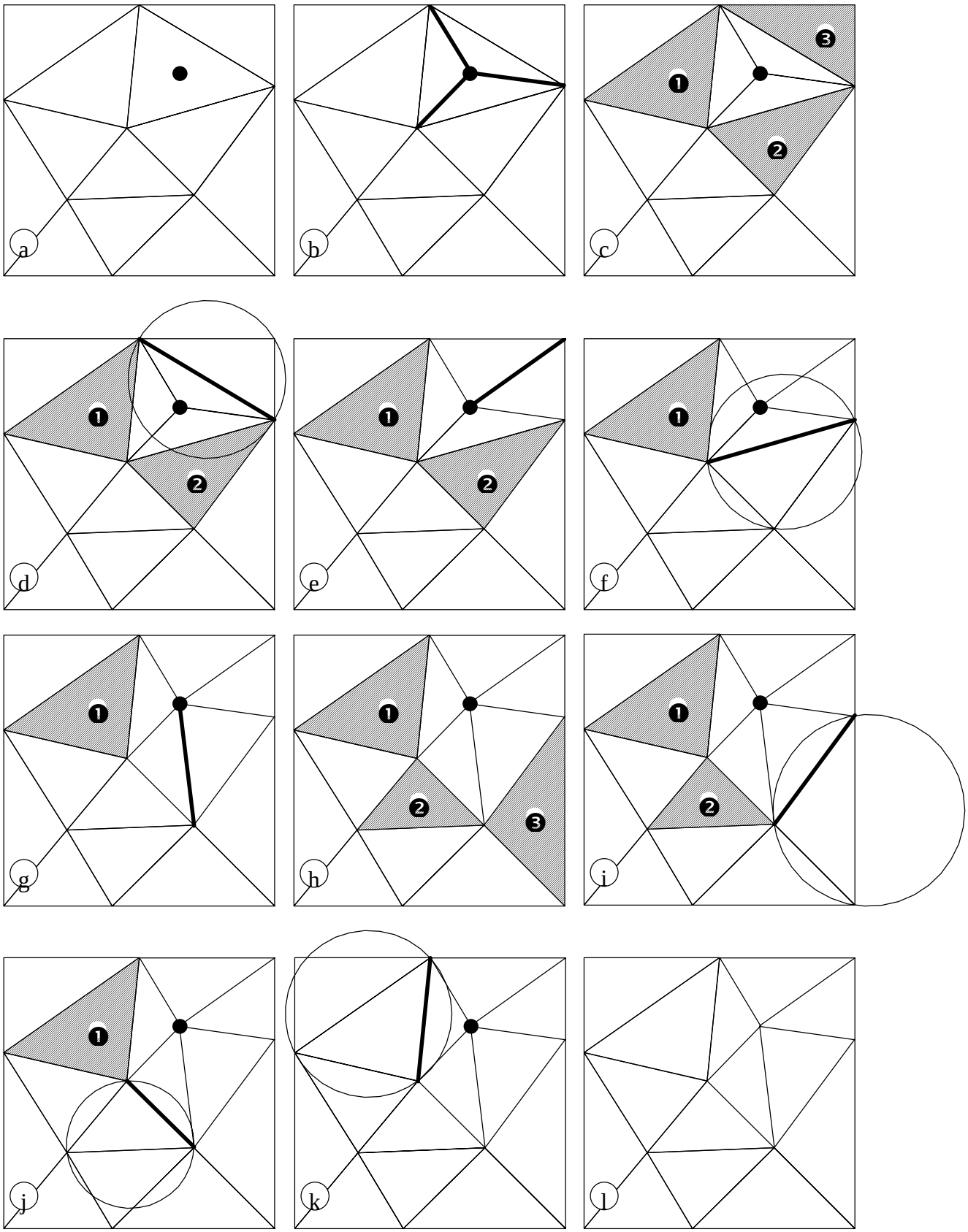

figuur 0.13: *Delaunay algoritme van Lawson*

7.3.6 'Intelligente' datastructuren

Vertrekkend van de element matrix '*elem*' die aanduid uit welke knooppunten elk element is opgebouwd, kan eenvoudig de knooppunt naar element matrix '*nodeelem*' opgebouwd worden (figuur 7.14). Deze matrix geeft voor elk knooppunt de omliggende elementen. Bovendien wordt het aantal omliggende elementen bijgehouden in een vector '*surrelem*'. Figuur 7.15 geeft de element matrix voor de initiële vermazing van figuur 7.12 en figuur 7.16 de knooppunt naar element matrix.

```
for (k=0;k<numelem;k++)
      for (i=0;i<3;i++)
            nodeelem[elem[k,i],surrelem[elem[k,i]]]=k;
            surrelem[elem[k,i]]++;
```

figuur 0.14: *Opbouw van de knooppunt naar element matrix*

0	0	1	9
1	0	9	7
2	1	2	10
3	1	10	9
4	2	3	10
5	3	4	5
6	3	5	8
7	3	8	10
8	5	6	7
9	5	7	8
10	7	9	8
11	8	9	10

figuur 0.15: *Element matrix*

0	0	1				2
1	0	2	3			3
2	2	4				2
3	4	5	6	7		4
4	5					1
5	5	6	8			4
6	8					1
7	1	8	9	10		4
8	6	7	9	10	11	5
9	0	1	3	10	11	5
10	0	3	4	7	11	5

figuur 0.16: *Knooppunt naar element matrix en de vector met het aantal omliggende elementen*

De buurelement matrix kan nu snel opgebouwd worden. Voor elke zijde van een element wordt het buurelement bepaald. In de twee rijen van de knooppunt naar element matrix wordt gezocht naar gemeenschappelijke elementnummers. Het element zelf komt voor en indien er een ander elementnummer gevonden wordt, is dat het nummer van het buurelement. Zoals blijkt uit figuur 7.16 zijn de rijen van de knooppunt naar element matrix geordend. Dit wil zeggen dat zeer snelle zoekalgoritmes gebruikt kunnen worden die van deze ordening gebruik maken. Bovendien is het maximum aantal omliggende elementen nagenoeg een constante. D.w.z. dat zelfs als het aantal knooppunten toeneemt, men over een constant aantal elementen moet zoeken. De eenvoudige kwadratische zoekalgoritmes die gebruikt kunnen worden, zijn vervangen door lineaire zoekalgoritmes die gebruik maken van een aantal 'intelligente' datastructuren. Bovendien zijn deze datastructuren eenvoudig (lineair) op te bouwen. Figuur 7.17 toont de buurelement matrix voor de initiële vermazing. Er dient opgemerkt te worden dat tijdens de opbouw van de buurelement matrix rekening wordt gehouden met binaire randvoorwaarden. Elementen die door middel van binaire randvoorwaarden met elkaar verbonden zijn, zijn buurelementen.

0		3	1
1	0	10	
2		4	3
3	2	11	0
4		7	2
5			6
6	5	9	7
7	6	11	4
8			9
9	8	10	6
10	1	11	9
11	10	3	7

figuur 0.17: *Buurelement matrix*

7.3.7 Edge gebaseerde verfijning

Met behulp van de buurelement matrix kan een edge gebaseerde verfijning eenvoudig geïmplementeerd worden. De grote moeilijkheid is dat het verfijnen van een element de buurelementen beïnvloedt. De foutenschatter bepaald welke elementen verfijnd moeten worden. Op basis van deze vector worden de zijden van deze elementen als te verfijnen gemarkeerd. Dit wordt gedaan door in de te verfijnen zijden matrix '*refedge*' het nummer van het nieuw knooppunt behorend bij deze zijde in te vullen. Gelijktijdig wordt dezelfde zijde van het buurelement met hetzelfde knooppuntnummer gemarkeerd. Wanneer het om een elementen gaat die via binaire randvoorwaarden met elkaar verbonden zijn, wordt het volgende knooppuntnummer toegekend. Figuur 7.18 toont de te verfijnen zijden matrix overeennkomstig de verfijning van figuur 7.19. Opnieuw wordt het element met nummer 6 als enige verfijnd ('Red' element). Doordat zijden van een element verfijnd worden, zijn de elementen 5, 7 en 9 'Green I' elementen.

0			
1			
2			
3			
4			
5			11
6	11	12	13
7	13		
8			
9			12
10			
11			

figuur 0.18: *De te verfijnen zijden matrix*

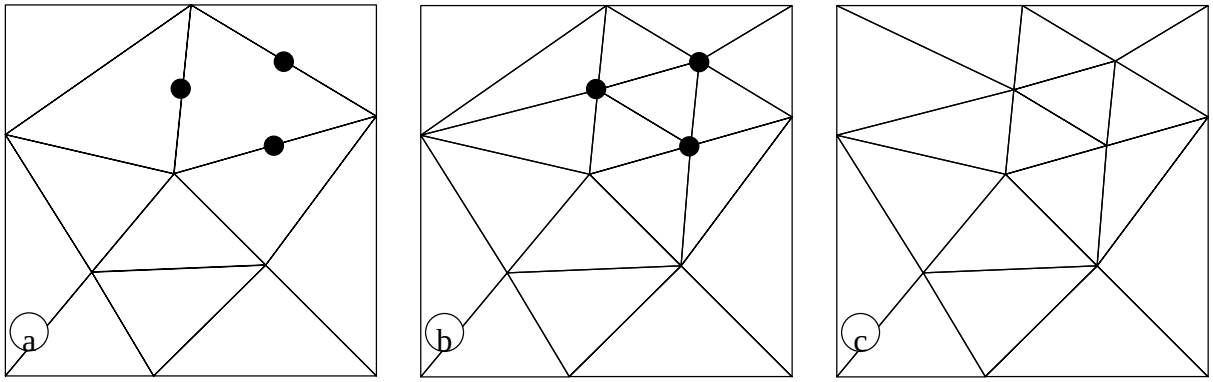

figuur 0.19: *Edge gebaseerde verfijning*

Nadat alle zijden die moeten verfijnd worden, gemarkeerd zijn, wordt elk element verfijnd overeenkomstig figuur 7.6. Er wordt niet tussentijds getest of er een Delaunay vermazing gegenereerd wordt. Daar een Delaunay vermazing uniek is, volstaat een globaal Delaunay algoritme om een Delaunay vermazing te genereren met de bestaande knooppunten. Een mogelijk algoritme bestaat erin om een lus op te stellen over alle knooppunten en te testen tussen twee naast elkaar liggende omliggende elementen. Het aantal omwisselingen wordt geteld en de lus wordt herhaald tot er geen omwisselingen meer hebben plaatsgevonden. De op deze manier bekomen vermazing is opnieuw een Delaunay vermazing (figuur 7.19c). Praktisch wordt het algoritme beëindigd indien het aantal omgewisselde zijden lager is dan 10 % van het aantal omgewisselde zijden in de eerste lus. Daar het aantal omwisselingen relatief laag is bij een edge gebaseerde verfijning, is de gegenereerde vermazing van voldoende hoge kwaliteit. Maar het is strikt genomen geen Delaunay vermazing.

7.3.8 Herstelling van de originele geometrie

Een ander kenmerk van een verfijningsalgoritme dat hoog kwalitatieve vermazingen genereert, is dat de originele geometrie hersteld wordt wanneer elementen verfijnd worden. Daarom wordt van elke zijde van een element dat op de rand van een gebied ligt, bijgehouden tot welke primitieve (boog, cirkel of rechte) de zijde behoort. Wordt zo'n zijde verfijnd, dan wordt het nieuw knooppunt niet in het midden van de zijde geplaatst. Bij het verfijnen van bogen en cirkels wordt daarom overgeschakeld op polaire coördinaten. Het nieuw knooppunt komt halfweg in termen van hoeken tussen de twee knooppunten te liggen (figuur 7.20).

$$\rho_n = \frac{\rho_i + \rho_j}{2} \tag{0.17}$$

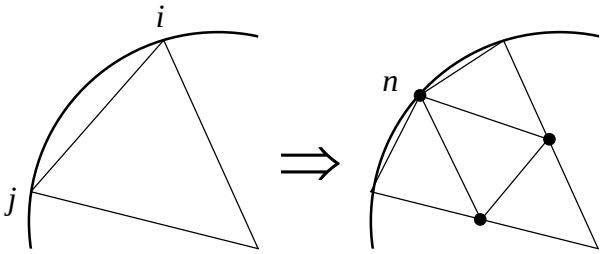

figuur 0.20: *Vormherstelling bij het verfijnen van een element*

7.3.9 Verschuiven van knooppunten

Verschuiving van knooppunten levert een betere gemiddelde aspect ratio op. Hiervoor een knooppunt naar het zwaartepunt van de omliggende knooppunten verschoven (figuur 7.21). Telkens wordt getest of er geen elementen ontstaan met een negatieve oppervlakte.

$$x_n = \frac{1}{n}\sum_{i=0}^{n-1} x_i \tag{0.18}$$

$$y_n = \frac{1}{n}\sum_{i=0}^{n-1} y_i \tag{0.19}$$

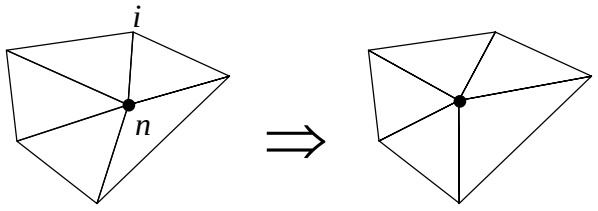

figuur 0.21: *Verschuiving van knooppunten*

Het edge gebaseerd verfijningsalgoritme kan eenvoudig uitgebreid worden met een verschuiving van knooppunten. De eenvoudige lus die over de knooppunten loopt en test of er tussen twee naast elkaar liggende omliggende elementen gewisseld moet worden, wordt uitgebreid overeenkomstig figuur 7.22. Een knooppunt wordt verschoven naar het zwaartepunt van de omliggende knooppunten, waarna getest wordt op de omliggende elementen. Indien er elementen gewisseld werden, wordt het knooppunt nogmaals verschoven naar het zwaartepunt van de nu omliggende knooppunten. De lus over alle knooppunten wordt enkele malen herhaald totdat het aantal gewisselde elementen voldoende laag is geworden. Figuur 7.23a toont de vermazing zonder verschuiving van de knooppunten, na een lus (figuur 7.23b) en na twee lussen (figuur 7.23c) van verschuiven en omwisselen. Na twee lussen was er geen enkel omwisselingen meer.

```
for (i=0;i<numnode;i++)
      movenode(i);
      swapedge(i,swapped);
      if (swapped=TRUE)
            movenode(i);
```

figuur 0.22: *Uitgebreid testalgoritme*

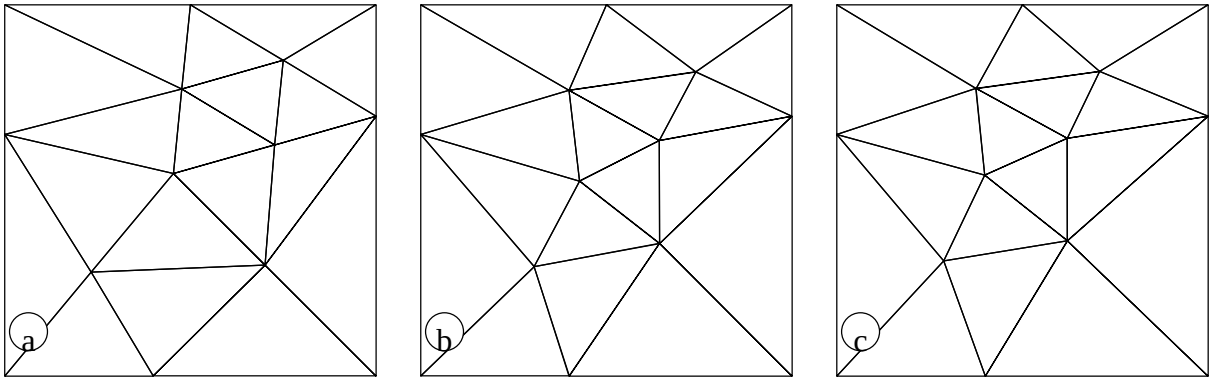

figuur 0.23: *Vermazing met verschuiving van knooppunten*

7.3.10 Startoplossing voor de volgende adaptiestap

Daar het oplossen van het stelsel van lineaire vergelijking via een iteratieve methode gebeurd, is een startoplossing vereist. De eerste startoplossing is een reeds berekende en ingelezen oplossing of de nuloplossing. De startoplossing voor de volgende adaptiestap wordt bepaald door een benaderende interpolatie van de berekende oplossing voor de nieuwe knooppunten. Er wordt immers geen rekening gehouden met de verschuiving van de knooppunten. Wanneer een zijde verfijnd wordt, wordt door interpolatie de oplossing op het nieuw knooppunt bepaald. De geïnterpoleerde waarde is imeers het gemiddelde van de twee knooppunten die de zijde beschrijven. Later zal dit knooppunt waarschijnlijk verschoven worden, maar hier wordt geen rekening meegehouden daar het om een startoplossing gaat. Een op deze manier bepaalde startoplossing kan het aantal iteratiestappen met 25 % beperken. Voor sterk verzadigde problemen kan dit zelfs een vermindering van een of meerdere Newton stappen opleveren.

7.3.11 Bijkomende verfijningsregels

Het markeren van de te verfijnen zijden gebeurt in vier stappen om de kwaliteit van de vermazing te verhogen, zelfs in gebieden waar niet verfijnd moet worden.

- De zijden van een element met een aspect ratio > 5.0 worden op een speciale manier gemarkeerd om de initiële aspect ratio te verbeteren (figuur 7.24).
- Alle zijden van een te verfijnen element worden gemarkeerd.
- Alle zijden van een element dat twee randen raakt, worden gemarkeerd in de eerste adaptiestap (figuur 7.25).
- Alle zijden van elementen die raken aan een te verfijnen zijde van een element dat op de rand is gelegen, worden gemarkeerd (figuur 7.26).

figuur 0.24: *Verfijning van elementen met een aspect ratio* > 5.0

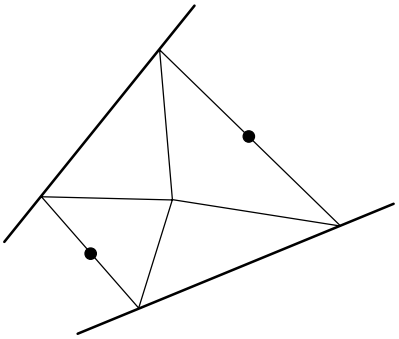

figuur 0.25: *Verfijning van een zijde van een element tussen twee randen*

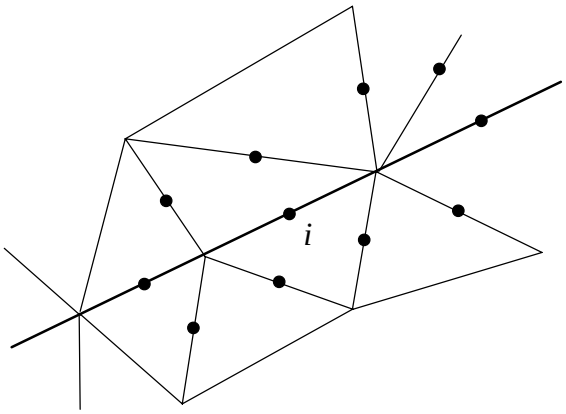

figuur 0.26: *Verfijning van zijden die raken aan een te verfijnen zijde gelegen op de rand*

CALCULATION OF GLOBAL AND LOCAL QUANTITIES, FORCE-CALCULATION

10.1 Post-processing

The fact of using arbitrary potentials (and not physical quantities) and the associated functionals in the formulation of the equations to solve, rises the need of a closer look at the post-processing stage. The user of an FEM system wants to analyse a physical system in terms of field strength, energies, forces, densities etc. The potential itself does not necessarily have a physical meaning. In some cases such as in the electrostatic and in the thermal analysis the potential represents the electric potential and the temperature respectively. But most of the quantities of interest in the post-processing will be numerically derived quantities.

The type and order of the shape function of the potential over an element (linear, quadratic, ...) and the element type (nodal, edge, etc.) determine the achievable relative accuracy of numerically derived values (chapter 4.4). The accuracy of the results will be influenced by the discretization and, related to it, the choice of the error estimator for the adaptive mesh refinement.

The aim of this chapter is to provide an overview of possible derived quantities, the necessary formulations and ways to influence the accuracy of the results. The discussion will include 2D formulations only.

10.2 Potentials

As shown in the previous chapters, the chosen potentials for the different types of problems do not necessarily represent a physical quantity directly. The formulations to define those potentials are chosen such that their application might impose simplifications in the formulation of the functionals or the choice of the gauges (chapter 3.5). A selection of problem types and the physical meaning of the potentials is given in table 1.

Type of analysis	differential equation	type of potential	physical meaning
electrostatic	$\varepsilon\nabla^2 V = -\rho$	V scalar	electric potential
magnetostatic	$\nu\nabla^2 A_z = -J_z$	A_z vector	none, $\vec{\mathbf{B}} = \text{curl}\,\vec{\mathbf{A}}$
thermal static	$\lambda\nabla^2 T = Q$	T scalar	temperature
time-harmonic magnetic	$\nu\nabla^2 A_z - j\omega\sigma A_z = -J_s$	A_z vector	induced currents related to A_z

Table 1: Physical meaning of a selected number of potentials.

The achievable accuracy of all derived values cannot be better than the accuracy of the computed potentials. The latter is determined by the choice of the element type, the shape function and the functionals used.

10.3 Energies

10.3.1 Stored energies

Energies are global quantities. In section 2.4 and in chapter 5, it has already been discussed, that in the finite element method (using the variation technique) an energy-like term (the functional) is minimized. This energy-like term does not necessarily have the meaning of a physical energy, for example a stored energy. Potentials are chosen such that the minimization of the related functional approximates the solution of the partial differential equation. In the case of a Laplace equation, the functional is:

$$F(A) = \frac{1}{2}\int_{\Omega} \nu_r |\nabla A|^2 \,\mathrm{d}\Omega \tag{0.1}$$

For a Cartesian, non-linear magnetostatic problem the stored magnetic energy can be calculated as:

$$W = \frac{\ell}{2\mu_0}\int_{\Omega}\left(\int_0^B \nu_r B \mathrm{d}B\right)\mathrm{d}\Omega \tag{0.2}$$

or for linear materials, with the material constant ν_r:

$$W = \frac{\ell}{2\mu_0}\int_{\Omega} \nu_r B^2 \mathrm{d}\Omega\,. \tag{0.3}$$

The formulas (10.1) and (10.2),(10.3) are alike. The total stored energy in the whole system (as an integration value) will be more accurate than any locally derived quantity.

Functionals for other differential equations can have additional terms in the integrant, but the similarity with an energy formulation is still maintained. The functional for the Poisson equation includes such an additional term (10.4).

$$F(A) = \frac{1}{2}\int_{\Omega}\left(\nu_r |\nabla A|^2 - 2\frac{J_S\, A}{\nu_0}\right) \mathrm{d}\,\Omega \tag{0.4}$$

The second term of the integrant could be thought to be related to the energy input from the supply. In linear systems the energy input from the supply can be calculated by the integral over the coil area:

$$W = \frac{\ell}{2}\int_{\Omega} J_s A \,\mathrm{d}\Omega \tag{0.5}$$

For linear systems, the value for the stored energy will be equal to the value of the energy input from the supply. This will only hold if all Dirichlet boundary conditions are zero (no additional flux forced into the system at the boundaries)! This last expression is even useful for non-linear problems for the calculation of flux linkages and inductances (in special cases, when the behaviour with changing current is important). The functional used for problems with linear permanent magnets is given as:

$$F(A) = \frac{1}{2}\int_{\Omega}\left(\nu_r |\nabla A|^2 - 2\frac{J_s\, A}{\nu_0} - 2A\nabla\left(\nu_{rev} M\right)\right) \mathrm{d}\,\Omega \tag{0.6}$$

The third term in the integrant could therefore be related to the energy output from the permanent magnet to the system.

Most electrostatic problems will be linear. The stored energy in an electrostatic model is then given by (Cartesian):

$$W = \frac{\ell}{2}\int_{\Omega} \varepsilon_0 \varepsilon_r E^2 \mathrm{d}\Omega \tag{0.7}$$

10.3.2 Coenergy

Associated with the energy is the concept of coenergy (Cartesian geometry, magnetic problem):

$$W_{co} = \frac{\ell}{\mu_0}\int_{\Omega} \nu_r B^2 \mathrm{d}\Omega - \frac{\ell}{2\mu_0}\int_{\Omega}\left(\int_0^B \nu_r B \mathrm{d}B\right)\mathrm{d}\Omega \tag{0.8}$$

This integral is effectively the "area under the BH-curve". The coenergy is useful for the force calculation, as it will be shown later in this chapter. In problems with linear materials and no permanent magnets, the value of the coenergy and the energy will be equal.

10.4 Local field quantities

10.4.1 Potential related physical quantities

As shown in table 1, some local field quantities are directly related to the potentials. In this case, their accuracy is determined by

- the simplifications made to the applied differential equation,
- the choice of the gauges,
- the choice of the element type,
- the choice of the shape function,
- the accuracy of the equation solver,
- and the quality of the discretization.

Therefore, the error convergence of these quantities will be of the same order as that of the related potentials.

One example:

Using the 2D magnetic vector potential, the normal component of the flux density through the edge of an element is always continuous. The flux through the edge equals the difference of the potentials in the adjacent nodes (the unit of the vector potential is Wb/m). This allows to calculate the flux through a line span between two points just by calculating the difference of the potential value at the end points. Practically, this could be applied for the calculation of flux linkages.

10.4.2 Numerically derived local field quantities

Most local field quantities, as well as other derived quantities such as force, require numerical derivatives of the potentials. Using nodal elements, the potentials are known in each node as the result of the approximate solution of the partial differential equation. The variation of the potential inside one element is determined by the choice of the shape function:

$$A_z = a + bx + cy \tag{0.9}$$

Knowing the potentials at the nodes of the elements, the coefficients *a*, *b* and *c* can be calculated using eqn. (5.4). The definition of the potential now determines the necessary mathematical operations towards the desired local field value. In case of a 2D magnetostatic problem, the vector potential $\vec{\mathbf{A}}$ is defined by:

$$\operatorname{curl} \vec{\mathbf{A}} = \vec{\mathbf{B}} \tag{0.10}$$

The *x*- and *y*-components of the flux density are calculated as follows:

$$B_x = \frac{\partial A_z}{\partial y} = \frac{1}{2\,\Delta}\sum_i^k c_i A_{zi} = \text{const inside element} \tag{0.11}$$

$$B_y = -\frac{\partial A_z}{\partial x} = -\frac{1}{2\,\Delta}\sum_i^k b_i A_{zi} = \text{const inside element} \tag{0.12}$$

Comparing the order of accuracy of *B* and of the potential, it is obvious that the accuracy of *B* is one order lower. This can be illustrated graphically on a simple test problem. Consider a trapezoidal domain containing one linear material. By applying Dirichlet boundary conditions of different values to the left and the right domain border, a constant flux is imposed in the domain (figure 10.1). The potential will be continuous (figure 10.2), the flux density however will not (figure 10.3).

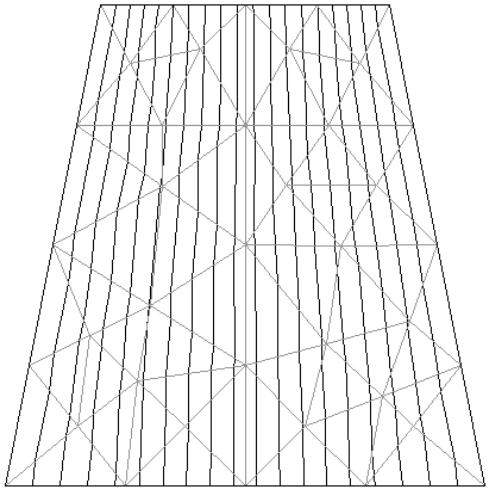

Figure 10.1 Magnetostatic problem with constant flux and trapezium shape

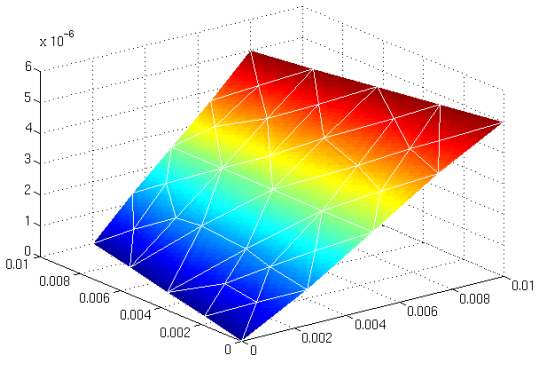

Figure 10.2 Continuous vector potential A_z

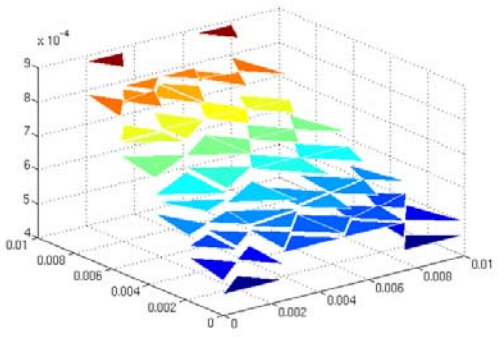

Figure 10.3 Piecewise constant flux density

The loss of one order of accuracy due to the numerical differentiation effects all quantities that are based on such derived quantities. There are three possibilities to increase the accuracy of local field quantities for the end user of an FEM-code:

- recalculate the model with higher order (shape function) elements,
- increase the quality of the discretization (adaptive mesh refinement),
- lower the error bound at which the equation solver stops.

The latter point is listed for practical reasons: Especially for eddy current and non-linear problems, a low error bound is absolutely essential. It is therefore a good choice to set a stopping margin close to the machine accuracy. If a high accuracy of the local field quantity is required, the relative error of the desired quantity should be monitored. The actions listed in the first two points of the above list can help to achieve this:

- If higher order elements are available in the code, rerun the computation by increasing the order of the elements in each step. Plot the desired quantity versus the number of steps. The relative accuracy can be judged by the convergence of the value towards an stable value.
- Monitor the convergence of the desired quantity over several steps of adaptive mesh refinement. Particular attention has to be payed to the choice of the error estimator. Some error estimators might have advantages for global quantities but would not be appropriate for local field value. The error estimator needs to have effect in the region of interest.
- The two points listed above can be combined.

Another possible way to increase the accuracy of local field quantities will be discussed in the next section: the recalculation of the field distribution in parts of the domain by a local post-process.

Two further points concerning the accuracy of local field values must be mentioned:

- Field values in the neighbourhood of singularities will have a large error. Adaptive mesh refinement can help to minimize the effect of these regions to the global solution, but the problem will not vanish.
- Smoothing techniques must be applied carefully. They are popular as they seem to establish a principle in nature: field distributions are smooth. The danger lies in the fact that almost all of the smoothing techniques are based on geometric algorithms instead on the underlying field equations. Smoothing may lead to just the opposite of what is intended by their usage: a loss of local field information.

10.5 Forces and torque's

Five different methods, their application and limits will be discussed. There are three that could be called "classics" and two rather new techniques.

10.5.1 Lorentz force

A frequently encountered situation is that of a current-carrying conductor in an external magnetic field. The differential force equation may be written:

$$\mathrm{d}\vec{\mathbf{F}} = I\left(\mathrm{d}\vec{\ell} \times \vec{\mathbf{B}}\right) \tag{0.13}$$

where $\mathrm{d}\vec{\ell}$ is the elementary length in the direction of the current I. Eqn. (10.13) is derived in theoretical electromagnetics from the fundamental force relationship between two moving charges. It represents the magnetic part of the *Lorentz force*. If the conductor is straight and the field is constant along it, the differential force may be integrated. In the case of a 2D Cartesian magnetostatic finite element calculation, there are only components of the magnetic flux density in the 2D plane, whereas the current is directed perpendicular to it. In this case eqn. (10.13) can be simplified to the following expression for the conductor of length ℓ:

$$F = BI\ell \tag{0.14}$$

Theoretically eqns. (10.13) and (10.14) are only valid for an isolated conductor in an infinite field. However, in practice it might be used even for the force calculation in machines with many slots containing current, provided that B is the average value in the air gap. This simplification already indicates a loss of accuracy, as local information about the field is not taken into account. This approach combines analytical machine analysis and numerical field analysis at a rather simplified level.

10.5.2 Virtual work

One of the most popular methods for the calculation of forces is based on the spatial rate of change of the stored coenergy in the model. The component of the force F_s in the direction of the displacement s is given by:

$$F_s = \frac{\partial W_{co}}{\partial s} \approx \frac{\mathrm{d}W_{co}}{\mathrm{d}s} \tag{0.15}$$

As shown in section 10.3.2, the accuracy of the coenergy calculation is rather high. It can be expected that the force calculation based on the coenergy should be accurate as well, provided the following restrictions are met:

- The method is valid for differential small displacements, which must be translated in terms of the dimensions of the model.
- The method is valid only if the current in the different models is kept constant.

The disadvantage of this method is the need of at least two finite element computations.

A corresponding expression for the torque T associated with an angular rotation θ is useful for the machine analysis:

$$T = \frac{\partial W_{co}}{\partial \theta} \approx \frac{\mathrm{d}W_{co}}{\mathrm{d}\theta} \tag{0.16}$$

In the rare case of keeping the flux constant, an expression including the stored energy can be used:

$$F_s = -\frac{\partial W}{\partial s} \approx -\frac{\mathrm{d}W}{\mathrm{d}s} \tag{0.17}$$

10.5.3 Maxwell stress tensor method

The probably most common approach to determining electromechanical forces is known as the Maxwell stress tensor method. In contrast to the virtual work method, which is based on the energy in the system, the Maxwell stress tensor method describes the forces directly in terms of the magnetic field strength. This method is attractive as forces can be determined with only one FEM-solution.

The Maxwell stress approach computes the local stress at all points of a bounding surface and then sums the local stresses (using a surface integral) to find the overall force. The expression for the Maxwell stress tensor can be derived from eqn. (10.13) as shown in the literature. In three dimensions the force then becomes a surface integral:

$$\vec{\mathbf{F}} = \nu \oint_S \vec{\mathbf{T}} \mathbf{d}\vec{\mathbf{S}} \tag{0.18}$$

where the surface vector $\mathbf{d}\vec{\mathbf{S}}$ is taken as the outward normal on S. For two dimensions, this reduces to a line integral with the magnetic stress tensor $\vec{\mathbf{T}}$ written as:

$$\vec{\mathbf{T}} = \begin{bmatrix} \left(B_x^2 - \frac{1}{2}|B|^2\right) & B_x B_y \\ B_y B_x & \left(B_y^2 - \frac{1}{2}|B|^2\right) \end{bmatrix}. \tag{0.19}$$

The expression given above may be rewritten in terms of the normal and tangential components of flux density at each point on the closed contour *C* along which the line integral has to be evaluated. The associated components of force for an axial length ℓ can therefore be found as follows:

$$F_x = \frac{\ell}{2\mu_0} \oint_C \left(B_x B_n - B_y B_t\right) \mathrm{d}l \tag{0.20}$$

$$F_y = \frac{\ell}{2\mu_0} \oint_C \left(B_y B_n + B_x B_t\right) \mathrm{d}l \tag{0.21}$$

These expressions assume the following convention for the directions of B_n and B_t: for a contour parallel to the *y*-axis, and traversed in the direction of increasing *y*, $B_n = B_x$ and $B_t = B_y$. Also the component values of eqn. (10.19) have units of stress, they do not necessarily give correct local stress values. However there closed line integral has the physical meaning of the total force on the enclosed object. The contour must be entirely in air and not pass through any

other material. In many cases the contour does not need to be closed. Parts of the closed contour might be skipped if their integral value is negligible. The expressions for the force computed on a single straight line are:

$$F_n = \frac{\ell}{2\mu_0}\int \left(B_n^2 - B_t^2\right) \mathrm{d}l \tag{0.22}$$

$$F_t = \frac{\ell}{\mu_0}\int B_n B_t \, \mathrm{d}l \tag{0.23}$$

The torque on an arc of radius r is similarly given by:

$$T = \frac{1}{\mu_0}\int B_n B_t r \, \mathrm{d}l \tag{0.24}$$

Similar expressions may be used for electric field problems by substituting E for B and e_0 for $1/\mu_0$.

The advantage of the Maxwell stress tensor method over the virtual work method of needing only one FEM-solution is lost when the accuracy of the results is compared. As the method is based on derived values, care has to be taken in its application. The loss of one order of accuracy compared to the potential solution can lead to large errors, especially when using eqns. (10.23) and (10.24). The practical implementation of the algorithm is introducing additional error sources. The stress values have to be evaluated at specified points along the contour, usually equidistantly distributed. If such a point is positioned exactly on the edge between two elements, the numerically derived B is double valued (piecewise constant B for first order shape function). The choice, from which elements the values are taken, depends on the search algorithm that is implemented and on round-off errors in the calculation of the co-ordinates.

Another problem arises when the value of the normal and tangential components of the local flux density differs by magnitudes. The integration may involve the subtraction of large numbers to yield small results.

The problem of accuracy of the Maxwell stress tensor method and possible ways of improving it have been extensively discussed in literature. Most of the proposed enhancements are based on smoothing algorithms or on different integration schemes. One of the most common methods is proposing to calculate the force on several different contours and averaging the result. This method can help to evaluate the margin of error in the calculation, but it will not give any absolute error bounds or even an enhancement of the accuracy, as the underlying principle is a pure geometrical one.

OPTIMALISERING

Het belang van optimalisatie van elektromagnetische apparaten neemt toe. ‘Automated Optimal Design’ (AOD) is een zelfgestuurd numerisch optimalisatie proces. Recente ontwikkelingen in numerische algoritmen en steeds krachtiger computers laten toe om praktische problemen te behandelen. Dit type van problemen onderscheidt zich door een hoge complexiteit tengevolge van de onderlinge afhankelijkheid van een groot aantal ontwerpparameters en randvoorwaarden. Meestal is de relatie tussen de gewenste kwaliteit van het produkt en de ontwerpparameters niet gekend. Stochastische optimalisatiemethoden in combinatie met numerische veldberekeningen zoals de eindige elementen methode, bieden de meest algemene aanpak van AOD aan. Een kostenminimalisatie van een kleine gelijkstroommotor door optimalisatie van de vorm van stator en anker illustreert de technische bruikbaarheid voor niet-lineaire magnetostatische problemen.

11.1 Inleiding

De toename van de vermogendichtheid in elektromagnetische apparaten, door een verhoging van de magnetische inductie, wordt beperkt door het niet-lineair gedrag van de ijzeren delen. Een supplementaire verhoging kan bekomen worden door de optimalisatie van het niet-lineair magnetisch netwerk. De combinatie van ‘evolution strategy’ en ‘simulated annealing’ geeft een robuust optimalisatie proces. De evalutie van de kwaliteit gebeurt met de eerste orde eindige elementen methode.

Het ontwerpproces van elektromagnetische apparaten komt neer op een optimalisatie. De constructie en de stap per stap optimalisatie van technische systemen is een ‘trial and error’-proces. De ontwerpprocedure kan tot een gedeeltelijke optimale oplossing leiden omdat succes en inspanning sterk afhangen van de ervaring van de ontwerper. Om de ontwerpcyclus te versnellen, wordt het fysisch gedrag van de systemen met numerische methoden gesimuleerd. Voor een geautomatiseerde optimale ontwerpmethode is bovendien een numerische optimalisatie vereist. De combinatie van twee ‘random’ gebaseerde zoekalgoritmen, ‘evolution strategy’ en ‘simulates annealing’ wordt besproken.

11.2 Numerische methoden

De verschillende numerische methoden worden geëvalueerd op basis van hun

- betrouwbaarheid
- robuustheid
- ongevoeligheid voor stochastische variaties
- toepassingsgebied

- nauwkeurigheid
- stabiliteit
- performantie.

Stochastische optimalisatie methoden voldoen aan deze eisen. Hun grootste voordeel is hun ongevoeligheid voor stochastische variaties op de kwaliteitsfunctie, veroorzaakt door de numerische berekeningsmethode [3]. Deze ongevoeligheid volgt uit het niet-deterministisch karakter van het zoekalgoritme en het niet-gebruiken van afgeleide functies. Een tweede belangrijke eigenschap is de eenvoudige behandeling van randvoorwaarden. Een ingewikkelde transformatie naar een formulering zonder randvoorwaarden is niet nodig.

Om het niet-lineair veldprobleem op te lossen is voor een algemeen toepasbare methode gekozen. De veldberekening kan o.a. op basis van magnetische netwerken [1] of met de eindige differentiemethode gebeuren. Er is hier voor de eindige elementen methode gekozen met verfijning van de vermazing op basis van de geschatte fout. Deze methode in niet onderhevig aan al te veel geometrische beperkingen.

11.3 Stochastische optimalisatie

Optimalisatie vereist dat alle ontwerpdoelstellingen samen gebracht worden in een enkele functie, de kwaliteitsfunctie $Z(\mathrm{x})$. Deze functie hangt af van alle ontwerpparameters en geeft de kwaliteit van het ontwerp weer. Deze kwaliteitsfunctie is het gewogen gemiddelde van de verschillende doelstellingen $\mathrm{Z}_1, \mathrm{Z}_2, ..., \mathrm{Z}_\mathrm{n}$.

$$Z = \sum_{i=1}^{n} a_i \; Z_i \tag{0.1}$$

met

a_i gewichtsfactoren

De randvoorwaarden $G_j(x)$ beperken de toegelaten parametervariatie. Met de voorwaarden $g_i \le g_{i,\max}$ en $g_i \ge g_{i,\min}$, wordt een bruikbare formulering voor een lineaire combinatie bekomen:

$$Z = \sum_i a_i \; 10^{\left(\frac{g_i - g_{i,\max}}{g_{i,\max}}\right)} + \sum_j a_j \; 10^{\left(\frac{g_{j,\min} - g_j}{g_j}\right)} \quad \rightarrow \quad \min. \tag{0.2}$$

Dit is een zwakke formulering voor de behandeling van randvoorwaarden. Wanneer niet aan de randvoorwaarden voldaan is, wordt dit in rekening gebracht door een penalisatieterm overeenkomstig (11.2) in te voeren. Een strengere formulatie houdt een verwerping van de parameter in en een nieuwe waarde wordt toegewezen tot de randvoorwaarden voldaan zijn.

In wiskundige termen heeft een optimalisatie een niet-lineair karakter met inbegrip van randvoorwaarden en komt neer op minimalisatie van

$$Z(\mathrm{x}) = Z(x_1, x_2, \ldots, x_n) \;\rightarrow\; \min. \tag{0.3}$$

met de onafhankelijke variabelen $\mathrm{x} = \{x_i \;:\; i = 1(1)n\}$ in de ruimte $\mathrm{x} \in IR^n$ en met de randvoorwaarden $j = 1(1)m$

$$G_j(\mathrm{x}) = G_j(x_1, x_2, \ldots, x_n) \begin{Bmatrix} \leq \\ = \end{Bmatrix} 0 \tag{0.4}$$

Door het gebruik van numerische technieken om $Z(\mathrm{x})$ te benaderen, bestaat er geen expliciet verband tussen de kwaliteitsfunctie en de ontwerpparameters. De berekening van afgeleiden is hierdoor moeilijk en onderhevig aan afrondings- en discretisatiefouten. Bovendien worden extra fouten geïntroduceerd door de berekening van de kwaliteitsfunctie. Hierdoor is de meest eenvoudige en meest betrouwbare methode het gebruik van een stochastisch zoekalgoritme voor optimalisatie.

Op basis van de regels van 'evolution strategy' worden willekeurige variaties op de verschillende parameters x_i uitgevoerd. Met het invoeren van een controle parameter, de temperatuur *T*, in het zoekalgoritme wordt vermeden dat het proces vastloopt in een lokaal extremum. 'Evolution strategy' gebruikt het idee van natuurlijke mutatie en selectie (survival of the fittest). Het basisidee wordt teruggevonden in DARWIN's nota's over de kwaliteit van systemen. De drijvende kracht van het optimalisatieproces is het doorvoeren van mutatie en selectie in elke stap. Verschillende strategieën kunnen onderscheiden worden met: μ het aantal ouders, λ het aantal kinderen en ρ de erfelijksheidsfactor.

- $(\mu + \lambda)$-plus-strategie: de populatie van de volgende generatie wordt geselecteerd uit de μ ouders en de λ kinderen.
- (μ, λ)-komma-strategie: de populatie van de volgende generatie wordt geselecteerd uit de μ beste kinderen. De ouders overleven slechts een generatie.
- $\left(\frac{\mu}{\rho} + \lambda\right)$-strategie: ρ ouders dragen bij tot de generatie van een kind. $1/\rho$ van de eigenschappen van een ouder wordt overgedragen aan het kind.
- $\left(\frac{\mu}{\rho}, \lambda\right)$-strategie: komma variant van de $\left(\frac{\mu}{\rho} + \lambda\right)$-strategie.

De verschillende strategieën verschillen enkel op basis van het selectiemechanisme. Om de eenvoud en de algemene toepasbaarheid aan te tonen, geeft figuur 1 een mogelijk selectiemechanisme weer.

De mutatie van de verschillende parameters van de initiële generatie (ouders) geeft aanleiding tot kinderen. De eigenschappen per kind kunnen afhangen van meerdere ouders. Afhankelijk van de gebruikte strategie, worden de beste kinderen gekozen als volgende generatie.

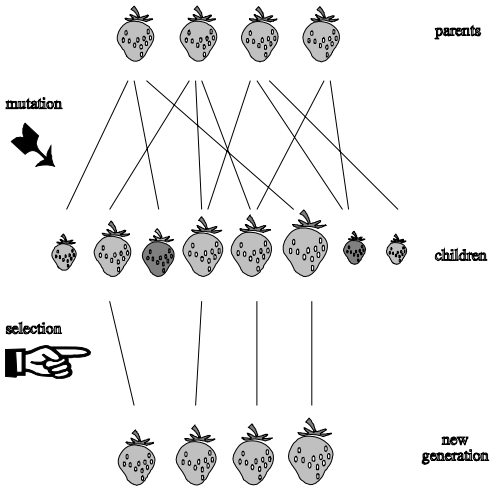

Fig. 1 *Eenvoudige methode van mutatie en selectie*

In een optimalisatieproces leidt de herhaling van mutatie en selectie van de verschillende parameters van een tijdelijke naar een verbeterde oplossing. Om deze procedure om te vormen naar een efficiënte methode, is controle van de staplengte noodzakelijk. Bij een kleine staplengte vertoont de methode een slechte convergentie. Een verbetetering van de kwaliteit wordt niet vastgesteld. Aan de ander kant zal een te grote staplengte aanleiding geven tot 'random' fluctuaties. De convergentiesnelheid van 'evolution strategy' is maximaal voor een beperkte reeks waarden van de staplengte. Een gemiddeld afnemende staplengte verzekert convergentie tijdens de optimalisatie [2],[6]. Op deze manier dient de staplengte ook als convergentie- en stopcriterium.

Mutatie gebeurt op basis van 'random' variaties van de verschillende parameters. Voor elke iteratiestap (k) wordt de nieuwe waarde $x_{C,i}^{(k)}$ bepaald uit de ouder parameter $x_{P,i}^{(k)}$.

$$x_{C,i}^{(k)} = x_{P,i}^{(k)} + \delta_{C,i}^{(k)}\ p_i^{(k)} \text{ met } i = 1(1)n \tag{0.5}$$

Om de staplengte $\delta_{C,i}^{(k)}$ van de ouder generatie door te geven naar de nieuwe generatie, wordt de staplengte van een willekeurige ouder gebruikt als gemiddelde waarde voor de nieuwe waarden van de staplengten.

$$\delta_{C,i}^{(k)} = \frac{1}{\rho}\sum_{j=1}^{\rho}\delta_{P,j}^{(k)}\ (z_j^{(k)}(\mu)) \text{ met } \begin{cases} i = 1(1)n \\ j = 1(1)\rho \end{cases} \tag{0.6}$$

$z_j^{(k)}(\mu)$ is een uniform verdeelde 'random' gehele waarde uit het interval $[1,\mu]$. De gemiddelde waarde van de staplengte wordt aangepast met een factor α.

$$\delta_{C,i}^{(k)} = \begin{cases} \delta_{C,i}^{(k)} \cdot \alpha & : i = 1(1)\lambda/2 \\ \delta_{C,i}^{(k)} \cdot 1/\alpha & : i = \lambda/2 + 1(1)\lambda \end{cases} \tag{0.7}$$

De uiteindelijke staplengte wordt bepaald door een MAXWELL waarschijnlijkheidsverdeling $\varphi(c)$ met meest waarschijnlijke waarde c_W.

$$\varphi(c) = \frac{4}{c_W\sqrt{\pi}}\left(\frac{c}{c_W}\right)^2 \exp(-\left(\frac{c}{c_W}\right)^2) \tag{0.8}$$

Om de zoekrichting te bepalen in een *n*-dimensionale ruimte wordt een 'random' vector $\mathrm{p}_i^{(k)}$ bepaald met

$$\left|\mathrm{p}_i^{(k)}\right| = \sqrt{(p_1^{(k)})^2 + \cdots + (p_n^{(k)})^2} = 1 \tag{0.9}$$

Om een globale optimalistiemethode te bekomen, wordt 'simulated annealing' [5] gecombineerd met 'evolution strategy'. Het invoeren van een energieterm voor de kwaliteit van een syteem geeft een robuuste optimalisatiemethode [2].

Met de fundamenten van de statische fysica kan aangetoond worden dat bij thermisch evenwicht de waarschijnlijkheid van de energie bepaald wordt door een BOLTZMANN verdeling. De energie E_i van een systeem in de macroscopische toestand *i* wordt gegeven door

$$prob\{E_i\} = \frac{1}{P(T)}\exp\left(-\frac{E_i}{k_B T}\right) \tag{0.10}$$

Met $P(T)$ gedefinieerd als

$$P(T) = \sum_i \exp\left(-\frac{E_i}{k_B T}\right) \tag{0.11}$$

Waarbij de sommatie loopt over alle mogelijke macroscopische toestanden.

Op basis van statistische fysica kan het aanvaardingscriterium geformuleerd worden als:

$$\xi < prob\{\Delta E_i\} = \exp(-\frac{\Delta E_i}{k_B T}) \tag{0.12}$$

Indien $\Delta E_i \le 0$, dan wordt het kind aanvaard. Indien $\Delta E_i > 0$, dan wordt het kind statistisch behandeld volgens het METROPOLIS criterium [5],[7]. ξ is een uniform verdeelde 'random' waarde uit het interval $[0,1]$.

Om het hele optimalisatieproces te vormen, is tenslotte een temperatuursverloop nodig. De temperatuur wordt verlaagd op een manier dat op het einde van de optimalisatie er geen kans is op een gualisteitswijziging. Een eenvoudig maar doeltreffend verloop wordt gegeven door

$$T^{(k)} = \alpha^{(k)} \cdot T^{(0)} \text{ met } 0 < \alpha < 1 \tag{0.13}$$

Dit algoritme is voorgesteld in figuur 2. Het vereiste thermisch evenwicht wordt bekomen indien er geen verhoging van de kwaliteit wordt vastgesteld of indien het maximaal aantal iteraties wordt overschreden. De optimalisatie wordt beëindigd als er geen kwaliteitswijziging meer is.

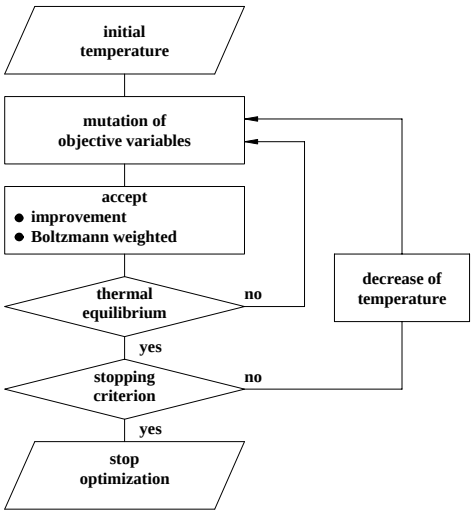

Fig. 2 *Blokschema van een gecombineerd zoekalgoritme*

11.4 Berekening van het magnetisch veld

De tweedimensionale eindige elementen methode wordt gebruikt om het veld te bepalen. De magnetische vectorpotentiaal wordt benaderd als een eerste graadsfunctie over de driehoekige elementen. Om een bepaalde nauwkeurigheid te verzekeren wordt het model adaptief verfijnd. Om de vermazing en de numerische fouten te controleren wordt de lokale foutverdeling berekend en de vermazing wordt verfijnd op die plaatsen waar de fout groter is dan een bepaalde grenswaarde. De fout *e* wordt berekend op basis van de niet-continuïteit van de tangentialel componente van de magnetische veldsterkte op naast elkaar liggende elementzijdes.

$$e = H_{t1} - H_{t2} = \frac{1}{\mu_1}\frac{\partial A_1}{\partial n} - \frac{1}{\mu_2}\frac{\partial A_2}{\partial n} \tag{0.14}$$

Figuur 3 toont de initiële vermazing en de vermazing na adaptie van een kleine permanent magneet gelijkstroommachine. Figuur 4 toont een beeld van het veld.

11.5 Optimalisatie van een elektrische machine

Als toepassing van de besproken methode wordt een kleine permanent magneet gelijkstroom-machine geoptimaliseerd. De bedoeling is de kostprijs bepaald door het volume van het permanent magneetmateriaal, koper en ijzer, te minimaliseren voor een gegeven koppel. De kwaliteitsfunctie wordt gegeven door

$$Z(\mathrm{x}) = 10^{\left(\frac{kost(x)-kost_{\max}}{kost_{\max}}\right)} + penalisatie \tag{0.15}$$

met

$$penalisatie = \begin{cases} T < T_{\min} : 10^{\left(\frac{T_{\min}-T(x)}{T(x)}\right)} \\ T \geq T_{\min} : 1 \end{cases} \tag{0.16}$$

Deze vorm laat een evaluatie toe zelfs indien de randvoorwaarde van het koppel overschreden wordt.

Het koppel wordt berekend door integratie van de Maxwell spanningstensor in de luchtspleet. De ijzerverliezen die afhankelijk zijn van de magnetische inductie, worden ingerekend door het luchtspleetkoppel bij 200 min^{-1} te verminderen om $T(x)$ te bekomen. De geometrie wordt bepaald door 15 parameters. De parameters zijn de $n/2$ zijden van de polygoon die de ankergleuf beschrijven en de buitenafmetingen van stator en anker zoals aangegeven of figuur 5.

De randvoorwaarden volgen uit de constructie voorwaarden. De vormverandering gedurende de optimalisatie wordt getoond in figuur 6. De initiële ijzer delen zijn overgedimensioneerd. Het koppel van de initiële motor is 25 % lager dan de gewenste waarde T_{min}. De geoptimaliseerde motor voldoet aan de koppelvereiste, voornamelijk bekomen door de toename van koper met 20 %. De grootste verandering is de halvering van het ijzervolume.

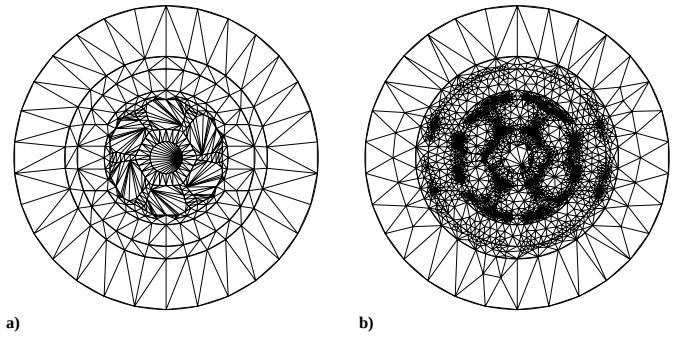

Fig. 3 a) *Initiële vermazing en* b) *vermazing na adaptie*

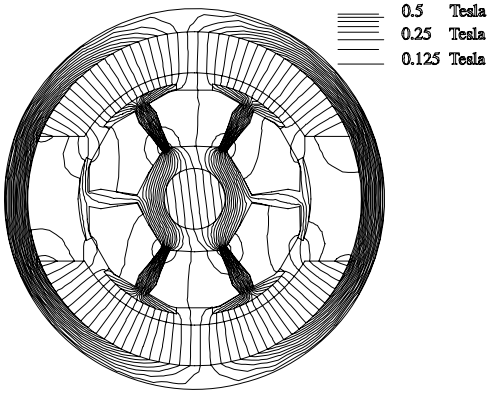

Fig. 4 *Veldlijnenbeeld*

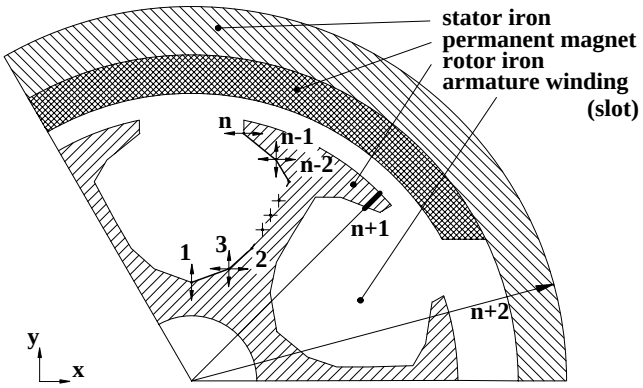

Fig. 5 *Geometrie van de motor*

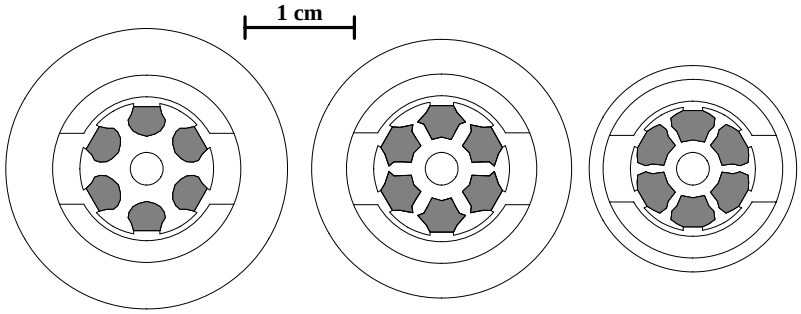

Fig. 6 *Initiele, tussentijdse en geoptimaliseerde geometrie*

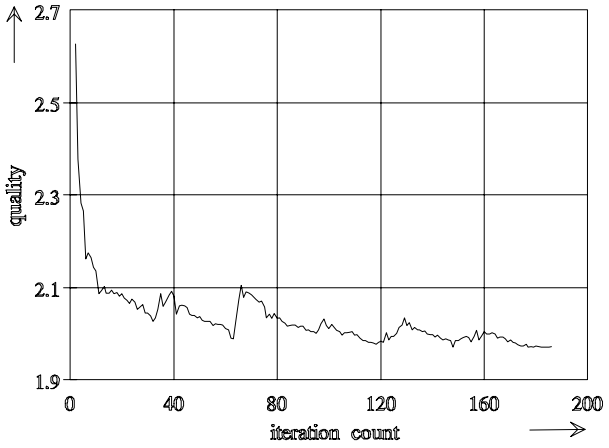

Fig. 7 *Kwaliteitswaarde voor de verschillende iteratiestappen*

In vergelijking hiermee levert verwaarlozing van de ijzerverliezen een 10 % kleinere diameter van het anker op. Door de broosheid van de permanente magneten, hebben de segmenten een minimale hoogte. Het volume permanent magneetmateriaal is lichtjes afgenomen. Het totaal volume is afgenomen met 38 %. Figuur 7 toont de convergentiesnelheid.

11.6 Besluiten

De methode voor een globale minimalisatie van continue functies is een combinatie van ‘evolution strategy’ en ‘simulated annealing’. Om de efficiëntie van het algoritme te verhogen wordt de Maxwell waarschijnlijkheidsverdeling gebruikt om de finale staplengte te bepalen. De niet-lineaire berekening van een kleine permanent magneet gelijkstroommotor toont het

gebruik van het optimalisatieproces. De kwaliteitsfunctie is berekend uitgaande van de eindige elementen oplossing. De gebruikte methode vereist vele functie evaluaties om het globaal optimum te vinden. Daarom hangt de rekentijd in sterke mate af van de complexiteit van het probleem.

De generatie van de verschillende modellen is onafhankelijk van elkaar. Dit laat toe om het algoritme te gebruiken op parallellle computers. Figuur 8 toont dit proces dat de rekentijd sterk vermindert. Het optimalisatieproces start van een initieel stel parameters en randvoorwaarden. 'Pre-processing', wat neer komt op de berekening van de geometrie uit de parameters, definitie van de gebieden met verschillende materiaaleigenschappen en het opstellen van de vermazing, kan parallel uitgevoerd worden. Controle van de randvoorwaarden vindt plaats in zowel 'pre-' als 'post-processing'. Na de veldberekening moet het proces gesynchronizeerd worden om de data te verwerken in het optimalisatiealgoritme. Het stopcriterium wordt geëvalueerd, en mutatie en selectie worden doorgevoerd. Na uitvoering van het optimalisatiealgoritme wordt een nieuwe reeks modellen in parallel berekend.

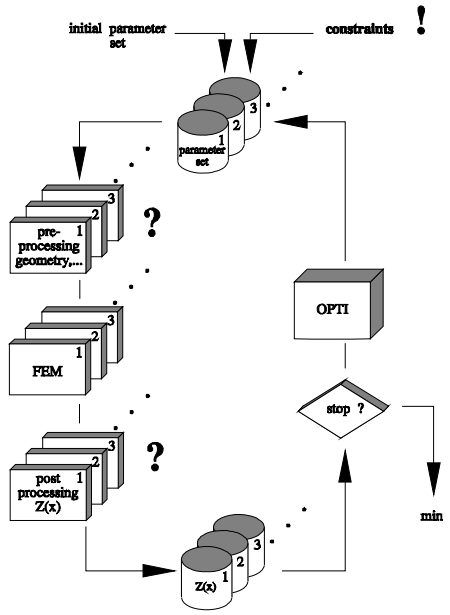

Fig. 8 *Controle van het optimalisatieproces*

Referenties

[1] Hameyer, K. and Hanitsch, R., 1993, Proc. Conf. COMPUMAG 93, Miami, USA, 90-91.

[2] Hameyer, K., 1992, "Beitrag zum automatischen optimalen Entwurf von elektromechanischen Wandlern am Bei-spiel eines Stellantriebs", *Reihe Elektrotechnik*, Verlag Shaker, Aachen, Germany.

[3] Kasper, M., 1990, "Die Optimierung elektro-magnetischer Felder mit Hilfe der Finiten Elemente Methode und deren Anwendung auf ein Wirbel-stromproblem", *Reihe Elektrotechnik*, Nr. 70, VDI Verlag, Düsseldorf, Germany.

[4] Patarnello, S. and Carnevali, P., 1989, "Learning capabilities of boolean networks", ed. in *Neural computing architectures, The design of brain-like machines*, North Oxford Academic Publishers Ltd., UK.

[5] Kirkpatrick, S., Gelatt, C.D. and Vecchi, M.P., 1988, Science 220:671-680, ed. in Neurocomputing, Foundations of Research, 554-567.

[6] Schwefel, H.-P., 1981, "Numerical optimization of computer models", Wiley & Sons, Chichester.

[7] Metropolis, N., Rosenbluth, A., Rosenbluth, M., Teller, A. and Teller, E., 1953, Journal of Chem. Physics, 21, 1087-1092.